



AMERICAN METEOROLOGICAL SOCIETY

Journal of Climate

EARLY ONLINE RELEASE

This is a preliminary PDF of the author-produced manuscript that has been peer-reviewed and accepted for publication. Since it is being posted so soon after acceptance, it has not yet been copyedited, formatted, or processed by AMS Publications. This preliminary version of the manuscript may be downloaded, distributed, and cited, but please be aware that there will be visual differences and possibly some content differences between this version and the final published version.

The DOI for this manuscript is doi: 10.1175/JCLI-D-12-00417.1

The final published version of this manuscript will replace the preliminary version at the above DOI once it is available.

If you would like to cite this EOR in a separate work, please use the following full citation:

Anav, A., P. Friedlingstein, M. Kidston, L. Bopp, P. Ciais, P. Cox, C. Jones, M. Jung, R. Myneni, and Z. Zhu, 2013: EVALUATING THE LAND AND OCEAN COMPONENTS OF THE GLOBAL CARBON CYCLE IN THE CMIP5 EARTH SYSTEM MODELS. *J. Climate*. doi:10.1175/JCLI-D-12-00417.1, in press.



1 **EVALUATING THE LAND AND OCEAN COMPONENTS OF THE GLOBAL**
2 **CARBON CYCLE IN THE CMIP5 EARTH SYSTEM MODELS**

3
4
5
6
7
8
9
10
11
12
13
14
15
16
17
18
19
20
21
22
23
24

A. Anav ^{1*}, P. Friedlingstein ¹, M. Kidston ², L. Bopp ², P. Ciais ², P. Cox ¹, C. Jones ³, M. Jung ⁴,
R. Myneni ⁵, Z. Zhu ⁵

¹*University of Exeter, College of Engineering, Mathematics and Physical Sciences, Exeter, England*

²*Laboratoire des Sciences du Climat et de l'Environnement, LSCE, Gif sur Yvette, France*

³*Met Office Hadley Centre, Exeter, UK*

⁴*Max Planck Institute for Biogeochemistry, MPI, Jena, Germany*

⁵*Boston University, Department of Geography & Environment, Boston, USA*

***Corresponding author:** Alessandro Anav, A.Anav@exeter.ac.uk, College of Engineering,
Mathematics & Physical Sciences, Harrison Building, North Park Road, Exeter EX4 4QF, UK

27 **ABSTRACT**

28 We assess the ability of 18 Earth System Models to simulate the land and ocean carbon cycle for the
29 present climate. These models will be used in the next Intergovernmental Panel on Climate Change
30 (IPCC) Fifth Assessment Report (AR5) for climate projections, and such evaluation allows
31 identification of the strengths and weaknesses of individual coupled carbon-climate models as well as
32 identification of systematic biases of the models.

33 Results show that models correctly reproduce the main climatic variables controlling the spatial and
34 temporal characteristics of the carbon cycle. The seasonal evolution of the variables under
35 examination is well captured. However, weaknesses appear when reproducing specific fields: in
36 particular, considering the land carbon cycle, a general overestimation of photosynthesis and leaf area
37 index is found for most of the models, while the ocean evaluation shows that quite a few models
38 underestimate the primary production.

39 We also propose climate and carbon cycle performance metrics in order to assess whether there is a set
40 of consistently better models for reproducing the carbon cycle. Averaged seasonal cycles and
41 probability density functions (PDFs) calculated from model simulations are compared with the
42 corresponding seasonal cycles and PDFs from different observed datasets.

43 Although the metrics used in this study allow identification of some models as better or worse than the
44 average, our ranking is partially subjective due to the choice of the variables under examination, and
45 can be also sensitive to the choice of reference data. In addition, we found that the model
46 performances show significant regional variations.

47
48
49
50
51
52
53

54 1. INTRODUCTION

55 Earth System Models (ESMs) are complex numerical tools designed to simulate physical, chemical
56 and biological processes taking place on Earth between the atmosphere, the land and the ocean.
57 Worldwide, only a few research institutions have developed such models and used them to carry out
58 historical and future simulations in order to project future climate change.

59 ESMs, and numerical models in general, are never perfect. Consequently, before using their results to
60 make future projection of climate change, an assessment of their accuracy reproducing several
61 variables for the present climate is required. In fact, the ability of a climate model to reproduce the
62 present-day mean climate and its variation adds confidence to projections of future climate change
63 (Reifen and Toumi 2009). Nevertheless, good skills reproducing the present climate do not necessarily
64 guarantee that the selected model is going to generate a reliable prediction of future climate (Reichler
65 and Kim 2008).

66 ESMs are routinely subjected to a variety of tests to assess their capabilities, and several papers
67 provide extensive model evaluation (e.g. Tebaldi et al. 2006; Lin et al. 2007; Lucarini et al. 2007;
68 Santer et al. 2007; Gillett et al. 2008; Gleckler et al. 2008; Reichler and Kim 2008; Schneider et al.
69 2008; Santer et al. 2009; Tjiputra et al 2009; Knutti et al. 2010; Steinacher et al. 2010; Radić and
70 Clarke 2011; Scherrer 2011; Chou et al. 2012; Séférian et al. 2012; Yin et al. 2012). In these papers,
71 the authors describe the performance of climate models by measuring their ability to simulate today's
72 climate at various scales from global to regional. Results reported in these papers indicate that not all
73 models simulate the present climate with similar accuracy. Furthermore, it should be noted that these
74 papers also highlighted that the best models for a particular region of the Earth do not always achieve
75 the same degree of performance in other regions. Additionally, the skill of the models is different
76 according to the meteorological variables examined.

77 Within this context, the aim of this paper is twofold. The first aim is to quantify how well the CMIP5
78 (Coupled Model Intercomparison Project phase-5, Taylor et al. 2011) models represent the 20th
79 century carbon cycle over the land and ocean, as well as the main climatic variables that influence the
80 carbon cycle.

81 Traditional model evaluation, or diagnostics (e.g. Collins et al. 2006; Delworth et al. 2006; Johns et al.
82 2006; Zhou and Yu 2006; Waliser et al. 2007; Lin et al. 2008; Volodin et al. 2009; Marti et al. 2010;
83 Xavier et al. 2010; Arora et al. 2011; Chylek et al. 2011; Collins et al. 2011; Radić and Clarke 2011;
84 Watanabe et al. 2011), provide detailed assessments of the strengths and weaknesses of individual
85 climate models based principally on seasonal and annual timescales, as well as on anomaly maps and
86 zonal means.

87 Our model evaluation is performed at three different time scales: first, we analyze the long-term trend,
88 which provides information on the model capability to simulate the temporal evolution over the 20th
89 century, given GHG and aerosol radiative forcing. Second, we analyze the interannual variability
90 (IAV) of physical variables as a constraint on the model capability to simulate realistic climate
91 patterns that influence both ocean and continental carbon fluxes (Rayner et al 2008). Third, we
92 evaluate the modelled seasonal cycle which, particularly in the Northern Hemisphere, constrains the
93 model's simulation of the continental fluxes.

94 The second aim of the paper is to assess whether there is a set of consistently better models
95 reproducing the carbon cycle and the main physical variables controlling the carbon cycle. One of the
96 scientific motivations is that modellers commonly make use of large climate model projections to
97 underpin impact assessments. So far, IPCC assumed that all climate models are equally good and they
98 are equally weighted in future climate projections (Meehl et al. 2007). If an impacts modeller wants to
99 choose the best models for a particular region however, assuming all models are equally good is not a
100 requirement and models could be ranked, weighted or omitted based on performance.

101 Contrasting with diagnostics, metrics could be developed and used for such purposes (Gleckler et al.
102 2008; Maximo et al. 2008; Cadule et al. 2010; Räisänen et al. 2010; Chen et al. 2011; Errasti et al.
103 2011; Moise et al. 2011; Radić and Clarke 2011).

104
105
106
107

108 2. MODELS, REFERENCE DATA SETS, AND ASSESMENT OF PERFORMANCES

109 2.1 CMIP5 simulations

110 In this study we analyze outputs from 18 coupled carbon-climate models that are based on the set of
111 new global model simulations planned in support of the IPCC Fifth Assessment Report (AR5). These
112 simulations are referred to as CMIP5 (Coupled Model Intercomparison Project phase-5). This set of
113 simulations comprises a large number of model experiments, including historical simulations, new
114 scenarios for the 21st century, decadal prediction experiments, experiments including the carbon cycle
115 and experiments aimed at investigating individual feedback mechanisms (Taylor et al. 2011). The
116 CMIP5 multi-model data set has been archived by PCMDI and has been made available to the climate
117 research community (<http://cmip-pcmdi.llnl.gov/cmip5/>).

118 Here we summarize the physical and biogeochemical model's performances for the historical
119 experiment only (i.e. ESMs driven by CO₂ concentration). Among all the available CMIP5 ESMs, we
120 selected the only models simulating both the land and ocean carbon fluxes and reporting enough
121 variables for our analysis.

122 The models used in this study, as well as their atmospheric and ocean grids, are listed in **Table 1**; note
123 that all the diagnostics and statistics are computed after regridding each model's output, and reference
124 datasets, to a common 2x2 degrees grid. In case of carbon fluxes, our regridding approach assumed
125 conservation of mass, while for the physical fields as well as for the LAI, we used a bilinear
126 interpolation.

127 **Table 2** reports the land and ocean biogeochemical models used by ESMs, while **Table 3** lists the
128 variables considered in this study with the number of independent realizations (or ensemble member)
129 for each model/variable. In fact, some models have only one run (realization), but other models have
130 up to five runs (**Table 3**). These realizations are climate simulations with different initial conditions.
131 In the next section, we present results only from the first realization for each individual climate model,
132 while for the final ranking we use the realization with the highest score for each individual model. In
133 general it is expected that the ensemble of runs associated with a particular model with the same
134 external forcing will reproduce very similar seasonal cycle and range of climate variability,

135 irrespective of the initial conditions (Errasti et al. 2011). However because of each ensemble member
136 having its own internal variability (largely unforced), the interannual variability of the ensemble
137 average is expected to be reduced with respect to one individual simulation; for such reason we
138 decided to use results from only the first realization, rather than the ensemble mean over the available
139 realizations.

140 Our analysis focuses on the historical period (20th century simulations; historical experiment, CO₂
141 concentration driven), which was forced by a variety of externally imposed changes such as increasing
142 greenhouse gas and sulfate aerosol concentrations, change in solar radiation, and forcing by volcanic
143 eruptions. Considering the land surface, except for BCC-CSM1, BCC-CSM1-M and INMCM4 all
144 models account for land use change (Table 2); likewise, except BCC models, NorESM1-ME, and
145 CESM1-BGC none of the models have an interactive land nitrogen cycle (Table 2).

146 Since considerable uncertainty as to the true forcing remains, the forcing used and its implementation
147 in the climate model is not exactly the same for all models (Jones et al. 2011). Rather, these runs
148 represent each group's best effort to simulate the 20th century climate. The models were spun up under
149 conditions representative of the pre-industrial climate (generally 1850 for almost all models, see **Table**
150 **2**). From this point, external time varying forcing, consistent with the historical period, was
151 introduced, and the simulations were extended through to year 2005.

152 Although the CMIP5 archive includes daily means for a few variables, we focus here only on the
153 monthly mean model output, since this temporal frequency is high enough to provide a reasonably
154 comprehensive picture of model performance both in terms of mean state of the system, its seasonal
155 and interannual variability, and trends.

156 In this study we focus mostly on the last 20 years of the 20th century simulations (1986–2005). During
157 this period, in fact, the observational record is most reliable and complete, largely due to the expansion
158 and advances in space-based remote sensing of vegetation greenness.

159
160
161

162 2.2 Reference data

163 The main focus of this paper is the evaluation of the land and ocean carbon fluxes. However, climatic
164 factors exert a direct control on the terrestrial and ocean carbon exchange with the atmosphere
165 (Houghton 2000; Schaefer et al. 2002), therefore we also provide an evaluation of the physical
166 variables. The main physical factors controlling the land carbon balance are the surface temperature
167 and precipitation (Piao et al. 2009), but also the cloud cover through its control on incoming radiation
168 is important for the land carbon balance; however we decided to consider only the two most important
169 variables influencing the land carbon cycle (Piao et al. 2009). In the ocean, physical fields include sea
170 surface temperature (SST), which is important for biological growth and respiration rates as well as
171 air–sea gas exchange, and mixing layer depth (MLD), which influences nutrient entrainment and the
172 average light field observed by the phytoplankton (Martinez et al. 2002).

173 Considering the land and ocean carbon fluxes, some of the available datasets used for the comparison
174 come from atmospheric inversion (discussed in section 2.2.6). To avoid pitfalls arising from weak data
175 constraints, most inversion studies have relied on regularization techniques that include the
176 aggregation of estimate fluxes over large regions (Engelen et al. 2002); as matter of fact, aggregating
177 the observed regional fluxes in space is one way to lower the uncertainty due to the limited
178 observational constraint (Kaminski et al. 2001; Engelen et al. 2002). Therefore, we only evaluate the
179 net CO₂ fluxes simulated by models at global scale or over large latitudinal bands (see below). For all
180 other model variables, the evaluation is performed at the grid level, conserving the spatial information.
181 However, when presenting the results, all model performances are averaged over the following
182 domains for land variables: Global (90S-90N), Southern Hemisphere (20S-90S), Northern Hemisphere
183 (20N-90N), and Tropics (20S-20N). Considering the ocean carbon, according to Gruber et al. (2009)
184 we aggregate results over 6 large regions: Globe (90S-90N), Southern Ocean (90S-44S), temperate
185 Southern Ocean (44S-18S), Tropics (18S-18N), temperate Northern Ocean (18N-49N) and Northern
186 Ocean (49N-90N).

187 In the following sub-sections we describe the different dataset used for the model comparison (see also
188 **Table 3**).

189 **2.2.1 Land temperature and precipitation**

190 Monthly gridded surface temperature and precipitation were constructed from statistical interpolation
191 of station observations by the Climatic Research Unit (CRU) of the University of East Anglia (New et
192 al. 2002; Mitchell and Jones 2005). CRU provides a global coverage only for land points between
193 1901 and 2006 with a spatial resolution of 0.5° (**Table 3**). Most of previous model-data comparison
194 studies use ERA40 (or other reanalysis) instead of the CRU dataset, due to the complete global land
195 and ocean coverage, and the way these reanalysis are built. Specifically, the reanalysis are a
196 combination of weather model output and a large amount of assimilated different observational data.
197 Therefore, unlike CRU that is built on statistical principles, the reanalysis are based on physical
198 principles (Scherrer 2011). Also comparison of the ERA40 dataset with the CRU land temperature
199 shows good agreement for most regions and the differences are comparatively small in comparison to
200 the model differences (Scherrer 2011). However, CRU provides data for the entire 20th century
201 allowing the evaluation of the simulated temperature and precipitation trends.

202

203 **2.2.2 Sea Surface Temperature**

204 For the Sea Surface Temperature (SST) evaluation we use the HadISST (Rayner et al. 2003), a
205 combination of monthly global SST and sea ice fractional coverage on a 1°x1° spatial grid from 1870
206 to date.

207 The SST data are taken from the Met Office Marine Data Bank (MDB), which from 1982 onward also
208 includes data received through the Global Telecommunications System. To enhance data coverage,
209 monthly median SSTs for 1871–1995 from the Comprehensive Ocean–Atmosphere Data Set
210 (COADS) were also used where there were no MDB data. HadISST temperatures are reconstructed
211 using a two-stage reduced-space optimal interpolation procedure, followed by superposition of
212 quality-improved gridded observations onto the reconstructions to restore local detail (Dima and
213 Lohmann 2010). SSTs near sea ice are estimated using statistical relationships between SST and sea
214 ice concentration (Rayner et al. 2003).

215

216 **2.2.3 Mixed Layer Depth**

217 The ocean Mixed Layer Depth (MLD) can be defined in different ways, according to the dataset used.
218 In this paper, MLD data are from the Ocean Mixed Layer Depth Climatology Dataset as described in
219 de Boyer Montégut et al. (2004). Data are available in monthly format on a $2^\circ \times 2^\circ$ latitude–longitude
220 mesh and were derived from more than five million individual vertical profiles measured between
221 1941 and 2008, including data from Argo profilers, as archived by the National Oceanographic Data
222 Centre (NODC) and the World Ocean Circulation Experiment (WOCE). In order to solve the MLD
223 overestimation due to salinity stratification, in this dataset the depth of the mixed layer is defined as
224 the uppermost depth at which temperature differs from the temperature at 10 m by 0.2°C . A validation
225 of the temperature criterion on moored time series data shows that this method is successful at
226 following the base of the mixed layer (de Boyer Montégut et al. 2004).

227

228 **2.2.4 Terrestrial Gross Primary Production**

229 Gross Primary Production (GPP) represents the uptake of atmospheric CO_2 during photosynthesis and
230 is influenced by light availability, atmospheric CO_2 concentration, temperature, availability of water
231 and nitrogen, and several interacting factors (e.g. atmospheric pollution, harvesting, insect attacks).
232 Direct GPP observations at global scale and for our reference period (1986-2005) do not exist, since in
233 the 1980s no measurement sites existed, and satellite observations of GPP were not yet available.
234 Recently, satellite derived GPP products have been developed (e.g Mao et al. 2012) but do not cover
235 the reference period.

236 Here we use GPP estimates derived from the upscaling of data from the FLUXNET network of eddy
237 covariance towers (Beer et al. 2010). The global FLUXNET upscaling uses data oriented diagnostic
238 models trained with eddy covariance flux data to provide empirically derived, spatially gridded fluxes
239 (Beer et al. 2010). In this study, we use the global FLUXNET upscaling of GPP based on the model
240 tree ensembles (MTE) approach, described by Jung et al. (2009, 2011). The upscaling relies on
241 remotely sensed estimates of the fraction of absorbed photosynthetically active radiation (fAPAR),
242 climate fields, and land cover data. The spatial variation of mean annual GPP as well as the mean

243 seasonal course of GPP are the most robust features of the MTE-GPP product, while there is less
244 confidence on its interannual variability and trends (Jung et al 2011). MTE-GPP estimates are
245 provided as monthly fluxes covering the period 1982-2008 with a spatial resolution of 0.5° (**Table 3**).

246

247 **2.2.5 LAI**

248 Leaf area index (LAI) is defined as the one-sided green leaf area per unit ground area in broadleaf
249 canopies and as one-half the total needle surface area per unit ground area in coniferous canopies
250 (Myneni et al. 2002). The LAI data set used in this study (LAI3g) was generated using an Artificial
251 Neural Network (ANN) from the latest version (third generation) of GIMMS AVHRR NDVI data for
252 the period July 1981 to December 2010 at 15-day frequency (Zhu et al. 2013). The ANN was trained
253 with best-quality Collection 5 MODIS LAI product and corresponding GIMMS NDVI data for an
254 overlapping period of 5 years (2000 to 2004) and then tested for its predictive capability over another
255 five year period (2005 to 2009). The accuracy of the MODIS LAI product is estimated to be 0.66 LAI
256 units (Yang et al. 2006); further details are provided in Zhu et al. (2012).

257

258 **2.2.6 Land-atmosphere and ocean-atmosphere CO₂ fluxes**

259 The net land-atmosphere (NBP) and ocean-atmosphere (fgCO₂) CO₂ exchange estimated by CMIP5
260 models are compared with results from atmospheric inversions of the Transcom 3 project (Gurney et
261 al. 2004; Baker et al. 2006), an intercomparison study of inversions (Gurney et al. 2002, 2003, 2004,
262 2008). Within this project a series of experiments were conducted in which several atmospheric tracer
263 transport models were used to calculate the global carbon budget of the atmosphere.

264 Transcom 3 results represent the a posteriori surface CO₂ fluxes inferred from monthly atmospheric
265 CO₂ observations at a set of GLOBALVIEW stations after accounting for the effects of atmospheric
266 transport on a prescribed a priori surface flux, which is corrected during the atmospheric inversion
267 (Gurney et al., 2003). In other words, the goal of the atmospheric inversion process is to find the most
268 likely combination of regional surface net carbon fluxes that best matches observed CO₂ within their

269 error, given values of prior fluxes and errors, after those fluxes have been transported through a given
270 atmospheric model (Gurney et al., 2003, 2008).

271 Flux estimates from atmospheric inverse models are comprehensive, in the sense that all ecosystem
272 sources and sinks, fossil fuel emissions, and any other processes emitting or absorbing CO₂ (e.g.
273 aquatic CO₂ fluxes, decomposition of harvested wood and food products at the surface of the Earth)
274 are, in principle, captured by the inversion CO₂ fluxes results.

275 Transcom 3 also provides an ensemble mean computed over 13 available atmospheric models in the
276 period 1996-2005 at a spatial resolution of 0.5°. The use of several models was motivated because
277 large differences in modelled CO₂ were found between models using the same set of prescribed fluxes
278 (Gurney et al. 2004). However it is argued that an average of multiple models may show
279 characteristics that do not resemble those of any single model, and some characteristics may be
280 physically implausible (Knutti et al. 2010). In absence of any other information to select the most
281 realistic transport models, Gurney et al. (2002) used the “between-model” standard deviation to assess
282 the error of inversions induced by the transport model errors. In addition, Stephens et al. (2007)
283 suggest that an average taken across all models does not provide the most robust estimate of northern
284 versus tropical flux partitioning. Additionally, they point to three different models as best representing
285 observed vertical profiles of [CO₂] in the Northern Hemisphere (Stephens et al. 2007). For such
286 reasons, instead of using the Transcom 3 ensemble mean and the “between-model” standard deviation,
287 we used results from the only JMA model (Gurney et al. 2003), being one of the three models
288 suggested by Stephens et al. (2007) and the only one available in our reference period 1986-2005.

289 We also use results from the Global Carbon Project (GCP, [http://www.tyndall.ac.uk/global-carbon-](http://www.tyndall.ac.uk/global-carbon-budget-2010)
290 [budget-2010](http://www.tyndall.ac.uk/global-carbon-budget-2010)), which estimates, using several models and observations, the ocean-atmosphere and
291 land-atmosphere CO₂ exchange (Le Quéré et al. 2009). These results are the most recent estimates of
292 global CO₂ fluxes for the period 1959-2008. Within this project, the global ocean uptake of
293 anthropogenic carbon was estimated using the average of four global ocean biogeochemistry models
294 forced by observed atmospheric conditions of weather and CO₂ concentration (Le Quéré et al. 2009).
295 The global residual land carbon sink was estimated from the residual of the other terms involved in the

296 carbon budget, namely the residual land sink is equal to the sum of fossil fuel emissions and land use
297 change less the atmospheric CO₂ growth and the ocean sink (Le Quéré et al. 2009). From the GCP
298 analysis, the NBP can easily be computed as the difference between the residual sink and the land use
299 change.

300 Finally, in addition to the inversion and GCP data, for the ocean-atmosphere flux we also use results
301 from Takahashi et al. (2002, 2009). This product contains a climatological mean distribution of the
302 partial pressure of CO₂ in seawater (pCO₂) over the global oceans with a spatial resolution of 4°
303 (latitude) x 5° (longitude) for the reference year 2000 based upon about 3 million measurements of
304 surface water pCO₂ obtained from 1970 to 2007 (Takahashi et al. 2009). It should be noted that
305 Takahashi et al. (2002) data are used as prior knowledge in many atmospheric inversions, suggesting
306 that the two datasets are not completely independent.

307 Although the difference between the partial pressure of CO₂ in seawater and that in the overlying air
308 ($\Delta p\text{CO}_2$) would be a better reference data set for the oceanic uptake of CO₂, in this study we have used
309 the net sea-air CO₂ flux (fgCO₂) to be consistent with the land flux component of this paper. The net
310 air-sea CO₂ flux is estimated using the sea-air pCO₂ difference and the air-sea gas transfer rate that is
311 parameterized as a function of wind speed (Takahashi et al. 2009).

312

313 **2.2.7 Vegetation and soil carbon content**

314 Heterotrophic organisms in the soil respire dead organic carbon, the largest carbon pool in the
315 terrestrial biosphere (Jobbagy and Jackson 2000); therefore the soil carbon, through the heterotrophic
316 respiration, represents a critical components of the global carbon cycle.

317 There are several global datasets that include estimates of soil carbon to a depth of 1 m. Generally,
318 there are two different approaches to creating such datasets: (1) estimation of carbon stocks under
319 natural, or mostly undisturbed, vegetation using climate and ecological life zones (2) extrapolation of
320 soil carbon data from measurement in soil profiles using soil type (Smith et al., 2012).

321 The Harmonized World Soil Database (HWSD) developed by Food and Agriculture Organization of
322 the United Nations (FAO 2012) and International Institute for Applied Systems Analysis (IIASA) is

323 the most recent, highest resolution global soils dataset available. It uses vast volumes of recently
324 collected regional and national soil information to supplement the 1:5000000 scale FAO-UNESCO
325 Digital Soil Map of the World. It is an empirical dataset and it provides soil parameter estimates for
326 topsoil (0–30 cm) and subsoil (30–100 cm), at 30 arc-second resolution (about 1 km).

327 The CMIP5 ESMs do not report the depth of carbon in the soil profile, making direct comparison with
328 empirical estimates of soil carbon difficult. For our analysis, we assumed that all soil carbon was
329 contained within the top 1 meter. Litter carbon was a small fraction of soil carbon for the models that
330 reported litter pools; thus, we combined litter and soil carbon for this analysis and refer to the sum as
331 soil carbon.

332 For the HWSD, the major sources of error are related to analytical measurement of soil carbon,
333 variation in carbon content within a soil type, and assumption that soil types can be used to extrapolate
334 the soil carbon data. Analytical measurements of soil carbon concentrations are generally precise, but
335 measurements of soil bulk density are more uncertain (Todd-Brown et al. 2012).

336 In addition to the soil carbon, also the vegetation carbon is a key variable in the global carbon cycle. In
337 the 1980s, Olson et al. (1985) developed a global ecosystem-complex carbon stocks map of above and
338 below ground biomass following more than 20 years of field investigations, consultations, and
339 analyses of the published literature. Gibbs (2006) extended Olson et al.'s methodology to more
340 contemporary land cover conditions using remotely sensed imagery and the Global Land Cover
341 Database (GLC, 2000). For this analysis we used the data created by Gibbs (2006), with a spatial
342 resolution of 0.5 degree.

343

344 **2.2.8 Oceanic Net Primary Production**

345 Oceanic integrated net primary production (NPP or intPP) is the gross photosynthetic carbon fixation
346 (photosynthesis), minus the carbon used in phytoplankton respiration. NPP is regulated by the
347 availability of light, nutrients and temperature and affects the magnitude of the biological carbon
348 pump. Oceanic export production (EP) exerts a more direct control on air-sea CO₂ fluxes, however

349 due to limited EP data we assess models compared to NPP estimates. In addition, we used the NPP to
350 be consistent with the use of GPP in the land section of the study, however often it is argued that a
351 proper validation of biological oceanic models should be based on the comparison of surface
352 chlorophyll concentration rather than phytoplankton primary production.

353 We used NPP estimated from satellite chlorophyll by the Vertically Generalised Production Model
354 (VGPM) (Behrenfeld and Falkowski 1997). The VGPM computes marine NPP as a function of
355 chlorophyll, available light, and temperature dependent photosynthetic efficiency. The NPP, estimated
356 with the Sea-viewing Wide Field-of-view Sensor (SeaWiFS) from 1997-2007, is a monthly dataset
357 with a spatial resolution of about 6 km.

358 As well as previous datasets (GPP-MTE, LAI, Transcom 3 and GCP data derived CO₂ fluxes), it
359 should be noted that although this is one of the best available global NPP products it is not actually
360 data, rather a model estimate dependent on parameterisations (the temperature dependent assimilation
361 efficiency for carbon fixation and an empirically determined light dependency term).

362

363 **2.2.9 Uncertainty in the observed dataset**

364 One limitation of most of the above chosen reference datasets is that it is in general difficult to
365 estimate their observational errors (except for Bayesian inversions that explicitly come with
366 uncertainty estimates). Sources of uncertainty include random and bias errors in the measurements
367 themselves, sampling errors, and analysis error when the observational data are processed through
368 models or otherwise altered. In short, the quality of observational measurements varies considerably
369 from one variable to the next (Gleckler et al. 2008) and is often not reported.

370 Errors in the reference data are frequently ignored in the evaluation of models. It is often argued that
371 this is acceptable as long as these errors remain much smaller than the errors in the models (Gleckler
372 et al. 2008). A full quantitative assessment of observational errors by the estimation of its impact on
373 the model ranking is however beyond the scope of this study.

374 Nevertheless, we would report that some of the reference data used for model validation show relevant
375 problems. For instance, the ocean NPP is calculated from SeaWiFS satellite chlorophyll data which
376 contains a significant uncertainty of ~30% (Gregg and Casey, 2004).

377 The MLD and SST data sets have a lack of observations in the Southern Ocean compared to other
378 regions, hence the uncertainty in these data sets is greatest in the Southern Ocean (De Boyer Montégut
379 et al. 2004).

380 It is also argued that CRU has been designed to provide best estimates of interannual variations rather
381 than detection of long-term trends and (Mitchell and Jones 2005).

382 Finally, the soil databases are based on a limited number of soil profiles and extrapolated to other
383 areas according to soil type. Climate or land cover and management are usually not considered so that
384 these data have high associated uncertainty.

385

386 **2.3 Assessment of model performances**

387 A series of measures of analysis are employed here for model evaluation and ranking; the model
388 performances are evaluated at every grid point and then aggregated over the different land and ocean
389 sub-domains. However, as previously described in section 2.2 the atmospheric inversion estimates do
390 not provide any reliable information at grid cell level, therefore for land-atmosphere and ocean-
391 atmosphere CO₂ fluxes only the evaluation is performed using regional averages of the CO₂ fluxes. In
392 the following we describe the diagnostics used for model evaluation and the metrics used for model
393 ranking.

394

395 **2.3.1 Diagnostics definition**

396 Climatic trends for land surface temperature, land precipitation and SST are estimated by the linear
397 trend value obtained from a least square fit line computed for the full period 1901-2005 of data, while
398 for the LAI, and GPP due to the unavailability of data before 1982, the trends are computed in the
399 same way but for the reference period 1986-2005.

400 Looking at simulated interannual variability, the root-mean square error (RMSE) is not an appropriate
401 measure for characterizing this aspect of model performance because there is no reason to expect
402 models and observations to agree on the phasing of internal (natural unforced) interannual variations
403 (e.g., the timing of El Niño events) (Lin 2007; Gleckler et al. 2008). Standard measures of model
404 mean variability such as the ratio of the standard deviation of the model means divided by the standard
405 deviation of the means in the reference data set suffer from the serious problem that regions with too
406 large/small IAV can cancel out and therefore give a too optimistic picture of model performance
407 (Gleckler et al. 2008; Scherrer, 2011). To avoid these cancellation effects the Model Variability Index
408 (MVI) as introduced by Gleckler et al. (2008) and Scherrer (2011) is used here to analyze the
409 performance for each model, as given by:

410

411

$$MVI_{x,y}^M = \left(\frac{s_{x,y}^M}{s_{x,y}^O} - \frac{s_{x,y}^O}{s_{x,y}^M} \right)^2 \quad (1)$$

412

413 where $s_{x,y}^M$ and $s_{x,y}^O$ are the standard deviations of the annual time series of models and observation for
414 a given variable, at each grid-point (x, y). Using this simple index of performance, we compare each
415 model's variability at every grid cell and then average over the different sub-domains in the period
416 1986-2005. Perfect model–reference agreement would result in a MVI value of 0. The MVI provides a
417 good measure to assess differences between model and reference data standard deviations and allow us
418 to identify consistent biases in the standard deviations of single models. The definition of a MVI
419 threshold value that discriminates between ‘good’ and ‘bad’ is somewhat arbitrary. Scherrer (2011), in
420 his CMIP3 validation paper, defined a $MVI < 0.5$ as a good representation of IAV. In this paper we
421 use the same threshold, although in case of biological variables the MVI could be much larger than
422 0.5.

423 Often it is also argued that a 20-year window could be not long enough for characterizing the long
424 time-scale variance of a model (Wittenberg 2009; Johnson et al. 2011). This means that when the MVI
425 is being computed over the last 20 years there is an implicit assumption that the variability is

426 representative of the full length of the simulation. To test whether this is the case, we also have
 427 accounted the MVI for the physical variables over the period 1901-2005, and we found a relevant
 428 reduction in the MVI of global surface temperature, precipitation and SST compared to the MVI
 429 computed in the period 1986-2005 (not shown). This confirms that a 20-year windows is pretty
 430 marginal in characterizing what the actual variability of the model is. However, considering this work,
 431 while for climate variables it is possible to compute the MVI from the beginning of last century, in
 432 case of all the other variables the data are limited to the only last 20 years, therefore we decided to
 433 analyze the MVI over the period 1986-2005 to be consistent between physical and biological
 434 variables.

435

436 **2.3.2 Metrics definition**

437 Two different skill scores are used for the model ranking. In the case of mean annual cycle we check
 438 the ability of models to reproduce both the phase and amplitude of the observations during the period
 439 1986-2005. Starting for monthly mean climatological data, we use the centered root-mean square
 440 (RMS) error statistic to account for errors in both the spatial pattern and the annual cycle. Given a
 441 model (M) at the grid-point (x, y) and the reference dataset at the same location ($O_{x,y}$), the errors of the
 442 model m ($E_{x,y}^{m^2}$) is calculated as follow:

443

$$444 \quad E_{x,y}^{m^2} = \frac{1}{N} \sum_{t=1}^N \left[\left(M_t^{x,y} - \overline{M}^{x,y} \right) - \left(O_t^{x,y} - \overline{O}^{x,y} \right) \right]^2 \quad (2)$$

445

446 where t corresponds to the temporal dimension, N is the number of months (i.e. 12), and $\overline{M}^{x,y}$ and
 447 $\overline{O}^{x,y}$ are the mean values of the model and reference data, respectively, at the grid point (x,y) .

448 In order to get an error between 0 and 1 (where 0 corresponds to poor skill and 1 perfect skill), we
 449 normalize the error of the model m dividing it by the maximum error computed considering all the
 450 models at the grid point (x,y) . Therefore the relative error (Re) of a single model m becomes:

451

$$\text{Re}_{x,y}^m = 1 - \frac{E_{x,y}^{m^2}}{\max(E_{x,y}^2)} \quad (3)$$

452

453 Unlike Gleckler et al. (2008) that normalized their seasonal skill score by the median of the RMS
 454 errors computed considering all the models, here we decided to divide by the maximum RMS error in
 455 order to have a skill score ranging between 0 and 1.

456 The second skill score used for model ranking is based on the comparison of Epanechnikov kernel-
 457 based probability density functions (PDFs; Silverman 1986) of models with observations (Perkins et
 458 al., 2007). This skill score provides a very simple but powerful measure of similarity between data and
 459 observations since it allows to compare both the mean state and the interannual variability of a given
 460 variable by calculation of the common area under the two PDFs (Maximo et al. 2008). If models
 461 perfectly reproduce the observed condition, the skill score would equal 1, which is the total area under
 462 a given PDF. On the contrary, if a model simulates the observed PDF poorly, it will have a skill score
 463 close to 0, namely there is not any overlap between the observed and modelled PDF. Note that despite
 464 this seeming to be similar to the Kolmogorov–Smirnov test for the similarity of PDFs, there is a
 465 fundamental difference between them: the Kolmogorov–Smirnov test is based on the maximum
 466 difference between cumulative PDFs, whilst the skill score is based on the common area under the
 467 PDF curves (Errasti et al. 2011). Starting from yearly data, and given $Z_{x,y}$ the common area under the
 468 observed PDF ($z_{x,y}^O$) and the simulated PDF ($z_{x,y}^M$) at the grid point (x,y):

469

$$Z_{x,y} = \min(z_{x,y}^O, z_{x,y}^M) \quad (4)$$

471

472 the skill score at a given geographical location is computed in the following way:

473

$$s_{x,y} = w^* \int_1^N Z_{x,y} \quad (5)$$

474

475 where $s_{x,y}$ is the numerical value of the skill score ($0 \leq s_{x,y} \leq 1$), N is the number of intervals used
476 discretize the PDF estimated by means of the Epanechnikov kernels (in this study, $N=100$), and w is a
477 weight (**Table 4**) introduced in order to give lower weight at the grid points where models are
478 expected to poorly reproduce the observations. In fact, models are expected not to faithfully reproduce
479 the observation in some specific regions such as in area of complex topography (i.e. in mountainous
480 regions the coarse resolution of models does not allow to correctly reproduce the right temperature
481 pattern) or over specific surface cover (ex. costal regions, ice-covered area, sparse vegetated points).
482 This measure is however imperfect: a model that is able to simulate the tails of a distribution well (i.e.
483 extreme events like heat waves or cold spells, drought or heavy rain) would be very valuable, but if it
484 simulates the more common regions of the PDF poorly it could score badly overall. Conversely, a
485 model could appear skilful by simulating all the probabilities one or two standard deviations from the
486 mean while being poor towards the tails (Maximo et al. 2008).

487 In general, models that properly simulate the observed mean value of a given variable, namely they
488 fall into the range of $\pm 1\sigma$ of the observed PDF, are able to reproduce at least the 68.2% of the
489 reference data. Maximo et al. (2008) defined as ‘adequate’ those models with a skill score greater than
490 0.9; this value was chosen since it allows identification of not only models that correctly capture the
491 mean value, but also those models that capture a considerable amount of the interannual variability.

492 However, a threshold of 0.9 is too large when aggregating the skills over sub-regions, therefore in this
493 study we consider a model as having relevant skill when it simulates at least 1σ of the observed PDF.
494 This method has already been used for AR4 ranking over Australia (Perkins et al. 2007; Maxino et al.
495 2008), Spain (Errasti et al. 2011) and CORDEX regions (Jacob et al. 2012). In their study, Errasti et
496 al. (2011) removed all the points below a threshold value of 0.7 to avoid models characterized by very
497 poor values affecting the overall score. However, this latter procedure is questionable since over large
498 sub-regions removing the points with a skill lower than 0.7 will favour only the points with good
499 agreement to observations and any poor performance of models related to severe bias will not be
500 regarded. Additionally, removing all the points below a particular low threshold (e.g. 0.05) can lead to
501 an overestimation of a model’s skill. For this reason, in order to compute the regional skill score we

502 apply a weighted mean, giving relatively large weights to points where the skill score exceed 0.75 and
503 low importance to points where the score is poor (**Table 4**). We also have computed the ranking
504 without weighting the skill scores (not shown) and we found that the weights only change the models
505 skill values, leaving unchanged the overall ranking.

506 In addition, for those variables we are unable to build the PDFs due to the lack of yearly data (e.g.soil
507 carbon, vegetation carbon and MLD) the skill score is computed using the bias between a given model
508 (M) and the reference data (O). Given the bias (B) of the model m at the grid point (x,y):

509

$$510 \quad B_{x,y}^m = |M_{x,y} - O_{x,y}| \quad (6)$$

511

512 the skill score is computed following the equation 3. It should also be noted that normalizing the skill
513 score calculations in this way yields a measure of how well a given model (with respect to a particular
514 reference data set) compares with the typical model error, namely it leads to a more optimistic skill
515 compared to the PDF-based skill score.

516

517 **3. CMIP5 MODELS PERFORMANCES DURING THE 20th CENTURY**

518 Since the simulation of physical variables will affect the simulation of the carbon cycle, we first
519 briefly show how CMIP5 models reproduce these variables and then we focus on the carbon cycle
520 performances. In particular, the evaluation of climatic variables is needed to assess whether any bias in
521 the simulated carbon variables can be related to poor performances of the ESMs reproducing physical
522 variables or is mainly due to the poor representation of some biogeochemical processes into the
523 biological components of ESMs.

524

525 **3.1 Land surface temperature, land precipitation, SST and MLD evaluation**

526 The temporal evolution of global mean surface temperature, for the land points only (without
527 Antarctica), is shown in **Figure 1** (upper panel) for the CMIP5 simulation as well as for the
528 observations derived data-product (CRU).

529 Like for the AR4 results (Solomon et al. 2007), the CMIP5 simulations of 20th century that incorporate
530 anthropogenic forcing (including increasing greenhouse gas concentrations and aerosols
531 concentrations), as well as natural external forcing (volcanoes, change in solar radiation) are able to
532 correctly reproduce the observed temperature anomaly, the observed data being systematically within
533 the grey shading representing the range of variability of CMIP5 models. Plotting the CMIP5
534 temperature time series as anomalies with respect to the base period 1901–1930, all the models exhibit
535 a general upward temperature trend (**Figure 1**); the net temperature increase over the historical period
536 is determined primarily by a balance between the warming caused by increased GHGs and the cooling
537 over some regions associated with increasing aerosols.

538 The ensemble mean suggests that CMIP5 models correctly reproduce the transient drop in global
539 mean temperatures owing to main volcanic eruptions followed by gradual recovery over several years
540 (**Figure 1**). Larger interannual variations are seen in the observations than in the ensemble mean,
541 consequently, mainly during the first 50 years, the observed evolution lies outside the 90% confidence
542 limits diagnosed from the CMIP5 ensemble spread (red shading). This result is related with the multi-
543 model ensemble mean that filters out much of the natural variability (unforced and forced, i.e.
544 volcanic, solar, and aerosols) simulated by each of the CMIP5 models. In addition, the ensemble
545 spread (i.e. range of model variability) shows an increase with lead time, reflecting the loss of
546 predictability associated with the different climate sensitivities, i.e. with the different model responses
547 to forcing (Solomon et al. 2007; Hawkins and Sutton 2009).

548 In **Figure 1** (lower panels) we present, for each model, the mean surface temperature over the period
549 1986-2005, the MVI computed in the same temporal period, and the trend during 1901-2005. On the
550 x-axis, models falling at the left (right) of observations indicate a cold (warm) bias, while on the y-axis
551 models above (below) the observations have a stronger (lower) trend than observations.

552 The comparison with CRU data shows that in general few models have a warm bias (within 1 °C),
553 while most of the models have a cold bias (**Figure 1**). Poor performances have been found for the
554 INMCM4 model: specifically, its global cold bias is around 2.3 °C, with the minimum found in
555 northern hemisphere (1.8 °C), and a maximum in the tropics (3.2 °C). Conversely, the best

556 performances have been found in IPSL-CM5A-MR, MPI-ESM-LR, MPI-ESM-MR and GFDL-
557 ESM2M models that are consistently closer to CRU data. Looking at the trends, however, IPSL-
558 CM5A-MR and GFDL-ESM2M generally seem to be closer to the observations than MPI-ESM-LR
559 and MPI-ESM-MR.

560 On the other hand, GFDL-ESM2M shows the poorest performances reproducing the observed IAV,
561 having a MVI larger than 1.4 at global scale, while only few models show a MVI lower than 0.5
562 (indicating a good representation of the simulated IAV). The best results in terms of simulated IAV
563 are found in the Northern Hemisphere, where several models show a MVI lower than 0.5; conversely,
564 in the tropics most of models have a MVI larger than 1.

565 In **Figure 2** (upper panel) we compare precipitation changes during the 20th century over land surfaces
566 as reconstructed from station data (CRU) and simulated by individual CMIP5 models; shown are
567 annual anomalies with respect to the period 1901-1930.

568 The CMIP5 models correctly reproduce the precipitation variability: specifically, for most of the time
569 the reference data falls inside the range of variability of models, identified by the grey shading.
570 Explosive volcanoes eruptions prescribed to models introduce anomalies in the simulated historical
571 precipitation as seen by temperature; a clear precipitation reductions around the year 1991 associated
572 with the Pinatubo eruptions is found in both CRU data and CMIP5 simulations.

573 Looking at the multi-model ensemble mean, it does not reproduce the amplitude of temporal evolution
574 in 20th century terrestrial precipitation (see also Allan and Soden 2007; John et al. 2009; Liepert and
575 Previdi 2009), being the observations larger than the 90% confidence limits diagnosed from the
576 ensemble spread (blue shading). As already described for the temperature, the averaging process
577 partially filters out the IAV.

578 The evaluation of precipitation for every model is given in **Figure 2** (lower panels). The best
579 performances reproducing global precipitation are found in IPSL-CM5B-LR, BCC-CSM1-M and MPI
580 models. BCC-CSM1, HadGEM2-ES, and HadGEM2-CC models show a slight wet bias (less than 40
581 mm/y), while CanESM2, IPSL-CM5A-LR and IPSL-CM5A-MR have a dry bias of about 80 mm/y.
582 All the other models overestimate global precipitation with a bias of about 100 mm/y. In the Southern

583 Hemisphere several models match the CRU data well, while IPSL-CM5A-LR and IPSL-CM5A-MR
584 showing a dry bias, and NorESM1-ME and CESM1-BGC have a strong wet bias. In the tropical
585 region, quite a few models are able to reproduce the mean precipitation, while in the Northern
586 Hemisphere, except CanESM2, all the models show a wet bias.

587 Looking at the IAV none of the models has a MVI close to the threshold of 0.5; the best results are
588 found in the Southern Hemisphere for the Hadley models. As expected, the worst performances
589 reproducing the precipitation IAV occur in the tropical region, reflecting the inability of these models
590 in reproducing the interannual variations in the hydrological cycle (Lin 2007; Scherrer 2011); as
591 already suggested by Wild and Liepert (2010) inadequacies in the simulation of surface radiation
592 balance may contribute to the poor simulation of IAV during the 20th century. In addition,
593 shortcomings in the representation of the natural variability in atmosphere/ocean exchanges of energy
594 and water that result in variations of convection and consequently in cloudiness and humidity can
595 contribute to a poor representation of precipitation IAV in CMIP5 models (Lin 2007; Wild and Liepert
596 2010).

597 The evaluation of the trend show that at global scale and in the tropical region several models are close
598 to CRU, while in the Southern and Northern Hemisphere in general the models are not capable to
599 capture the observed wettening trend. This is particularly evident in the Southern Hemisphere where
600 the CMIP5 models show an ensemble trend around zero, while the CRU data gives a positive trend of
601 5.5 mm/decade over the period 1901-2005.

602 In order to understand the source of this mismatch between CMIP5 models and CRU data, we also use
603 precipitation data from the Global Precipitation Climatology Project (GPCP) (Adler et al., 2003) for a
604 further comparison. The GPCP trend in the Southern Hemisphere during the period 1979-2005 is -
605 0.4 ± 9.5 mm/decade, while CRU shows a strong positive trend of 13 ± 10 mm/decade over the same
606 period; this suggests that the two datasets show a completely different trend. Although these results
607 are affected by a large uncertainty, it is often argued on the reliability of CRU for the long term trends
608 (Mitchell and Jones 2005).

609 **Figure 3** (upper panel) shows the temporal evolution of global mean SST. Unlike the observed surface
610 temperature that is scattered around the CMIP5 ensemble mean and falls in the middle of the gray
611 shading, the observed SST is markedly above the ensemble mean, particularly during the period 1940-
612 1970.

613 The CMIP5 ensemble mean shows an increasing trend, with declining periods in the early 1960's and
614 1990's as a consequence of the cooling due to the Agung and Pinapubo eruptions, and a sharper rise in
615 the post 1960 period. The HadISST data shows an overall more linear increase than the CMIP5 model
616 ensemble mean. Similar to the land temperature trend, the SST trend is primarily a balance between
617 warming caused by GHG concentrations in the atmosphere and cooling resulting from aerosol
618 emissions, modulated by the heat uptake by the ocean. Thus, factors regulating the heat uptake by the
619 ocean such as changes in the thermohaline circulation, and upwelling have an effect on SST.

620 Aerosols from volcanic eruptions can lower SST at the time of the eruption and for a few years
621 following the eruption. The CMIP5 models simulate a drop in SST as a result of the main volcanic
622 eruptions, as can be seen in **Figure 3** (upper panel).

623 **Figure 3** (lower panels) shows that the increasing trend in SST is evident in all regions for all the
624 CMIP5 models except in the high latitude Southern Hemisphere where GFDL-ESM2M shows a
625 cooling and the high latitude Northern Hemisphere where GFDL-ESM2G displays a cooling. It should
626 also be noted that the trend for BNU-ESM has been computed over the period 1950-2005, rather than
627 in the period 1901-2005, and it explains why this model exhibits this large trend compared to both
628 observations and other CMIP5 models.

629 Most of the models show a cold bias, particularly in the Northern Hemisphere, and a lower trend than
630 the observations, particularly in the Southern Hemisphere. At the global scale most of the models
631 display a cold bias, with IPSL-CM5A-LR having the largest cold bias (1 °C). All models except IPSL-
632 CM5A-LR, IPSL-CM5A-MR, MPI-ESM-LR and BCC-CSM1 show a lower trend than observations,
633 with the lowest trend being in HadGEM2-ES, which has an increase of 0.4 °C/decade less than is seen
634 in observations. The interannual variability is fairly well simulated by CMIP5 models, with a MVI
635 lower than 1.5 in most of the sub-domains and for most of the models; however, severe problems

636 reproducing the IAV are found in the high latitude Northern Hemisphere where most of models
637 generally show a MVI larger than 2. Since we also found poor performances for a few models in
638 reproducing the IAV in the Southern Hemisphere, the poor skill could be related to sea ice cover that
639 affects both measured and modelled SST.

640 As already described in section 2.2.3 the reference MLD dataset is a climatology, therefore it is not
641 possible to provide the same evaluation used for the other physical variables. However, the MLD
642 seasonal cycle allows identification of some importance differences between models, and also allows
643 the identification of possible bias when compared to observations. **Figure 4** shows the seasonal
644 performance of each of the models in comparison to observed MLD (De Boyer Monégut et al., 2004).
645 In general all the models simulate the basic seasonal cycle. However, in all the models (except the
646 Hadley models) there is a consistent slight deep bias at the global scale, with a strong bias found in
647 MPI-ESM-LR and MPI-ESM-MR.

648 The large global bias found in MPI models is related to a very deep mixed layer in the Weddell gyre,
649 the aggregation of regions means that the entire Southern Ocean MLD is over estimated during austral
650 winter. However it must also be considered that deep mixed layers of up to 800m are indeed observed
651 in this region (Rintoul and Trull 2001). In addition, there is a lack of observations in the Southern
652 Ocean compared to other regions and therefore there are biases in the data, which is based on
653 individual profiles of temperature and salinity.

654 The biases are less pronounced in the Northern Hemisphere, however several models display a deep
655 bias, particularly in winter. Most of the models show a shift in the timing of the maximum and
656 minimum MLD compared to the observations, with the maximum occurring 1 month later. This would
657 have a knock on effect on other components of the model, such as the timing of the spring bloom.
658 Summer MLDs are better simulated as there is less variability at this time, with summer depths
659 between approximately 10 and 50m in all sub-regions.

660 It should also be noted that some inconsistencies between CMIP5 models might arise due to differing
661 definitions of mixed layer depth between the CMIP5 modelling groups.

662

663 3.2 CMIP5 land carbon

664 The land-atmosphere CO₂ flux, or net exchange of carbon between the terrestrial biosphere and the
665 atmosphere (NBP), represents the difference between carbon uptake by photosynthesis and release by
666 plant respiration, soil respiration and disturbance processes (fire, windthrow, insects attack and
667 herbivory in unmanaged systems, together with deforestation, afforestation, land management and
668 harvest in managed systems) (Denman et al. 2007). In **Figure 5** we compare the temporal evolution of
669 simulated global land-atmosphere CO₂ flux with the GCP global carbon budget estimates (Le Quéré et
670 al. 2009). Mainly thanks to CO₂ fertilization effect, the CMIP5 ensemble mean shows increasing
671 global land CO₂ uptake between 1960 and 2005 with large year-to-year variability. The temporal
672 variability of the land carbon is primarily driven by variability in precipitation, surface temperature
673 and radiation, largely caused by ENSO variability (Zeng et al. 2005). Specifically, the observed land
674 carbon sink decreases during warm climate El Niño events and increases during cold climate La Niña
675 and volcanic eruption events (Sarmiento et al. 2009). Consistent with surface temperature results
676 (**Figure 1**), CMIP5 models do capture the right NBP response after volcanic eruptions, but are not
677 meant to reproduce the observed phase of ENSO variability (**Figure 5**).

678 The CMIP5 multi-model ensemble land-atmosphere flux (\pm standard deviation of the multi-model
679 ensemble) evolved from a small source of -0.31 ± 0.52 PgC/y over the period 1901-1930 (with a mean
680 year-to-year variability of ± 0.33 PgC/y) to a sink of 0.7 ± 0.6 PgC/y in the period 1960-2005 (with a
681 mean yearly variability of ± 0.69 PgC/y), while GCP estimates show a weaker land sink of 0.36 ± 1
682 PgC/y during the latter period. As already shown for the physical variable, the GCP IAV (± 1 PgC/y) is
683 larger than the IAV of multi-model ensemble (± 0.6 PgC/y) owing to the averaging process that
684 partially filters out the IAV.

685 At the regional level, the evaluation is performed against the atmospheric inversions, the GCP
686 estimate being only global. Individual model performances reproducing the land-atmosphere CO₂
687 fluxes over different regions are given in **Figure 6**. The global value of land-atmosphere flux from
688 JMA atmospheric CO₂ inversion in the period 1986-2005 is 1.17 ± 1.06 PgC/y, with GCP showing a
689 slightly lower global mean (0.75 ± 1.30 PgC/y).

690 As shown in **Figure 6** quite a few models correctly reproduce the global land sink: in particular,
691 MIROC-ESM (0.91 ± 1.20 PgC/y) IPSL-CM5A-LR (0.99 ± 1.18 PgC/y), IPSL-CM5A-MR (1.27 ± 1.54
692 PgC/y), HadGEM2-CC (1.33 ± 1.44 PgC/y), MIROC-ESM-CHEM (1.45 ± 1.21 PgC/y), and BNU-ESM
693 (1.55 ± 1.37 PgC/y) simulate global NBP within the range of reference datasets. CanESM2 (0.31 ± 2.32
694 PgC) underestimates the land sink, as does NorESM1-ME (-0.09 ± 1.03 PgC/y) and CESM1-BGC ($-$
695 0.23 ± 0.78 PgC/y), these latter models showing a global carbon source in our reference period, in
696 contradiction with the atmospheric inversion and GCP estimates. Despite showing a realistic mean
697 uptake, GFDL-ESM2M (0.67 ± 4.53 PgC/y) has severe problems reproducing the IAV, GFDL-ESM2G
698 (0.72 ± 2.58 PgC/y) showing a strong reduction in IAV compared to GFDL-ESM2M.

699 In the Transcom 3 inversions the Southern Hemisphere land is found to be either carbon neutral or a
700 slight source region of CO₂ (-0.25 ± 0.23 PgC/y) potentially due to deforestation; CMIP5 results in
701 general put a slight carbon sink in this region and only a few of the models (IPSL-CM5A-MR, IPSL-
702 CM5A-LR, CESM1-BGC, and MIROC-ESM) agree with observations (**Figure 6**).

703 Inversions place a substantial land carbon sink in the Northern Hemisphere (2.22 ± 0.43 PgC/y), while
704 tropical lands are a net source of carbon (-0.8 ± 0.75 PgC/y) due to deforestation.

705 Looking at the Northern Hemisphere all CMIP5 models predict a CO₂ sink, despite an overall
706 underestimation. Possible reasons for this underestimation could be the poor representation of forest
707 regrowth from abandoned crops fields (Shevliakova et al. 2009), as well as the absence of sinks due to
708 nitrogen deposition for most models (Dezi et al. 2010). It should also be noted that Stephens et al.
709 (2007) found JMA having a weaker sink in the Northern Hemisphere compared to the other inversion
710 datasets, therefore using an other inversion model from TRANSCOM would further increase the
711 mismatch between CMIP5 models and the inversion estimates over this sub-domain.

712 Over the tropical region several models simulate a carbon source, i.e. CESM1-BGC (-0.24 ± 0.55
713 PgC/y), MIROC-ESM (-0.24 ± 0.79 PgC/y), NorESM1-ME (-0.11 ± 0.74 PgC/y), and GFDL-ESM2G ($-$
714 0.03 ± 1.52 PgC/y), the rest of the ESM simulating a tropical sink, with IPSL-CM5B_LR (0.97 ± 1.30
715 PgC/y) simulating the strongest carbon sink.

716 In **Figure 7** the seasonal evolution of simulated land-atmosphere CO₂ fluxes is compared against the
717 JMA atmospheric inversion estimates. While at global scale and in the Northern Hemisphere only
718 CanESM2 has serious problems reproducing the net uptake of carbon during spring and summer
719 months due to increasing GPP over respirations and the release of carbon during autumn and winter
720 months owing to respiration processes, in the Southern Hemisphere and in the tropics some models do
721 not capture the right seasonal cycle. The performances of CMIP5 models are particularly poor in the
722 tropics, where most of the models are shifted by a few months or are even anti-correlated with
723 observations. Looking at surface climate, quite a few models do correctly reproduce the right phase of
724 temperature and precipitation in the tropics, therefore this suggests that the poor performances
725 reproducing the right NBP phase are not directly related with bad skills simulating surface climate.
726 Among other possibilities, missing or coarse parameterization of harvesting, fires and LUC might
727 helps to explain the seasonal cycle discrepancy between models and data, as well as the well known
728 problems related to tree rooting depth (Saleska et al. 2003; Baker et al. 2008). Additionally, it should
729 also be noted that there are no CO₂ station data in the tropics, and consequently the seasonal cycle
730 estimates might suffer from large uncertainty (Gurney et al. 2004). It is also remarkable that in the
731 tropics the amplitude of the NBP seasonal cycle is small, therefore it is partially expected that models
732 do not perfectly reproduce the flat temporal evolution.

733 In the following, we try to identify the causes that might lead to wrong land-atmosphere CO₂ fluxes,
734 namely we check how CMIP5 models reproduce the GPP, the LAI, and soil and vegetation carbon
735 pools. Note that like GPP, the heterotrophic respiration (RH) is a key variables affecting NBP;
736 however, owing to the lack of global datasets, the RH evaluation is not performed in this study.

737 The comparison of GPP simulated by CMIP5 models with estimates derived from FLUXNET site-
738 level observations using a multiple tree ensemble (MTE) upscaling approach (Jung et al. 2009, 2011)
739 shows that all the models overestimate the GPP over the period 1986-2005 (**Figure 8**). In general we
740 can identify two groups of models: the first group has a mean global GPP value ranging from 106 to
741 140 PgC/y, which despite an overall overestimation is reasonably similar to the value of 119_{±6} PgC/y

742 found in MTE (where 6 PgC/y is the uncertainty due to the different approaches used to estimate the
743 MTE-GPP), and a second group that has a mean global GPP value greater than 150 PgC/y.

744 Using eddy covariance flux data and various diagnostic models (a similar approach used by Jung et al.
745 2009), Beer et al. (2010) provide an observation-based estimate of this flux at 123 ± 8 PgC/y in the
746 period 1998-2005 consistent with result of Jung et al. (2009), while MODIS GPP estimates (Mao et al.
747 2012) indicate a mean value of 114 PgC/y over the period 2000-2005. These results suggest that IPSL,
748 GFDL and MPI models strongly overestimate the global GPP (**Figure 8**). We note that recent studies
749 suggest that current estimates of global GPP of 120 PgC/y may be too low, and that a best guess of
750 150–175 PgC/y (Welp et al. 2011) or 146 ± 19 PgC/y (Koffi et al. 2012) better reflects the observed
751 rapid cycling of CO₂. In light of these recent results, one could suggest that the best CMIP5 models
752 are those having a global GPP value greater than 150 PgC/y. However it is argued that Welp et al.
753 (2011) have used only a limited number of observations and a very simple model for their studies,
754 while Koffi et al. (2012) cannot distinguish the best estimate of 146 ± 19 PgC/y from a different
755 assimilation experiment yielding a terrestrial global GPP of 117 PgC/y. For such reasons our reference
756 dataset for GPP still remains the MTE-GPP of Jung et al. (2011).

757 With the clear exception of high latitudes, annual GPP or LAI zonal means follow precipitation zonal
758 distributions, i.e. more productive ecosystems are found in correspondence of precipitation maxima.
759 Therefore, as a first approximation, the precipitation is the main limiting factor for the photosynthesis
760 across the globe, temperature being mainly limiting at high latitudes (Piao et al. 2009). In fact too high
761 temperatures could produce a negative effect on GPP, while a wet bias would generally be a benefit
762 for the GPP. Looking at **Figure 2**, we can exclude that the bias in GPP is caused by a wet bias in
763 precipitation, since the models that systematically overestimate the GPP are in fact the closer to the
764 observed precipitation. Therefore there are other reasons explaining the systematic overestimation of
765 global mean GPP in all the CMIP5 models. Firstly, most of these models do not consider nutrient
766 limitation on GPP (Zaehle et al. 2010; Goll et al. 2012); it should be noted that the few models
767 simulating the N cycling are the closer to the reference data. Second, the parameterization of the
768 impact of tropospheric ozone on reducing GPP is not implemented yet in the models; Sitch et al.

769 (2007) and Wittig et al. (2009) quantified that ozone leads to a mean global GPP reduction of about
770 20% during the historical period as compared with a simulation without elevated tropospheric ozone.
771 Finally the original FLUXNET stations data sets used in the MTE approach are affected by
772 uncertainties originating from u^* filtering (Papale et al. 2006), gap-filling (Moffat et al. 2008), and
773 flux partitioning (Reichstein et al. 2005; Lasslop et al. 2009). In addition, uncertainties increase when
774 extrapolating to the globe, which also carries uncertainties related to the accuracy and spatial-temporal
775 consistency of global forcing data (Jung et al. 2011).

776 A further comparison with results from different process-based terrestrial carbon cycle models forced
777 offline by observed climate (i.e. CRU) shows that the land surface components of the CMIP5 ESMs
778 still overestimate the GPP when forced by observations. Specifically, Piao et al (2013) found that the
779 global terrestrial GPP averaged across 10 models forced by observed climate is 133 ± 15 PgC/y, with
780 ORCHIDEE and CLM4 having a mean global GPP of 151 ± 4 PgC/y over the period 1982-2008, and
781 TRIFFID showing a global GPP of about 140 PgC/y, consistent with our results from the IPSL-CM5
782 models, CESM1-BGC and the HadGEM2 models respectively. Since TRIFFID does not show any
783 relevant bias reduction between the online and offline version and although the bias in ORCHIDEE is
784 slightly lowered when forced by observed climate, we can exclude that the coupling generates this
785 large bias in GPP.

786 Looking at the interannual variability of GPP, in the tropics and in the Northern Hemisphere no model
787 captures the IAV of the observation based product, all models simulating larger GPP IAV than the one
788 given by the MTE-GPP. Several models show relatively good performances in the Southern
789 Hemisphere despite none of these models show a MVI value close to the good performance threshold
790 of 0.5 defined by Scherrer (2011). The poor performances found in the tropics and in the Northern
791 Hemisphere affect the global MVI and all the models show a MVI larger than 3.

792 However, it is worth seriously questioning the realism of the MTE-GPP product regarding its
793 magnitude of interannual variability and in particular in the tropics (Zhao and Running 2010). Most of
794 the MTE GPP sensitivity to temperature and precipitation is learned from the spatial variability of the
795 FLUXNET data, not its interannual variability. Also, there are virtually no FLUXNET sites in the

796 tropics to train the MTE product. The MTE tropical temporal variability is hence derived from the
797 spatial variability of temperate ecosystems. Hence, we prefer not to use the MTE-GPP IAV as a target
798 for CMIP5 models' evaluation.

799 All models predict a significant increase in vegetation productivity at global scale from 1986 to 2005,
800 although the magnitude of the trend from all the CMIP5 models (ranging from 0.2 PgC/y² to 0.66
801 PgC/y²) is significantly larger than MTE estimates (0.09 PgC/y²). Again, one could question the MTE-
802 GPP trend as atmospheric CO₂ fertilization was not explicitly accounted for in MTE-GPP framework.
803 Also, the MTE-GPP trend may be affected by changing satellite products of vegetation activity before
804 and after 1998. Hence, we prefer not to use the MTE-GPP trend as a target for CMIP5 models'
805 evaluation.

806 In the Southern Hemisphere almost all CMIP5 models do not show any relevant increase in vegetation
807 productivity, being the trend scattered around zero, while over the Northern Hemisphere and tropics
808 all the models exhibit a positive trend in GPP.

809 In **Figure 9** we compare the phase of the mean annual cycle of CMIP5 models with the GPP from the
810 MTE dataset. At global scale, all the CMIP5 models correctly reproduce the phase of the seasonal
811 cycle of GPP. In particular, over the globe and Northern Hemisphere the CMIP5 models capture the
812 GPP minimum during winter and fall and the summer GPP maximum related to the spring leaf out and
813 maximum growing season, while in the Southern Hemisphere, the models reproduce the phase of the
814 winter GPP minimum. Several problems are found in the tropical regions and only a few of the models
815 (BCC-CSM1, INMCM4, HadGEM2-ES, and NorESM1-ME) are able to accurately reproduce the
816 phase of the GPP seasonal cycle in this region. IPSL-CM5A-LR and IPSL-CM5A-MR models,
817 indeed, show in the Northern Hemisphere (and a global scale as well) a strong positive bias of GPP
818 during JJA. Since the evaluation of precipitation does not show a coincident wet bias, this suggest that
819 the land surface component of the IPSL models overestimates the GPP in summer, maybe because this
820 model does not have N-limitations or because the water stress is not strong enough during the peak
821 growing season.

822 The comparison of simulated LAI with a global data set derived from satellite data is presented in
823 **Figure 10**. However, before describing model's deficiencies we would highlight that there are several
824 limitations in the satellite observations that could explain the mismatch between the LAI data set and
825 CMIP5 results.

826 The remote sensing LAI products are estimates derived from top-of-the-atmosphere reflectances, and
827 use different sensors and algorithms (Los et al. 2000; Myneni et al. 2002). Therefore, the quality of
828 LAI retrievals is limited by the intrinsic characteristics of the sensor systems, the dynamic of the
829 signal received at the satellite level, and the physical properties of the target (Gibelin et al. 2006). For
830 instance, cloud cover hides the surface and produces discontinuities in time series. In addition, the
831 layers of a vegetation canopy cast shadow and LAI of lower layers near the ground may not be well
832 documented. This may yield a 30% underestimation in the case of clumped canopies (Roujean and
833 Lacaze 2002). This occurs mostly for dense forested areas and fully developed crops. On the other
834 hand, over semiarid ecosystems, soil brightness contaminates sufficiently the signal to restrict its
835 sensitive response to LAI increase. Similarly, high reflectance of snow may hamper an accurate LAI
836 retrieval at high latitudes at springtime (Gibelin et al. 2006).

837 Similarly to the temperature, precipitation, and GPP evaluation, the overall behaviour of CMIP5
838 models reproducing the LAI is analyzed by comparing the yearly mean simulated value with the
839 satellite-derived data set. In **Figure 10** we present, for each model, the mean LAI, the trend, and the
840 MVI computed in the period 1986-2005 for different sub-domains.

841 Looking at the mean global value, only INMCM4 and CanESM2 models capture the main features of
842 the global pattern, while all the remaining models overestimate the global LAI. Serious problems have
843 been found in BNU-ESM and GFDL models, all showing a global LAI above 2.4, while the reference
844 values is much lower (1.45). We found BNU-ESM having severe problems in reproducing the right
845 amplitude of LAI in the tropics (**Figure 10**) and the GFDL models completely unable to reproduce the
846 eastward gradient over Europe and Asia, as well as overestimating the LAI in North America (Anav et
847 al 2013). Consequently as shown in **Figure 10** in the Northern Hemisphere GFDL-ESM2G and
848 GFDL-ESM2M are far outliers and the global result is affected by this erroneous pattern. This

849 problem is likely due to the initialization of the vegetation during the spin up phase: in fact the GFDL
850 land model only allows coniferous trees to grow in cold climates, i.e. deciduous trees and grass do not
851 grow in these cold regions. As a result, coniferous trees are established in areas where there should be
852 tundra or cold deciduous trees (Anav et al 2013). Additionally, since all CMIP5 models were spun up
853 for many thousands of years, in case of GFDL models the coniferous vegetation eventually builds up
854 high LAI. It is also noteworthy that this positive bias in LAI does not significantly affect the GPP in
855 the Northern Hemisphere (**Figure 8**).

856 Over the Southern and Northern Hemispheres as well as in the tropical bounds we found a general
857 tendency by CMIP5 models to overestimate the LAI and only a few models are close to the
858 observation.

859 There are several reasons to explain the large overestimation of LAI by CMIP5 models. First, the high
860 GPP could lead to a surplus of biomass stored into the leaves. Also the missing parameterization of
861 ozone partially explains the LAI overestimation due to the GPP: specifically Wittig et al. (2009) and
862 Anav et al. (2011) found that ozone leads to a mean global LAI reduction of about 10-20% during the
863 historical period as compared with a simulation without elevated tropospheric ozone. Finally, as the
864 LAI dataset does not come out from true observations we cannot exclude that it is affected by a
865 significant bias. However, compared to other LAI datasets our reference data shows a good agreement:
866 in particular, considering the period 2000-2005, the mean global LAI of our dataset is 1.46, while
867 MODIS LAI (Yuan et al. 2011) shows a value of 1.49 and CYCLOPES LAI (Baret et al. 2007; Weiss
868 et al. 2007) has a global mean slightly lower at 1.27. However, this latter dataset has some low values
869 in dense canopies, especially evergreen broadleaf forests, which results in a lower value for the whole
870 Earth (Zhu et al. 2013).

871 Considering the interannual variability, none of models are close to the good performance threshold of
872 0.5, the MVI being systematically larger than 2 in all the domains. On the other side, the LAI trend is
873 well simulated by all models except BNU-ESM that largely overestimates the greening in the
874 Northern Hemisphere and tropics, as well as by GFDL-ESM2M and IPSL-CM5A-LR which show a

875 browning in Southern Hemisphere. Looking at global scale, most of the models do reproduce a slight
876 greening of the same magnitude than the observed data.

877 The comparison of LAI seasonal cycle is given in **Figure 11**. At the global scale and in the Northern
878 Hemisphere all the models (except GFDL) correctly reproduce the seasonal variability, namely
879 CMIP5 models reproduce the right timing of bud-burst and leaf-out, as well as the weak leaf coverage
880 during fall and winter. Some problems are found in the tropics and Southern Hemisphere, where some
881 models are anti-correlated to observations. Despite that the MIROC models show a good phase of LAI
882 compared to observations, they also show a strong positive bias during JJA in both the Hemispheres
883 and at the global scale.

884 The mean global soil carbon (\pm ensemble standard deviation) reported across all ESMs is 1502 ± 798
885 PgC, whereas the global soil carbon in the reference dataset is 1343 PgC (**Figure 12**). CESM1-BGC
886 has the lowest total at 512 PgC and MPI-ESM-MR the highest at 3091 PgC. Looking at the global
887 mean, most of the ESMs are clustered around the HWSO reference data (Todd-Brown et al 2012). It is
888 also interesting to note that both CESM1-BGC and NorESM1-ME models show the lowest totals and
889 these models both use CLM4 as land surface model (Table 2). This severe global underestimation is
890 due by the lower carbon soil simulated in the Northern Hemisphere. On the other side, MIROC and
891 MPI models strongly overestimate the soil carbon in all the sub-regions.

892 Similarly to the soil carbon results, the vegetation carbon evaluation shows that ESMs are also
893 clustered around the reference value (**Figure 12**). The multi-model mean of global vegetation carbon
894 (\pm ensemble standard deviation) reported across all ESMs is 522 ± 162 PgC, value close to the
895 reference data (556 PgC). At global scale MIROC and MPI models underestimate the reference value,
896 whereas BNU-ESM reported the highest total at 927 PgC, compared to the reference data. It is also
897 interesting to note that in the Northern Hemisphere GFDL-ESM2M shows the highest value; as
898 already observed for the LAI, the overestimation of vegetation carbon by GFDL-ESM2M is related to
899 the substitution of tundra with coniferous forest in the cold regions of North Hemisphere.

900 These results also show that CESM1-BGC and the NorESM1-ME models have a realistic vegetation
901 carbon, indicating that the large underestimation of their soil carbon content most probably comes

902 from an overestimation of the soil carbon decomposition rate. This might also contribute to explain the
903 low than average NBP simulated by these two models (**Figure 6**).

904 **3.3 CMIP5 ocean carbon**

905 The simulated evolution of ocean-atmosphere CO₂ flux is compared with GCP estimates in **Figure 13**.
906 Analogous to the land-atmosphere CO₂ flux (**Figure 5**), the CMIP5 models show increasing global
907 ocean CO₂ uptake, evident from the 1940's-2005. The CMIP5 ensemble air-sea flux increased from a
908 sink of 0.56 ± 0.13 PgC/y (with a mean yearly variability of ± 0.07 PgC/y) over the period 1901-1930 to
909 1.6 ± 0.2 PgC/y in the period 1960-2005 (with a mean yearly variability of ± 0.4 PgC/y). This multi-
910 model mean is slightly lower than GCP estimates, which show an ocean sink of 1.92 ± 0.3 PgC/y for
911 the period 1960-2005.

912 During El Niño events there is a suppression of the normally strong outgassing of CO₂ in the
913 Equatorial Pacific, and hence a larger than average global ocean sink. Keeling et al. (1995) show a
914 much smaller effect on the atmospheric CO₂ variability from the ocean than the biosphere, however
915 observational based estimates show contrasting results in terms of timing and magnitude of the
916 variations in net air-sea CO₂ fluxes (Francey et al. 1995; Rayner et al. 1999). The CMIP5 ensemble
917 mean shows a smaller variability in the ocean CO₂ uptake than in the biosphere (i.e. models agree on
918 the sign and magnitude of ocean CO₂ fluxes), as well as it has a lower year-to-year variability than
919 GCP estimates, partly because the interannual variability is somewhat smoothed out due to the model
920 averaging.

921 The mean ocean-atmosphere CO₂ fluxes for any individual model and in each ocean sub-domain are
922 shown in **Figure 14**. The global estimate of oceanic uptake of CO₂ from JMA inversion over the
923 period 1986-2005 is 1.73 ± 0.33 PgC/y, which is significantly lower than GCP estimate (2.19 ± 0.17
924 PgC/y) and Takahashi estimate (2.33 PgC/y), however similar to the estimates made in the IPCC 4th
925 assessment report (Denman et al. 2007).

926 At the global scale all CMIP5 models, except INMCM4, which overestimates the ocean sink with a
927 1986-2005 average of 2.65 ± 0.37 PgC/y, are in the range of observational uncertainty. In particular,
928 IPSL-CM5A-MR (2.22 ± 0.11 PgC/y), IPSL-CM5A-LR (2.17 ± 0.21 PgC/y), BCC-CSM1-M (2.09 ± 0.18

929 PgC/y), GFDL-ESM2M (2.04 ± 0.3 PgC/y), HadGEM2-ES (2.01 ± 0.12 PgC/y), HadGEM2-CC
930 (2.00 ± 0.19 PgC/y) and MPI-ESM-LR (1.96 ± 0.17 PgC/y) simulate values of both the global mean and
931 interannual variability close to the observational values, while CanESM2 (1.64 ± 0.25 PgC/y) shows the
932 weaker CO₂ sink, and NorESM1-ME (2.32 ± 0.15 PgC/y) well matches Takahashi estimate.

933 The fact that the CMIP5 models lack processes associated to the river loop of the carbon cycle, might
934 explain why the JMA inversions give a slightly lower CO₂ uptake than the models. Although carbon
935 fluxes from rivers are small compared to natural fluxes, they have the potential to contribute
936 substantially to the net air-sea fluxes of CO₂ (Aumont et al. 2001)

937 Using oceanic inversion methods it is possible to separately estimate the natural and anthropogenic
938 components of the air-sea CO₂ fluxes (Gruber et al. 2009). Here we consider the CMIP5 historical
939 simulations only, and therefore all regional patterns described are largely characteristic of natural air-
940 sea CO₂ exchanges and do not elucidate anthropogenic CO₂ uptake patterns.

941 At the regional scale the CMIP5 models demonstrate the expected pattern of outgassing of CO₂ in the
942 tropics and an uptake of CO₂ in the mid and high latitudes, with comparatively small fluxes in the high
943 latitudes. The exceptions are INMCM4, which shows an outgassing of CO₂ in the high latitude
944 Northern Hemisphere, and CanESM2, which shows an outgassing in the high latitude Southern
945 Hemisphere.

946 Inversion and Takahashi estimates show the mid-latitude Southern Ocean is a large sink of
947 atmospheric CO₂ (Takahashi et al. 2002). Its magnitude has been estimated over the period 1986-2005
948 to be about 0.73 ± 0.19 PgC/y from JMA inversion and 1.28 PgC/y from the Takahashi product
949 (**Figure 14**). All the CMIP5 models simulate a similar magnitude sink in this region except CanESM2,
950 which overestimates the sink (1.59 ± 0.05 PgC/y).

951 The mid latitude Northern Hemisphere Ocean is also a net sink for CO₂ (Denman et al. 2007), with a
952 magnitude of the order of 0.77 ± 0.08 PgC/y from JMA, and 1.15 PgC/y from Takahashi over the
953 period 1986-2005 (**Figure 14**). All the CMIP5 models, simulate a net sink, with values comparable to
954 the JMA inversion results.

955 The tropical oceans outgassing of CO₂ to the atmosphere has a mean flux of the order of -0.73 ± 0.14

956 PgC/y in the period 1986-2005 (**Figure 14**), estimated from JMA inversions, and a value of -1.25
957 PgC/y estimated from Takahashi. We find INMCM4 (1.10 ± 0.17 PgC/y) the only model unable to
958 reproduce the tropical source of carbon.

959 The seasonal air-sea CO₂ fluxes are compared against the JMA inversion estimates and the Takahashi
960 product in **Figure 15**. All the models except INMCM4 accurately reproduce the observational based
961 estimates in the mid latitudes. The model estimates for the tropics and high latitudes show greater
962 ambiguity. This is attributed to large uncertainties in modelled SST, MLD and ocean NPP in the high
963 latitude Southern Ocean, while in the equatorial region uncertainties can arise due to the lack of
964 mesoscale processes simulated by the models. At the global scale all of the models are out of phase
965 with the observations, and the MPI models as well as INMCM4 show a larger seasonal variation than
966 observations. In the MPI models this is a result of the poor performance in the high latitude Southern
967 Hemisphere where they strongly overestimate the CO₂ sink in austral summer and underestimate
968 during austral winter.

969 The air-sea CO₂ flux is driven in part by the biological pump. **Figure 16** shows individual model
970 performances at reproducing SeaWiFS based estimates of oceanic NPP in the reference ocean sub-
971 domains. The mean global NPP estimate based on the SeaWiFS data used here during the period
972 1998–2005 is 52.2 PgC/y. Using CZCS chlorophyll fields Longhurst et al. (1995) estimated global
973 NPP to be between 45-50 PgC/y, and Behrenfeld and Falkowski (1997) estimated a global rate of 43.5
974 PgC/y.

975 Globally quite a few models, except GFDLs, underestimate SeaWiFS NPP. Most of the models predict
976 a global average of ~30-40 PgC/y. This is reasonable when compared with published chlorophyll
977 based estimates, and considering the large uncertainty in the observational based datasets. The
978 significant under estimation of ocean NPP by most of the CMIP5 models could occur partly due to the
979 lack of explicit representation of coastal processes. The coarse resolution of ocean models does not
980 allow realistic simulation of the processes taking place in these shallow waters that are naturally
981 eutrophic because of riverine discharge, coastal upwelling and a high recycling rate of organic nutrient
982 matter.

983 On the other side, the strong positive bias found in the GFDL models for ocean NPP predominantly
984 stems from an overestimation of phytoplankton activity in the Eastern Equatorial Pacific. The GFDL
985 SST (**Figure 3**) and MLD do not show a larger deviation from observations than other models,
986 therefore we can exclude these two variables as the cause of the bias in this region.

987 Conversely, MPI models and CESM1-BGC have a global mean marine NPP most similar to that of the
988 SeaWiFS NPP, however in the case of MPI models this is a misleading result since the agreement
989 arises from a large overestimation of NPP in the Southern Hemisphere and an underestimation in the
990 Northern Hemisphere. Regionally all of the model biases take a different pattern to that of the global
991 scale. In the northern high latitudes we see that all of the models under estimate NPP whereas in the
992 Southern Hemisphere high latitudes all the models except CanESM2, IPSL-CM5A-LR and IPSL-
993 CM5A-MR overestimate NPP.

994 In all the CMIP5 models, and the SeaWiFS based estimates, zonally summed NPP is greatest in the
995 tropics. This is simply due to a larger ocean surface area, since on average NPP is lower in the tropics
996 and highest in Northern Hemisphere high latitudes.

997 Looking at the interannual variability the models in general are clustered around the reference data,
998 albeit in the two Northern Hemisphere sub-regions larger interannual variations are seen in the
999 reference data than in the CMIP5 models.

1000 In **Figure 17** we show the mean annual cycle of NPP as simulated by the CMIP5 models compared
1001 with the NPP estimated from SeaWiFS data. The largest seasonal variability in the SeaWiFS based
1002 NPP is seen the Northern Hemisphere high latitudes (49N–90N) with the peak in observations
1003 occurring in July. None of the CMIP5 models capture the magnitude or timing of this significant peak
1004 in productivity, with the majority of the models biased towards lower NPP and predicting the peak in
1005 productivity up to 2 months too early. Accurate model simulations of NPP are more difficult in this
1006 ocean sub-domain since it includes a mixture of several different regions and has a large proportion of
1007 coastal areas.

1008 Many of the models show the largest seasonal peak in marine NPP in the Southern Ocean (90S-44S),
1009 which is not supported by SeaWiFS estimates. This is due to a combination of model and

1010 observational errors. SeaWiFS observations generally underestimate surface chlorophyll in the
1011 Southern Ocean (Moore et al. 1999) and contain the largest uncertainty in the Southern Ocean due to
1012 under sampling and frequent deep chlorophyll maxima that cannot be observed on satellites. The
1013 models tend to overestimate NPP in the Southern Ocean due to too shallow simulated mixed layers in
1014 summer months and uncertainty in light parameterisations (Séférian et al. 2012). The models with the
1015 greatest overestimation of springtime NPP in the high latitude Southern Ocean are MPI models and
1016 NorESM1-ME with peak values of ~ 3 PgC/y compared to ~ 0.75 PgC/y for SeaWiFS based NPP
1017 estimates. All these models use the same biogeochemical model HAMOCC5 (Table 2), although with
1018 different parameterisations. It should also be noted that these latter models show the largest bias in the
1019 MLD seasonal cycle and this can contribute to the poor representation of temporal evolution of
1020 primary production.

1021

1022 4. MODEL RANKING

1023 Different diagnostics were used in section 3 to investigate the performances of CMIP5 Earth System
1024 Models during the 20th century at reproducing the mean value, IAV, trends and mean annual cycle for
1025 various different variables crucial to characterizing the global carbon cycle. These measures or
1026 “diagnostics” show that in general, the CMIP5 models simulate all the variables well when compared
1027 to the observations used here, although a few of the models do show notably poorer agreement than
1028 others and general problems exist for quite a few of the models. Specifically, all the variables in the
1029 tropical regions prove to be problematic for the models, reinforcing well-known deficiencies of
1030 models in reproducing the decadal variations in the ocean-atmosphere system, but also questioning the
1031 availability and quality of the data in the tropics.

1032 However, the diagnostics presented in sections 3 are not sufficient to clearly identify the best models;
1033 for such a purpose we need to define specific metrics that allow a quantitative model ranking. Metrics
1034 can be contrasted with ‘diagnostics’, which may take many forms (e.g., maps, time series, power
1035 spectra, errorbars, zonal means, etc.) and may often reveal more about the causes of model errors and

1036 the processes responsible for those errors. Following Gleckler et al. (2008) the metrics used in this
1037 paper are designed to quantify how much the model simulations differ from observations.

1038

1039 **4.1 Land carbon ranking**

1040 We used two different metrics to estimate the models' skills. In case of the mean annual cycle the skill
1041 score is computed following equation 3, and the model performances and ranking of the land variables
1042 are shown in **Figure 18**. Considering the mean annual cycle in addition to this skill score, in order to
1043 check how models reproduce only the phase of the observations, we also have computed the
1044 correlation coefficient (not shown). In fact, the correlation coefficient allows to identify models that
1045 are in phase with observations ($r>0$), and models that are out of phase ($r<0$). Correlation values close
1046 to 1 point out models that perfectly reproduce the seasonal phase of observations.

1047 Looking at the land surface temperature, at global scale and in Southern and Northern Hemisphere the
1048 best performances reproducing the mean annual cycle have been found for MPI models, CESM1-
1049 BGC, and NorESM1-ME, whilst in the tropics BNU-ESM and BCC-CSM1 have the highest scores.
1050 All the models have a correlation coefficient greater than 0.9 at global scale and in the 2 Hemispheres,
1051 while in the tropics it ranges between 0.6 and 0.8.

1052 The precipitation shows a similar pattern, with MPI models having the best performances in all the
1053 sub-domains, except the Southern Hemisphere, where BCC-CSM1 and IPSL-CM5A-MR have the
1054 best scores (**Figure 18**).

1055 Unlike seasonal variation in temperature, which at large scales is strongly determined by the insolation
1056 pattern, seasonal precipitation variations are strongly influenced by vertical movement of air due to
1057 atmospheric instabilities of various kinds and by the flow of air over orographic features. For models
1058 to simulate accurately the seasonally varying pattern of precipitation, they must correctly simulate a
1059 number of processes (e.g. evapotranspiration, condensation, transport) that are difficult to evaluate at a
1060 global scale (Randall et al. 2007). The precipitation exhibits a correlation never exceeding a value of
1061 0.8 in all the sub-domains and for all the models, with the lowest value (0.4) found in the Northern
1062 Hemisphere for the BNU-ESM model (not shown).

1063 Looking at the GPP, at global scale CESM1-BGC shows the best performances, albeit its GPP
1064 decrease during fall does not match the phase of observation (**Figure 9**). In fact, for a given seasonal
1065 skill score it is impossible to determine how much of the error is due to a difference in structure and
1066 phase and how much is simply due to a difference in the amplitude of the variations. Also in the
1067 Southern Hemisphere and Tropics CESM1-BGC has the highest scores for the GPP, while in the
1068 Northern Hemisphere the best results are found in BCC-CSM1-M.

1069 Looking at the phase of GPP there is a relevant agreement with the reference data, the correlation
1070 being systematically positive. This is particularly evident in the Northern Hemisphere where all the
1071 models have a correlation above 0.8 (not shown). Contrarily, in the Tropics there is a poorer
1072 agreement and some models (e.g. CanESM2, and IPSL-CM5B-LR) show a correlation around 0.4 (not
1073 shown).

1074 The same considerations drawn for the GPP are also valid for the LAI, with CanESM2 showing the
1075 best skills at global scale, although it seems to be 2 months out of phase with respect to observations
1076 during the peak season (**Figure 11**). In addition, all the models show a correlation greater than 0.6
1077 both at global scale and in the Northern Hemisphere, while in the Tropics we found the poorest results
1078 with some models (BNU-ESM, BCC-CSM1, and BCC-CSM1-M) having a correlation of about 0.2.

1079 Considering the global NBP, consistent with results of **Figure 7**, MPI-ESM-LR and MIROC-ESM
1080 have the best performances, whilst CanESM2, BNU-ESM, MPI-ESM-MR, and CESM1-BGC show
1081 the poorest scores. Contrarily, in the Southern Hemisphere CESM1-BGC and CanESM2 have the
1082 highest scores, while in the Tropics the 2 Hadley models show the best results.

1083 Several models show a negative correlation compared to inversion estimates in the Tropical region
1084 and in the Southern Hemisphere, while in the Northern Hemisphere quite a few models have a
1085 correlation above 0.9 (not shown).

1086 The second skill score is computed following equation 5, and it essentially allows to asses the skills of
1087 models in reproducing the mean state of the system with its IAV. **Figure 19** shows an absolute
1088 measure of ESMs skill in simulating the observed PDFs of the variables under examination for the

1089 land carbon. There is no obvious way to define ‘good’ or ‘bad’ performance, or indeed, ‘adequate’
1090 from the skill score, but identifying those models with a relatively better skill is straightforward.

1091 According to the skill threshold defined in Section 2.3, looking at global temperature, only few models
1092 are close to the threshold value of 0.68. Consistent with **Figure 1**, the best performances have been
1093 found in the MPI models, while the poorest skills are found in INMCM4. The same considerations are
1094 valid also for the Southern and Northern Hemisphere. Looking at the Tropics, consistent with **Figure**
1095 **1**, INMCM4 shows a very poor skill, related to the large cold bias previously described. Unlike **Figure**
1096 **1**, the skill score shows that BCC-CSM1 is not the best model in the Tropical region. This results
1097 however is not surprising, the agreement in the mean tropical temperature shown in **Figure 1** could
1098 arise from a compensation between overestimation in some regions of the tropics and underestimation
1099 in other regions of the tropics, while the skill score does not lead to the same optimistic picture. In fact
1100 the overlapping of the PDFs allows equal weighting of all the points with a relevantly poor mismatch
1101 to the mean value. This suggests that the models we found using the previous diagnostics that have a
1102 bias in the mean values still score badly, but models with a good agreement with the mean do not
1103 necessarily score well.

1104 The precipitation shows the same picture of temperature with a general good agreement in the
1105 Southern and Northern Hemisphere and poorer skills in the Tropical region, likely related to the poor
1106 skill reproducing the IAV (**Figure 2**). Relevant skills are found in the Southern Hemisphere for the
1107 Hadley models, where the overall score is greater than 0.7.

1108 Contrarily, very poor skills are found for GPP and LAI, both a global scale and in all the sub-domains.
1109 In **Figure 8** and **Figure 10**, respectively, we show how almost all CMIP5 models overestimate these
1110 two variables, possibly because these models do not have nutrient limitations and any ozone impact on
1111 carbon assimilation. Consequently none of models achieve a relevant score, and for quite a few
1112 models the skill score is less than 0.3. As pointed out before, we cannot exclude risks of significant
1113 bias in the GPP and LAI evaluation datasets as these are not true observations.

1114 Unlike other variables related to the land carbon cycle, good scores are found for the NBP. As already
1115 shown in **Figure 6** most of the models match both the mean value and the IAV, therefore, except

1116 GFDL-ESM2M that significantly overestimates the IAV, at global scale we found a score above 0.5
1117 for all the models, with the best result found in IPSL-CM5A-LR that simulates more than 2σ of the
1118 reference PDF. Conversely, none of the models are able to simulate the observed PDF for the NBP in
1119 the Northern Hemisphere, and this is consistent with the negative bias already shown in **Figure 6**.
1120 However it should also be noted that the NBP PDFs are build from regional averages, while other
1121 variables are based on the comparisons of skills at each grid point, then averaged over large sub-
1122 regions; this explains why the NBP skill scores are consistently better than the scores of the other
1123 variables.
1124 In case of soil and vegetation carbon the skill scores reported in **Figure 19** are not based on the PDF
1125 overlapping, but they have been computed as a relative bias. Results in general agree with finding of
1126 **Figure 12**, namely the best results for the soil carbon are found in BCC models, while MIROC and
1127 MPI models show the poorest performances due to the large positive bias. Considering the vegetation
1128 carbon, INMCM4 has the best skill score, while BNU-ESM and GFDL-ESM2M show the poorest
1129 performances. The only exception is the Tropical region, where the best model reproducing the
1130 vegetation carbon is MPI-ESM-MR, with BNU-ESM still showing the poorest results.

1131

1132 **4.2 Ocean carbon ranking**

1133 The skills of CMIP5 models at reproducing the mean annual cycle of relevant variables for the ocean
1134 carbon cycle are shown in **Figure 20**.

1135 Considering the SST, there is a large variability in the skill score of models between the different sub-
1136 domains; in general, the best results are found for CanESM2, CESM1-BGC and MPI models, while
1137 BNU-ESM and GFDL models show the poorest skills. Consistent with results of **Figure 4**, the Hadley
1138 models show the best performances at reproducing the mean annual cycle of the MLD, with the MPI
1139 models having the poorest skill scores (**Figure 20**).

1140 We also have found excellent performances of CMIP5 models in reproducing the only phase of the
1141 mean annual cycle of physical variables (i.e. SST and MLD), with correlations above 0.85 for all the
1142 models and sub-domains (not shown).

1143 As discussed previously, the poor performances of the MPI models in reproducing the seasonal
1144 evolution of the MLD also affect the overall skill score of the ocean-atmosphere CO₂ fluxes; in
1145 particular, we found the MPI models having the worst performances at global scale, as a consequence
1146 of the poor results found in the extreme Southern Ocean, whilst in the tropical bound and in the 2
1147 Northern Hemisphere sub-domains the MPI models show a relevant skill in reproducing the CO₂
1148 fluxes (**Figure 20**).

1149 Nevertheless, severe problems exist in reproducing the only phase of global seasonal cycle of CO₂
1150 fluxes, where several models are anti-correlated with observations. The poor performances in the
1151 global values are caused by the inability of models in simulating the correct seasonal cycle in the
1152 tropical sub-domain as well as in the high-latitude Southern and Northern Oceans. Conversely, in the
1153 mid-latitude Southern and Northern Oceans, except INMCM4, all the models are positively correlated
1154 with JMA inversions and the correlation coefficient is generally higher than 0.7 (not shown).

1155 Considering the ocean primary production the best performances have been found for CESM1-BGC
1156 and IPSL models, while the worst results are found for the MPI models and NorESM1-ME. It should
1157 be noted that all these models use the same ocean biogeochemical model (**Table 2**). Conversely, with
1158 the only exception of CanESM2, all the models show a relevant correlation with SeaWIFS data in all
1159 the sub-domains (not shown).

1160 Considering the PDF-based skill score, consistent with land surface temperature and precipitation
1161 results, the SST skill score for several models is above the threshold of 1σ , with some models having a
1162 score above 0.8 (**Figure 21**). This is particularly evident in the temperate Southern and Northern
1163 Oceans as well as in the tropics. Although the models exhibit relevant skills at reproducing the SST in
1164 some basins, in the Northern and Southern Ocean none of the model is able to reproduce at least 1σ of
1165 the reference dataset.

1166 Since the observed MLD is a climatology, the ranking is tricky and the values shown in **Figure 21** do
1167 not represent the skill score defined in section 2. Therefore, for this variable only the ranking is based
1168 on the bias rather than on the overlapping of the PDFs. Globally, we found HadGEM2-ES and
1169 HadGEM2-CC the best models at reproducing the MLD, and NorESM1-ME is found to have the

largest bias in all the sub-domains, except in the Southern Ocean where MPI models show the worst agreement to the observations.

The ocean-atmosphere CO₂ flux shows an acceptable skill score for most of the models; however it should be noted that likewise the NBP also the ocean-atmosphere CO₂ flux PDFs are based on regional comparisons. Globally several models have a score higher than 0.7, and only IPSL-CM5A-MR, INMCM4, and NorESM1-ME show poor performances. As already seen in **Figure 14**, the poor skill found in INMCM4 at global scale is due to the poor performances of this model to correctly reproduce the fluxes in the tropical regions (18S-18N) and in the Northern Hemisphere. Therefore, consistent with results of **Figure 14** INMCM4 shows the poorest performances in these sub-domains. Conversely, INMCM4 has the best performances in the temperate Southern Hemisphere where it is able to reproduce almost 2σ of the observed PDF.

As we previously discussed, the simulated global ocean primary production is affected by a negative (or positive for GFDL models and MPI-ESM-LR) bias, consequently the skill score does not exceed a value of 0.4. The same considerations are also valid for the other sub-domains, and the only relevant performances are found in the Southern Hemisphere where several models show a skill score above 0.6. In previous sections we speculated that the ocean primary production underestimation by models is likely due to a coarse resolution of the ocean grids that does not allow to properly simulate the dynamics in the shallow waters; the good performances found in the Southern Ocean would support this assumption.

5. CONCLUSION

In this study the evaluation of the CMIP5 ESMs focused on the ability of the models to reproduce the seasonal cycle, the mean state with its interannual variability, and trends of land and ocean variables related to the carbon cycle. This task allows the identification of the strengths and weaknesses of individual coupled carbon-climate models as well as identification of systematic biases of the models. We have highlighted that the evaluation is partly subjective due to the choice of the variables. In this paper we focused only on the validation of carbon fluxes and main variables affecting the fluxes,

1197 however many more data (e.g. DIC, pCO₂, chlorophyll concentration) could be used to evaluate the
1198 ESMs

1199 Multi-model databases offer both scientific opportunities and challenges. One challenge is to
1200 determine whether the information from each individual model in the database is equally reliable, and
1201 should be given equal “weight” in a multi-model detection and attribution study (Santer et al. 2009).
1202 We used a skill score based on the overlapping of PDFs, and the centered RMS error for the model
1203 ranking. In general we found that the ranking is sensitive to the large latitudinal bounds and the
1204 variable under examination, i.e. models that poorly perform in some sub-domains could have relevant
1205 skills in other sub-domains.

1206 Although both the skill scores identify some models as having the best global performances, several
1207 criticisms must be noted.

1208 Firstly, the evaluation presented here is partly subjective due to the choice of the variables, and these
1209 are sensitive to the choice of reference data. In other words, the best models for our reference variables
1210 might have poor performances reproducing other variables of interest. This suggests, therefore, that
1211 users of the CMIP5 models need to assess each model independently for their regions of interest,
1212 against those variables that are important for their specific subject of research.

1213 Secondly, we did not account for the uncertainty in the reference data; in general for the physical
1214 variables it is expected that errors remain much smaller than the errors in the models, but in case of
1215 biological variables this is not true. However, we believe that considering the uncertainties in the
1216 observed datasets does not significantly change our model ranking, except for land GPP interannual
1217 variability and ocean NPP that might suffer large uncertainty in the mean value. For instance, Gregg
1218 and Casey (2004) report an uncertainty in the ocean primary production of about 30%, and
1219 considering this uncertainty the model ranking could significantly differ from our results.

1220 In addition the observations used in this study do not always come from direct measurements, and in
1221 the case of biological variables some models or algorithms have been used to retrieve the values used
1222 in this study. This suggests that additional uncertainty should be added to the reference data, or in
1223 some case (e.g GPP trend) the data should simply not be used in the model evaluation.

1224 Thirdly, the aggregation of regions can give distorted results. The choice of regions in itself affects the
1225 outcome of the regional metrics calculated, but also affects the global result through neutralising or
1226 enhancing regional outcomes when Northern and Southern hemispheres are combined.

1227 In addition, the skill scores could be sensitive to the spatial scale. Considering 22 coupled ocean-
1228 atmosphere general circulation models (OAGCMs), Gleckler et al (2008) have evaluated the impact of
1229 alternative reference data set, other available realizations, and different resolution grids to the final
1230 ranking, finding that ‘*in some cases these variations on our analysis choices lead to small differences*
1231 *in a model’s relative ranking, whereas in others the differences can be quite large. Rarely, however,*
1232 *would the model rank position change by more than 5 or 6”.*

1233 In order to cross check the sensitivity of the skill score to resolution, we regrided the surface
1234 temperature to 4 different resolutions (i.e. 0.5, 1, 1.5, and 2 degrees), finding that the resolution does
1235 not significantly affect the ranking. Best models and poor models are always the same for all the
1236 resolutions, and in general the model rank position does not change by more than 4 (not shown).

1237 Fourthly, considering the model ranking, one could argue that choosing the highest score would
1238 favour models with more than one realization. However we also produced alternative rankings using
1239 either only the first realization from all the models, or computing the mean skill score averaged over
1240 the available realizations. We found no relevant differences in the model ranking between the three
1241 different methods (not shown).

1242 Lastly, a PDF-derived skill-score is a useful means of evaluating models since skill in this measure
1243 implies an ability to simulate a range of behaviour (e.g., mean, IAV, trend), however, we do not argue
1244 that the skill metrics used in this paper are definitive nor do these identify models that are more
1245 predictive. We believe that it is a substantial advance on the assessment of climate and carbon cycle
1246 models skill, but as with all statistics, must be interpreted with a degree of caution so as to avoid
1247 misleading assertions.

1248

1249

1250

1251 **Acknowledgements**

1252 We acknowledge the World Climate Research Programme's Working Group on Coupled Modelling,
1253 which is responsible for CMIP, and we thank the climate modeling groups (listed in Table 1 of this
1254 paper) for producing and making available their model output. For CMIP the U.S. Department of
1255 Energy's Program for Climate Model Diagnosis and Intercomparison provides coordinating support
1256 and led development of software infrastructure in partnership with the Global Organization for Earth
1257 System Science Portals.

1258 We also thank G. Maze for providing blended monthly time series of ocean NPP
1259 (http://data.guillaumemaze.org/ocean_productivity), the three anonymous reviewers and Dr. Anand
1260 Gnanadesikan for their helpful comments. A special thank to Tomohiro Hajima, Dr. Hideki Okajima,
1261 and Spencer Liddicoat for providing additional datasets not available on PDMDI server, to Philippe
1262 Peylin for sharing TRANSCOM3 inversion results, and Markus Reichstein for the several
1263 clarifications. This work was supported by the European Commission's 7th Framework Programme
1264 under grant agreement 238366 (GREENCYCLESII) and 282672 (EMBRACE), while Dr. Jones was
1265 supported by the Joint DECC/Defra Met Office Hadley Centre Climate Programme (GA01101).

1266 **REFERENCES**

- 1267 Adler, R.F., and Coauthors, 2003: The Version-2 Global Precipitation Climatology Project (GPCP)
1268 monthly precipitation analysis (1979-present). *J. Hydrometeor.*, **4**, 1147-1167.
1269
- 1270 Allan, R. P., and B. J. Soden, 2007: Large discrepancy between observed and simulated precipitation
1271 trends in the ascending and descending branches of the tropical circulation. *Geophys. Res. Lett.*, **34**,
1272 L18705, doi:10.1029/2007GL031460.
1273
- 1274 Anav, A., L. Menut, D. Khvorostyanov, and N. Viovy, 2011: Impact of tropospheric ozone on the
1275 Euro-Mediterranean vegetation. *Global Change Biol.*, **17**, 2342–2359.
- 1276 Anav, A., G. Murray-Tortarolo, P. Friedlingstein, S. Sitch, S. Piao, Z. Zhu, 2013: Evaluation of
1277 DGVMs in Reproducing Satellite Derived LAI over Northern Hemisphere. Part II: Earth System
1278 Models. *Remote Sens.*, in prep.
- 1279 Arora, V. K., J. F. Scinocca, G. J. Boer, J. R. Christian, K. L. Denman, G. M. Flato, V. V. Kharin, W.
1280 G. Lee, and W. J. Merryfield, 2011: Carbon emission limits required to satisfy future representative
1281 concentration pathways of greenhouse gases. *Geophys. Res. Lett.*, **38**, L05805,
1282 doi:10.1029/2010GL046270.
1283
- 1284 Aumont, O., J. C. Orr, P. Monfray, W. Ludwig, P. Amiotte-Suchet, J.-L. Probst, 2001: Riverine-driven
1285 interhemispheric transport of carbon. *Global Biogeochem. Cycles*, **15**, 393–405.
1286
- 1287 Baker, D. F., and Coauthors, 2006: Transcom 3 inversion intercomparison: Impact of transport model
1288 errors on the interannual variability of regional CO₂ fluxes, 1988–2003. *Global Biogeochem. Cycles*,
1289 **20**, GB1002, doi:10.1029/2004GB002439.
1290
- 1291 Baker, I. T., L. Prihodko, A. S. Denning, M. Goulden, S. Miller, and H. R. da Rocha, 2008: Seasonal
1292 drought stress in the Amazon: Reconciling models and observations. *J. Geophys. Res.*, **113**, G00B01,
1293 doi:10.1029/2007JG000644.
1294
- 1295 Baret, F., and Coauthors, 2007: LAI, fAPAR and fCover CYCLOPES global products derived from
1296 VEGETATION: Part 1: Principles of the algorithm. *Remote Sens. Environ.*, **110**, 275-286.
1297
- 1298 Beer, C., and Coauthors, 2010: Terrestrial gross carbon dioxide uptake: Global distribution and
1299 covariation with climate. *Science*, **329**, 834–838.
1300
- 1301 Behrenfeld, M. J., and P. G. Falkowski, 1997: Photosynthetic rates derived from satellite-based
1302 chlorophyll concentration. *Limnol. Oceanogr.*, **42**, 1–20.
1303
- 1304 Cadule, P., P. Friedlingstein, L. Bopp, S. Sitch, C. D. Jones, P. Ciais, S. L. Piao, and P. Peylin, 2010:
1305 Benchmarking coupled climate-carbon models against long-term atmospheric CO₂ measurements.
1306 *Global Biogeochem. Cycles*, **24**, GB2016, doi:10.1029/2009GB003556.
1307
- 1308 Chen, W., Z. Jiang, and L. Li, 2011: Probabilistic projections of climate change over China under the
1309 SRES A1B scenario using 28 AOGCMs. *J. Climate*, **24**, 4741-4756.
1310
- 1311 Chou, C., and C.-W. Lan, 2012: Changes in the annual range of precipitation under global warming. *J.*
1312 *Climate*, **25**, 222-235.
1313

1314 Chylek, P., Li, J., Dubey, M. K., Wang, M., and Lesins, G., 2011: Observed and model simulated 20th
1315 century Arctic temperature variability: Canadian Earth System Model CanESM2. *Atmos. Chem. Phys.*
1316 *Discuss.*, **11**, 22893-22907.

1317

1318 Collins, W., and Coauthors, 2006: The community climate system model version 3 (CCSM3). *J.*
1319 *Climate*, **19**, 2122–2143.

1320

1321 Collins, W., and Coauthors, 2011: Development and evaluation of an earth-system model-HadGEM2.
1322 *Geosci. Model Dev.*, **4**, 1051–1075.

1323

1324 de Boyer Montégut, C., G. Madec, A. S. Fischer, A. Lazar, and D. Iudicone, 2004: Mixed layer depth
1325 over the global ocean: an examination of profile data and a profile-based climatology. *J. Geophys.*
1326 *Res.*, **109**, C12003, doi:10.1029/2004JC002378.

1327

1328 Delworth, T. L., and Coauthors, 2006: GFDL’s CM2 global coupled climate models. Part I:
1329 formulation and simulation characteristics. *J. Climate*, **19**, 643–674.

1330

1331 Denman, K. L., and Coauthors, 2007: Couplings between changes in the climate system and
1332 biogeochemistry. *Climate Change 2007: The Physical Science Basis*, S. Solomon et al., Eds.,
1333 Cambridge University Press, 589–662.

1334

1335 Dezi, S., B. E. Medlyn, G. Tonon, and F. Magnani, 2010: The effect of nitrogen deposition on forest
1336 carbon sequestration: a model-based analysis. *Global Change Biol.*, **16**, 1470–1486.

1337

1338 Dima, M., and G. Lohmann, 2010: Evidence for two distinct modes of large-scale ocean circulation
1339 changes over the last century. *J. Climate*, **23**, 5–16.

1340

1341 Dufresne, J.-L., and Coauthors, 2012: Climate change projections using the IPSL-CM5 Earth System
1342 Model: from CMIP3 to CMIP5. *Clim. Dyn.*, under review.

1343

1344 Dunne, J. P., and Coauthors, 2012: GFDL’s ESM2 Global Coupled Climate–Carbon Earth System
1345 Models. Part I: Physical Formulation and Baseline Simulation Characteristics. *J. Climate*, **25**, 6646–
1346 6665.

1347

1348 Engelen, R. J., A. S. Denning, and K. R. Gurney, 2002: On error estimation in atmospheric CO₂
1349 inversions. *J. Geophys. Res.*, **107**, 4635, doi:10.1029/2002JD002195.

1350

1351 Errasti, I., A. Ezcurra, J. Sáenz, and G. Ibarra-Berastegi, 2011: Validation of IPCC AR4 models over
1352 the Iberian Peninsula. *Theor. Appl. Climatol.*, **103**, 61–79.

1353

1354 FAO/IIASA/ISRIC/ISSCAS/JRC, 2012: Harmonized World Soil Database (version 1.2). FAO, Rome,
1355 Italy and IIASA, Laxenburg, Austria.

1356

1357 Francey, R. J., P. P. Tans, C. E. Allison, I. G. Enting, J. W. C. White, and M. Trolier, 1995: Changes
1358 in oceanic and terrestrial carbon uptake since 1982. *Nature*, **373**, 326-330.

1359

1360 Gibbs, H. K.: 2006: Olson’s Major World Ecosystem Complexes Ranked by Carbon in Live
1361 Vegetation: An Updated Database Using the GLC2000 Land Cover Product (available at
1362 <http://cdiac.ornl.gov/epubs/ndp/ndp017/ndp017b.html>).

1363

1364 Gibelin, A.-L., J.-C. Calvet, J.-L. Roujean, L. Jarlan, and S. O. Los, 2006: Ability of the land surface
1365 model ISBA-A-gs to simulate leaf area index at the global scale: Comparison with satellites products.
1366 *J. Geophys. Res.*, **111**, D18102, doi:10.1029/2005JD006691.

1367 Gillett, N. P., P. A. Stott, and B. D. Santer, 2008: Attribution of cyclogenesis region sea surface
1368 temperature change to anthropogenic influence. *Geophys. Res. Lett.*, **35**, L09707, doi:
1369 10.1029/2008GL033670.

1370
1371 GLC2000. Global Land Cover 2000 database. European Commission, Joint Research Centre, 2003
1372 (available at <http://bioval.jrc.ec.europa.eu/products/glc2000/glc2000.php>).

1373
1374 Gleckler, P. J., K. E. Taylor, and C. Doutriaux, 2008: Performance metrics for climate models, *J.*
1375 *Geophys. Res.*, **113**, D06104, doi:10.1029/2007JD008972.

1376
1377 Goll, D. S., V. Brovkin, B. R. Parida, C. H. Reick, J. Kattge, P. B. Reich, P. M. van Bodegom, and Ü.
1378 Niinemets, 2012: Nutrient limitation reduces land carbon uptake in simulations with a model of
1379 combined carbon, nitrogen and phosphorus cycling. *Biogeosciences Discuss.*, **9**, 3173–3232.

1380
1381 Gregg W. W., and N. W. Casey, 2004: Global and regional evaluation of the SeaWiFS chlorophyll
1382 data set. *Remote Sens Environ.*, **93**, 463–479.

1383
1384 Gruber, N., and Coauthors, 2009: Oceanic sources, sinks, and transport of atmospheric CO₂. *Global*
1385 *Biogeochem. Cycles*, **23**, GB1005, doi:10.1029/2008GB003349.

1386
1387 Gurney, K. R., and Coauthors, 2002: Towards robust regional estimates of CO₂ sources and sinks
1388 using atmospheric transport models. *Nature* **415**, 626–630.

1389
1390 Gurney, K. R., and Coauthors, 2003: Transcom 3 CO₂ Inversion Intercomparison: 1. Annual mean
1391 control results and sensitivity to transport and prior flux information. *Tellus*, **55B**, 555–579.

1392
1393 Gurney, K. R., and Coauthors, 2004: Transcom 3 inversion intercomparison: model mean results for
1394 the estimation of seasonal carbon sources and sinks. *Global Biogeochem. Cycles*, **18**, GB1010,
1395 doi:10.1029/2003GB002111.

1396
1397 Gurney, K. R., D. Baker, P. Rayner, and S. Denning, 2008: Interannual variations in continental-scale
1398 net carbon exchange and sensitivity to observing networks estimated from atmospheric CO₂
1399 inversions for the period 1980 to 2005. *Global Biogeochem. Cycles*, **22**, GB3025,
1400 doi:10.1029/2007GB003082.

1401
1402 Hawkins, E., and R. Sutton, 2009: The potential to narrow uncertainty in regional climate predictions.
1403 *Bull. Amer. Meteor. Soc.*, **90**, 1095–1107.

1404
1405 Houghton, R. A., 2000: Interannual variability in the global carbon cycle. *J. Geophys. Res.*, **105**,
1406 20121–20130.

1407
1408 Kaminski, T., P. J. Rayner, M. Heimann, and I. G. Enting, 2001: On aggregation errors in atmospheric
1409 transport inversions. *J. Geophys. Res.*, **106**, 4703–4715.

1410
1411 Keeling, C.D., T. P. Whorf, M. Wahlen, and J. van der Plicht, 1995: Interannual extremes in the rate
1412 of rise of atmospheric carbon dioxide since 1980. *Nature*, **375**, 666–670.

1413
1414 Knutti, R., R. Furrer, C. Tebaldi, J. Cermak, and G. Meehl, 2010: Challenges in Combining
1415 Projections from Multiple Climate Models. *J. Climate*, **23**, 2739–2758.

1416
1417 Koffi, E. N., P. J. Rayner, M. Scholze, and C. Beer, 2012: Atmospheric constraints on gross primary
1418 productivity and net ecosystem productivity: Results from a carbon-cycle data assimilation system.
1419 *Global Biogeochem. Cycles*, **26**, GB1024, doi:10.1029/2010GB003900.

1420 Jacob D., A. Elizalde, A. Haensler, S. Hagemann, P. Kumar, R. Podzun, D. Rechid, A. R. Remedio, F.
1421 Saeed, K. Sieck, C. Teichmann, C. Wilhelm, 2012: Assessing the Transferability of the Regional
1422 Climate Model REMO to Different COordinated Regional Climate Downscaling EXperiment
1423 (CORDEX) Regions. *Atmosphere*, **3**, 181-199.
1424
1425 Jobbagy, E. G., and R. B. Jackson, 2000: The vertical distribution of soil organic carbon and its
1426 relation to climate and vegetation. *Ecological Applications*, **10**, 423–436.
1427
1428 John, V. O., R. P. Allan, and B. J. Soden, 2009: How robust are observed and simulated precipitation
1429 responses to tropical ocean warming? *Geophys. Res. Lett.*, **36**, L14702, doi:10.1029/2009GL038276.
1430
1431 Johns, T. C., and Coauthors, 2006: The new Hadley centre climate model (HadGEM1): evaluation of
1432 coupled simulations. *J. Climate*, **19**, 1327–1353.
1433
1434 Johnson, F., S. Westra, A. Sharma, and A. J. Pitman, 2011: An Assessment of GCM Skill in
1435 Simulating Persistence across Multiple Time Scales. *J. Climate*, **24**, 3609–3623.
1436
1437 Jones, C. D., and Coauthors, 2011: The HadGEM2-ES implementation of CMIP5 centennial
1438 simulations. *Geosci. Model Dev.*, **4**, 543-570
1439
1440 Jung, M., M. Reichstein, and A. Bondeau, 2009: Towards global empirical upscaling of FLUXNET
1441 eddy covariance observations: Validation of a model tree ensemble approach using a biosphere model.
1442 *Biogeosciences*, **6**, 2001–2013.
1443
1444 Jung, M., and Coauthors, 2011: Global patterns of land-atmosphere fluxes of carbon dioxide, latent
1445 heat, and sensible heat derived from eddy covariance, satellite, and meteorological observations. *J.*
1446 *Geophys. Res.*, **116**, G00J07, doi:10.1029/2010JG001566.
1447
1448 Lasslop, G., M. Reichstein, D. Papale, A. Richardson, A. Arneth, A. Barr, P. Stoy, and G. Wohlfahrt,
1449 2009: Separation of net ecosystem exchange into assimilation and respiration using a light response
1450 curve approach: Critical issues and global evaluation. *Global Change Biol.*, **16**, 187–208.
1451
1452 Le Quere, C., and Coauthors, 2009: Trends in the sources and sinks of carbon dioxide. *Nat. Geosci.*, **2**,
1453 831–836.
1454
1455 Liepert, B. G., and M. Previdi, 2009: Do Models and Observations Disagree on the Rainfall Response
1456 to Global Warming? *J. Climate*, **22**, 3156–3166.
1457
1458 Lin, J. L., 2007: Interdecadal variability of ENSO in 21 IPCC AR4 coupled GCMs. *Geophys. Res.*
1459 *Lett.*, **34**, L12702, doi:10.1029/2006GL028937.
1460
1461 Lin, J. L., K. M. Weickmann, G. N. Kiladis, B. E. Mapes, S. D. Schubert, M. J. Suarez, J. T.
1462 Bacmeister, and M. I. Lee, 2008: Subseasonal variability associated with Asian Summer Monsoon
1463 simulated by 14 IPCC AR4 coupled GCMs. *J. Climate*, **21**, 4541–4567.
1464
1465 Los, S. O., P. J. Sellers, G. J. Collatz, R. S. DeFries, C. J. Tucker, N. H. Pollack, D. A. Dazlich, and L.
1466 Bounoua, 2000: A global 9-year biophysical land surface dataset from NOAA AVHRR data. *J.*
1467 *Hydrometeor.*, **1**, 183–199.
1468
1469 Lucarini, V., S. Calmanti, A. Della Aquila, P. M. Ruti, and A. Speranza, 2007: Intercomparison of the
1470 northern hemisphere winter mid-latitude atmospheric variability of the IPCC models. *Climate Dyn.*,
1471 **28**, 829-848.
1472

1473 Mao, J., P. Thornton, X. Shi, M. Zhao, and W. Post, 2012: Remote sensing evaluation of CLM4 GPP
1474 for the period 2000 to 2009. *J. Climate*, **25**, 5327–5342.
1475

1476 Marti, O., and Coauthors, 2010: Key features of the IPSL ocean atmosphere model and its sensitivity
1477 to atmospheric resolution. *Climate Dyn.*, **34**, 1–26.
1478

1479 Martin, G. M., and Coauthors, 2011: The HadGEM2 family of Met Office Unified Model climate
1480 configurations. *Geosci. Model Dev.*, **4**, 723–757.
1481

1482 Martinez, E., D. Antoine, F. D’Ortenzio, and B. Gentili, 2009: Climate-driven basin-scale decadal
1483 oscillations of oceanic phytoplankton. *Science*, **326**, 1253–1256.
1484

1485 Maxino, C. C., B. J. McAvaney, A. J. Pitman, and S. E. Perkins, 2008: Ranking the AR4 climate
1486 models over the Murray Darling Basin using simulated maximum temperature, minimum temperature
1487 and precipitation. *Int. J. Climatol.*, **28**, 1097–1112.
1488

1489 Meehl, G. A., and Coauthors, 2007: Global climate projections. *Climate Change 2007: The Physical
1490 Science Basis*, S. Solomon, Eds., Cambridge University Press.
1491

1492 Mitchell, T. D., and P. D. Jones, 2005: An improved method of constructing a database of monthly
1493 climate observations and associated high-resolution grids. *Int. J. Climatol.*, **25**, 693–712.
1494

1495 Moffat, A. M., and Coauthors, 2007: Comprehensive comparison of gap-filling techniques for eddy
1496 covariance net carbon fluxes. *Agric. For. Meteorol.*, **147**, 209–232.
1497

1498 Moise, A. F., and F. P. Delage, 2011: New climate model metrics based on object orientated pattern
1499 matching of rainfall. *J. Geophys. Res.*, **116**, D12108, doi:10.1029/2010JD015318.
1500

1501 Moore, J. K., and Coauthors, 1999: SeaWiFS satellite ocean color data from the Southern Ocean.
1502 *Geophys. Res. Lett.*, **26**, 1465–1468.
1503

1504 Myneni, R., S. Hoffman, J. Glassy, Y. Zhang, P. Votava, R. Nemani, S. Running, and J. Privette,
1505 2002: Global products of vegetation leaf area and fraction absorbed PAR from year one of MODIS
1506 data. *Remote Sens. Environ.*, **83**, 214–231.
1507

1508 New, M., D. Lister, M. Hulme, and I. Makin, 2002: A high-resolution data set of surface climate over
1509 global land areas. *Climate Res.*, **21**, 1–25.
1510

1511 Olson, J. S., J. A. Watts, and L. J. Allison, 1985: Major World Ecosystem Complexes Ranked by
1512 Carbon in Live Vegetation (NDP-017), available at: (<http://cdiac.ornl.gov/ndp017.html>) from the
1513 Carbon Dioxide Information Center, U.S. Department of Energy, Oak Ridge National Laboratory, Oak
1514 Ridge TN.
1515

1516 Papale, D., M. Reichstein, M. Aubinet, E. Canfora, C. Bernhofer, W. Kutsch, B. Longdoz, S. Rambal,
1517 R. Valentini, T. Vesala, and D. Yakir, 2006: Towards a standardized processing of net ecosystem
1518 exchange measured with eddy covariance technique: Algorithms and uncertainty estimation.
1519 *Biogeosciences*, **3**, 1–13.
1520

1521 Perkins, S. E., A. J. Pitman, N. J. Holbrook, J. McAneney, 2007: Evaluation of the AR4 Climate
1522 Models’ Simulated Daily Maximum Temperature, Minimum Temperature, and Precipitation over
1523 Australia Using Probability Density Functions. *J. Climate*, **20**, 4356–4376.
1524

- 1525 Piao, S., P. Ciais, P. Friedlingstein, N. de Noblet-Ducoudre, P. Cadule, N. Viovy, and T. Wang, 2009:
1526 Spatiotemporal patterns of terrestrial carbon cycle during the 20th century. *Global Biogeochem.*
1527 *Cycles*, **23**, GB4026, doi:10.1029/2008GB003339.
- 1528
- 1529 Piao, S., and Coauthors, 2013: Evaluation of terrestrial carbon cycle models for their response to
1530 climate variability and to CO₂ trends. *Global Change Biol.*, In press.
- 1531
- 1532 Radić, V., and G. K. C. Clarke, 2011: Evaluation of IPCC Models' Performance in Simulating Late-
1533 Twentieth-Century Climatologies and Weather Patterns over North America. *J. Climate*, **24**, 5257–
1534 5274.
- 1535
- 1536 Räisänen, J., L. Ruokolainen, and J. Ylhäisi, 2010: Weighting of model results for improving best
1537 estimates of climate change. *Climate Dyn.*, **35**, 407–422.
- 1538
- 1539 Randall, D. A., and Coauthors, 2007: Climate models and their evaluation. *Climate Change 2007: The*
1540 *Physical Science Basis*, S. Solomon et al., Eds., Cambridge University Press
- 1541
- 1542 Rayner, N. A., D. E. Parker, E. B. Horton, C. K. Folland, L. V. Alexander, D. P. Rowell, E. C. Kent,
1543 and A. Kaplan, 2003: Global analyses of sea surface temperature, sea ice, and night marine air
1544 temperature since the late nineteenth century. *J. Geophys. Res.*, **108**, doi: 10.1029/2002JD002670.
- 1545
- 1546 Rayner, P., I. Enting, R. Francey, and R. Langenfelds, 1999: Reconstructing the recent carbon cycle
1547 from atmospheric CO₂, d13C, and O₂/N₂ observations. *Tellus*, **51**, 213–232.
- 1548
- 1549 Rayner, P., R. M. Law, C. E. Allison, R. J. Francey, C. M. Trudinger, and C. Pickett-Heaps, 2008:
1550 Interannual variability of the global carbon cycle (1992 – 2005) inferred by inversion of atmospheric
1551 CO₂ and d13CO₂ measurements. *Global Biogeochem. Cycles*, **22**, GB3008,
1552 doi:10.1029/2007GB003068.
- 1553
- 1554 Reichler, T., and J. Kim, 2008: How well do coupled models simulate today's climate? *Bull. Amer.*
1555 *Meteor. Soc.*, **89**, 303–311.
- 1556
- 1557 Reichstein, M., and Coauthors, 2005: On the separation of net ecosystem exchange into assimilation
1558 and ecosystem respiration: Review and improved algorithm. *Global Change Biol.*, **11**, 1424–1439.
- 1559
- 1560 Reifen, C., and R. Toumi, 2009: Climate projections: Past performance no guarantee of future skill?
1561 *Geophys. Res. Lett.*, **36**, L13704, doi:10.1029/2009GL038082.
- 1562
- 1563 Rintoul, S. R., and T. W. Trull, 2001: Seasonal evolution of the mixed layer in the Subantarctic Zone
1564 south of Australia. *J. Geophys. Res.*, **106**, 31447–31462.
- 1565
- 1566 Roujean, J.-L., and R. Lacaze, 2002: Global mapping of vegetation parameters from POLDER multi-
1567 angular measurements for studies of surface-atmosphere interactions: A pragmatic method and its
1568 validation. *J. Geophys. Res.*, **107**, doi:10.1029/2001JD000751.
- 1569
- 1570 Saleska, S. R., and Coauthors, 2003: Carbon in Amazon forests: unexpected seasonal fluxes and
1571 disturbance-induced losses. *Science*, **302**, 1554-1557.
- 1572
- 1573 Santer, B. D., and Coauthors, 2007: Identification of human-induced changes in atmospheric moisture
1574 content. *Proc. Natl. Acad. Sci. U. S. A.*, **104**, 15248–15253.
- 1575
- 1576 Santer, B. D., and Coauthors, 2009: Incorporating model quality information in climate change
1577 detection and attribution studies. *Proc. Natl. Acad. Sci. U. S. A.*, **106**, 14778–14783.

1578 Sarmiento, J. L., M. Gloor, N. Gruber, C. Beaulieu, A. R. Jacobson, S. M. Fletcher, S. Pacala, and K.
1579 Rodgers, 2009: Trends and regional distributions of land and ocean carbon sinks. *Biogeosciences*, **7**,
1580 2351–2367.

1581

1582 Schaefer, K., A. S. Denning, N. Suits, J. Kaduk, I. Baker, S. Los, and L. Prihodko, 2002: Effect of
1583 climate on interannual variability of terrestrial CO₂ fluxes. *Global Biogeochem. Cycles*, **16**, 1102–
1584 1029.

1585

1586 Scherrer, S. C., 2010: Present-day interannual variability of surface climate in CMIP3 models and its
1587 relation to future warming. *Int. J. Climatol.*, **31**, 1518–1529

1588

1589 Schneider, B., L. Bopp, M. Gehlen, J. Segschneider, T. L. Frölicher, P. Cadule, P. Friedlingstein, S. C.
1590 Doney, M. J. Behrenfeld, and F. Joos, 2008: Climate-induced interannual variability of marine export
1591 production in three global coupled carbon cycle models. *Biogeosciences*, **5**, 597–614.

1592

1593 Séférian, R., L. Bopp, M. Gehlen, J. Orr, C. Éthé, P. Cadule, O. Aumont, D. Salas-y-Mélia, A.
1594 Voltaire, and G. Madec, 2012: Skill Assessment of Three Earth System Models with Common
1595 Marine Biogeochemistry. *Climate Dyn*, **1-25**, doi:10.1007/s00382-012-1362-8

1596

1597 Shevliakova, E., S. W. Pacala, S. Malyshev, G. C. Hurtt, P. C. D. Milly, J. P. Caspersen, L. T.
1598 Sentman, J. P. Fisk, C. Wirth, and C. Crevoisier, 2009: Carbon cycling under 300 years of land use
1599 change: Importance of the secondary vegetation sink. *Global Biogeochem. Cycles*, **23**, GB2022,
1600 doi:10.1029/2007GB003176.

1601

1602 Silverman, B. W., 1986: Density Estimation for Statistics and Data Analysis. Chapman and Hall.

1603

1604 Sitch, S., P. Cox, W. J. Collins, and C. Huntingford, 2007: Indirect radiative forcing of climate change
1605 through ozone effects on the land–carbon sink. *Nature*, **448**, 791–794.

1606

1607 Smith, P., and Coauthors, 2012: Towards an integrated global framework to assess the impacts of land
1608 use and management change on soil carbon: current capability and future vision. *Global Change*
1609 *Biol.*, **18**, 2089–2101.

1610

1611 Solomon, S., D. Qin, M. Manning, M. Marquis, K. Averyt, M. M. B. Tignor, H. L. Miller Jr., and Z.
1612 Chen, Eds., 2007: *Climate Change 2007: The Physical Science Basis*. Cambridge University Press,
1613 996 pp.

1614

1615 Steinacher, M., F. Joos, T. L. Frölicher, L. Bopp, P. Cadule, V. Cocco, S. C. Doney, M. Gehlen, K.
1616 Lindsay, J. K. Moore, B. Schneider, J. Segschneider, 2010: Projected 21st century decrease in marine
1617 productivity: a multi-model analysis. *Biogeosciences*, **7**, 979–1005.

1618

1619 Stephens, B. B., and Coauthors, 2007: Weak northern and strong tropical land carbon uptake from
1620 vertical profiles of atmospheric CO₂. *Science*, **316**, 1732–1735.

1621

1622 Takahashi, T., and Coauthors, 2002: Global sea–air CO₂ flux based on climatological surface ocean
1623 pCO₂, and seasonal biological and temperature effects. *Deep-Sea Res.*, **49B**, 1601–1622.

1624

1625 Takahashi, T., and Coauthors, 2009: Climatological mean and decadal change in surface ocean pCO₂,
1626 and net sea–air CO₂ flux over the global oceans. *Deep-Sea Res.*, **56B**, 554–577.

1627

1628 Taylor, K. E., R. J. Stouffer, and G. Meehl, 2011: An Overview of CMIP5 and the Experiment
1629 Design. *Bull. Am. Meteorol. Soc.*, **93**, 485–498.

1630

1631 Tebaldi, C, K. Hayhoe, J. Arblaster, and G. A. Meehl, 2006: Going to the extremes. An
1632 intercomparison of model-simulated historical and future changes in extreme events. *Clim. Change*,
1633 **79**, 185– 211.

1634

1635 Tjiputra, J. F., K. Assmann, M. Bentsen, I. Bethke, O. H. Otterå, C. Sturm, and C. Heinze, 2009:
1636 Bergen earth system model (BCM-C): model description and regional climate-carbon cycle feedbacks
1637 assessment. *Geosci. Model Dev. Discuss.*, **2**, 845-887

1638

1639 Todd-Brown, K. E. O., J. T. Randerson, W. M. Post, F. M. Hoffman, C. Tarnocai, E. A. Schuur, and
1640 S. D. Allison, 2012: Causes of variation in soil carbon predictions from CMIP5 Earth system models
1641 and comparison with observations. *Biogeosciences Discuss.*, **9**, 14437-14473.

1642

1643 Volodin, E. M., N. A. Dianskii, and A. V. Gusev, 2010: Simulating Present Day Climate with the
1644 INMCM4.0 Coupled Model of the Atmospheric and Oceanic General Circulations. *Izv. Ocean. Atmos.*
1645 *Phys.*, **46**, 414–431.

1646

1647 Waliser, D., K.-W. Seo, S. Schubert, and E. Njoku, 2007: Global water cycle agreement in the climate
1648 models assessed in the IPCC AR4. *Geophys. Res. Lett.*, **34**, L16705, doi:10.1029/2007GL030675.

1649

1650 Watanabe, S., and Coauthors, 2011: MIROC-ESM, 2010: model description and basic results of
1651 CMIP5-20c3m experiments. *Geosci. Model Dev.*, **4**, 845-872.

1652

1653 Weiss, M., F. Baret, S. Garrigues, and R. Lacaze, 2007: LAI and fAPAR CYCLOPES global products
1654 derived from VEGETATION. Part 2: validation and comparison with MODIS collection 4 products.
1655 *Remote Sens. Environ.*, **110**, 317-331.

1656

1657 Welp, L.R., R. F. Keeling, H. A. J. Meijer, A. F. Bollenbacher, S. C. Piper, K. Yoshimura, R. J.
1658 Francey, C. E. Allison, and M. Wahlen., 2001: Interannual variability in the oxygen isotopes of
1659 atmospheric CO₂ driven by El Nino. *Nature*, **417**, 579-582.

1660

1661 Wild, M., and B. Liepert, 2010: The Earth radiation balance as driver of the global hydrological cycle.
1662 *Environ. Res. Lett.*, **5**, 025203, doi:10.1088/1748-9326/5/2/025203.

1663

1664 Wittenberg, A. T., 2009: Are historical records sufficient to constrain ENSO simulations? *Geophys.*
1665 *Res. Lett.*, **36**, L12702, doi:10.1029/2009GL038710.

1666

1667 Wittig, V. E., E. A. Ainsworth, S. L. Naidu, D. F. Karnosky, and S. P Long, 2009: Quantifying the
1668 impact of current and future tropospheric ozone on tree biomass, growth, physiology and
1669 biochemistry: a quantitative meta-analysis. *Global Change Biol.*, **15**, 396–424.

1670

1671 Xavier, P. K., J. P. Duvel, P. Braconnot, and F. J. Doblas-Reyes, 2010: An evaluation metric for
1672 interannual variability and its application to CMIP3 twentieth-century simulations. *J. Climate* **23**,
1673 3497–3508.

1674

1675 Yang, W., and Coauthors, 2006: MODIS leaf area index products: from validation to algorithm
1676 improvement. *IEEE Trans. Geosci. Remote Sens.*, **44**, 1885-1898.

1677

1678 Yin, L., R. Fu, E. Shevliakova, and R. Dickinson, 2012: How well can CMIP5 simulate precipitation
1679 and its controlling processes over tropical South America? *Clim. Dyn.*, doi:10.1007/s00382-012-1582-
1680 y

1681

1682 Yuan, H., Y. Dai, Z. Xiao, D. Ji, and S. Wei, 2011: Reprocessing the MODIS leaf area index products
1683 for land surface and climate modelling. *Remote Sens. Environ.*, **115**, 1171–1187.

1684 Zaehle, S., A. D. Friend, P. Friedlingstein, F. Dentener, P. Peylin, and M. Schulz, 2010: Carbon and
1685 nitrogen cycle dynamics in the O-CN land surface model: 2. Role of the nitrogen cycle in the
1686 historical terrestrial carbon balance. *Global Biogeochem. Cycles*, **24**, GB1006,
1687 doi:10.1029/2009GB003522.
1688
1689 Zeng, N., A. Mariotti, and P. Wetzel, 2005: Terrestrial mechanisms of interannual CO₂ variability,
1690 *Global Biogeochem. Cycles*, **19**, GB1016, doi:10.1029/2004GB002273.
1691
1692 Zhao, M., and S. W. Running, 2010: Drought-Induced Reduction in Global Terrestrial Net Primary
1693 Production from 2000 Through 2009. *Science*, **329**, 940–943.
1694
1695 Zhou, T., and R. Yu, 2006: Twentieth-Century Surface Air Temperature over China and the Globe
1696 Simulated by Coupled Climate Models. *J. Climate*, **19**, 5843–5858.
1697
1698 Zhu, Z., and Coauthors, 2013: Global Data Sets of Vegetation Leaf Area Index (LAI)_{3g} and Fraction
1699 of Photosynthetically Active Radiation (FPAR)_{3g} Derived from Global Inventory Modeling and
1700 Mapping Studies (GIMMS) Normalized Difference Vegetation Index (NDVI)_{3g} for the Period 1981
1701 to 2011. *Remote Sens.*, **5**, 927-948.
1702
1703

1704
1705
1706

Table 1. CMIP5 models used with the associated atmospheric and ocean grids, with the number of vertical levels.

MODELS	SOURCE	ATMOSPHERIC RESOLUTION (lon x lat, levels)	OCEAN RESOLUTION (lon x lat, levels)
BCC-CSM1.1	Beijing Climate Center, China Meteorological Administration, China	2.8125°x~2.8125°, L26	1°x(1-1/3)°, L40
BCC-CSM1.1-M	Beijing Climate Center, China Meteorological Administration, China	1.1°x~1.1°, L26	1°x(1-1/3)°, L40
BNU-ESM	Beijing Normal University	2.8125°x~2.8125°, L26	~1°x~0.6, L50
CanESM2	Canadian Centre for Climate Modelling and Analysis, Canada	2.8125°x~2.8125°, L35	1.40625°x~0.9375°, L40
CESM1-BGC	National Center for Atmospheric Research, United States	0.9°x1.25°, L26	384x320 points (gx1v3),L60
GFDL-ESM2G ^x	Geophysical Fluid Dynamics Laboratory, United States	2.5°x2°, L24	1°x~0.6, L63
GFDL-ESM2M ^x	Geophysical Fluid Dynamics Laboratory, United States	2.5°x2°, L24	1°x~0.6, L50
HadGEM2-CC ^y	Met Office Hadley Centre, UK	1.875°x1.25°, L60	1°x(1-0.3)°, L40
HadGEM2-ES ^y	Met Office Hadley Centre, UK	1.875°x1.25°, L38	1°x(1-0.3)°, L40
INMCM4	Institute for Numerical Mathematics, Russia	2°x1.5°, L21	1°x0.5°, L40
IPSL-CM5A-LR*	Institut Pierre Simon Laplace, France	3.75°x~1.875°, L39	~2°x~2°, L31
IPSL-CM5A-MR*	Institut Pierre Simon Laplace, France	2.5°x1.25°, L39	~2°x~2°, L31
IPSL-CM5B-LR*	Institut Pierre Simon Laplace, France	3.75°x1.875°, L39	~2°x~2°, L31
MIROC-ESM-CHEM ^z	Japan Agency for Marine-Earth Science and Technology, Japan; Atmosphere and Ocean Research Institute, Japan; National Institute for Environmental Studies, Japan	2.8125°x2.8125°, L80	1.40625°x~0.9375°, L44
MIROC-ESM ^z	Japan Agency for Marine-Earth Science and Technology, Japan; Atmosphere and Ocean Research Institute, Japan; National Institute for Environmental Studies, Japan	2.8125°x2.8125°, L80	1.40625°x~0.9375°, L44
MPI-ESM-LR	Max Planck Institute for Meteorology, Germany	1.875°x1.875°, L47	1.5°x~1.5°, L40
MPI-ESM-MR	Max Planck Institute for Meteorology, Germany	1.875°x1.875°, L47	~0.4°x~0.4°, L40
NorESM1-ME	Norwegian Climate Centre, Norway	2.5°x1.9°, L26	~1°x~0.5°, L53

1707
1708
1709
1710
1711
1712
1713
1714
1715
1716
1717
1718
1719
1720
1721
1722
1723
1724
1725
1726
1727
1728
1729
1730
1731
1732
1733
1734
1735

^x The two GFDL models differ almost exclusively in the physical ocean component; ESM2M uses Modular Ocean Model version 4.1 with vertical pressure layers, while ESM2G uses Generalized Ocean Layer Dynamics with a bulk mixed layer and interior isopycnal layers (Dunne et al. 2012).

^y HadGEM2 models differ for the number of vertical levels in the atmospheric component and for different representation of processes (HadGEM2-ES also reproduce the atmospheric chemistry, Martin et al. 2011).

* IPSL-CM5A-LR and IPSL-CM5A-MR models differ for the resolution of the atmospheric component, while IPSL-CM5A-LR and IPSL-CM5B-LR differ only for some parameterizations in the atmospheric model (Dufresne et al. 2012).

^z The difference between MIROC-ESM and MIROC-ESM-CHEM is that this latter simulates the atmospheric chemistry (Watanabe et al. 2011).

1736 **Table 2.** Summary of land and ocean biogeochemistry models used by ESMs and comparison of the
 1737 selected processes (dynamic vegetation, nitrogen cycling and land use change) for the only terrestrial
 1738 modules.
 1739

MODELS	LAND MODELS	DYNAMIC VEGETATION	N CYCLE	LUC	OCEAN MODELS
BCC-CSM1	BCC_AVIM1.0	Y	Y	N	Simple model into MOM4
BCC-CSM1-M	BCC_AVIM1.0	Y	Y	N	Simple model into MOM4
BNU-ESM	CoLM + BNU-DGVM	Y	N	Y	iBGC
CanESM2	CLASS2.7 + CTEM1	N	N	Y	CMOC
CESM1-BGC	CLM4	N	Y	Y	BEC
GFDL-ESM2G	LM3	Y	N	Y	TOPAZ2
GFDL-ESM2M	LM3	Y	N	Y	TOPAZ2
HadGEM2-CC	JULES + TRIFFID	Y	N	Y	Diat-HadOCC
HadGEM2-ES	JULES + TRIFFID	Y	N	Y	Diat-HadOCC
INMCM4	Simple model into INMCM4 atmospheric component	N	N	Y*	Simple model into INMCM4 ocean component
IPSL-CM5A-LR	ORCHIDEE	N	N	Y	PISCES
IPSL-CM5A-MR	ORCHIDEE	N	N	Y	PISCES
IPSL-CM5B-LR	ORCHIDEE	N	N	Y	PISCES
MIROC-ESM-CHEM	MATSIRO + SEIB-DGVM	Y	N	Y	NPZD
MIROC-ESM	MATSIRO + SEIB-DGVM	Y	N	Y	NPZD
MPI-ESM-LR	JSBACH + BETHY	Y	N	Y	HAMOCC5
MPI-ESM-MR	JSBACH + BETHY	Y	N	Y	HAMOCC5
NorESM1-ME	CLM4	N	Y	Y	HAMOCC5

1740
 1741 * In INMCM4 land use change was prescribed at low preindustrial level.
 1742

1743
1744
1745
1746
1747

Table 3. Temporal range of available data for historical simulation, and variable used in this study, with associated the number of independent realization for each variable. Note that not all the variables for all the ensembles are available on PDMDI server.

MODELS	PHYSICAL VARIABLES				BIOLOGICAL VARIABLES						
	LAND		OCEAN		LAND					OCEAN	
	Surface Temperature	Precipitation	SST	MLD	GPP	LAI	NBP	SoilC	VegC	fgCO ₂	PP
BCC-CSM1-1	3	3	3	n/a	3	3	n/a	3	3	3	n/a
BCC-CSM1-1-M	3	3	3	n/a	3	3	n/a	3	3	3	n/a
BNU-ESM	1	1	1 [*]	n/a	1	1	1	1	1	1	n/a
CanESM2	5	5	5	1	5	5	5	5	5	5	5
CESM1-BGC	1	1	1	1	1	1	1	1	1	1	1
GFDL-ESM2G	1	1	1	1	1	1	1	1	1	1	1
GFDL-ESM2M	1	1	1	1	1	1	1	1	1	1	1
HadGEM2-CC	1	1	1	1	1	1	1	1	1	1	1
HadGEM2-ES	4	4	4	1	4	4	4	4	4	4	4
INMCM4	1	1	1	n/a	1	1	1 ^y	1	1	1	n/a
IPSL-CM5A-LR	5	5	5	5	5	5	5	5	5	5	5
IPSL-CM5A-MR	1	1	1	1	1	1	1	1	1	1	1
IPSL-CM5B-LR	1	1	1	1	1	1	1	1	1	1	1
MIROC-ESM-CHEM	1	1	1	1 ^x	1	1	1	1	1	1	1
MIROC-ESM	3	3	1	1 ^x	3	3	3	3	3	3	1
MPI-ESM-LR	3	3	3	3	3	3	3	3	3	3	3
MPI-ESM-MR	3	3	3	3	3	3	3	3	3	3	3
NorESM1-ME	1	1	1	1	1	1	1	1	1	1	1

1748
1749
1750
1751
1752
1753
1754
1755
1756
1757
1758
1759

^x MLD from MIROC models was not directly provided as output, but it has been estimated from potential temperature, potential density and salinity.

^{*} Monthly SST were not available on the server; we used daily SST in the reference period 1950-2005 to compute the monthly SST.

^y In INMCM4 the land use was prescribed at preindustrial level and kept constant during the whole simulation; this means that the provided NBP does not include the LUC term and therefore it should be considered as NEP rather NBP. For this reason we decided to exclude the INMCM4 NBP from our analysis.

1760
1761
1762

Table 4. *Observationally-based data sets used to validate models. The spatial resolution is given as latitude x longitude.*

VARIABLES	REFERENCE	TEMPORAL WINDOW	SPATIAL RESOLUTION	TEMPORAL RESOLUTION
Temperature	CRU (Mitchell and Jones 2005)	1901-2006	Global (land), 0.5°x0.5°	Monthly
Precipitation	CRU (Mitchell and Jones 2005)	1901-2006	Global (land), 0.5°x0.5°	Monthly
SST	HadISST (Rayner et al. 2003)	1870-2011	Global, 1°x1°	Monthly
MLD	de Boyer Montégut et al. (2004)	1941-2008	Global, 2°x2°	Climatology
GPP	MTE (Jung et al. 2009)	1982-2008	Global, 0.5°x0.5°	Monthly
LAI	LAI3g (Zhu et al. 2013)	1981-2011	Global, ~0.08°x ~0.08°	15 Days
NBP	Inversion (Gurney et al. 2004)	1995-2008	Global, 0.5°x0.5°	Monthly
	GCP (Le Quéré et al. 2009)	1959-2008	Global, spatial average	Yearly
Soil Carbon	HSWD, (FAO 2012)	n/a	Global, 1 km x1 km	Annual Value
Vegetation Carbon	NDP-017b (Gibbs 2006)	n/a	Global, 0.5x0.5	Annual Value
fgCO2	Inversion (Gurney et al. 2004)	1995-2008	Global, 0.5°x0.5°	Monthly
	GCP (Le Quéré et al. 2009)	1959-2008	Global, spatial average	Yearly
	Takahashi (Takahashi et al. 2009)	2000	Global, 4°x5°	Climatology
NPP	SeaWIFS. (Behrenfeld and Falkowski, 1997)	1998-2007	Global, 6x6 km	Monthly

1763
1764
1765
1766
1767
1768
1769
1770
1771
1772
1773
1774
1775
1776
1777
1778
1779
1780
1781
1782
1783
1784
1785
1786
1787
1788
1789
1790
1791
1792
1793
1794
1795
1796
1797

1798 **Table 5.** Skill score values with the corresponding weights used to compute regional estimates.
 1799

<i>SKILL SCORE</i>	<i>WEIGHT</i>
$Z_{x,y} < 0.05$	0.05
$0.05 \leq Z_{x,y} < 0.25$	0.1
$0.25 \leq Z_{x,y} < 0.5$	0.15
$0.5 \leq Z_{x,y} < 0.75$	0.25
$Z_{x,y} \geq 0.75$	0.45

1800
 1801
 1802
 1803
 1804
 1805
 1806
 1807
 1808
 1809
 1810
 1811
 1812
 1813
 1814
 1815
 1816
 1817
 1818
 1819
 1820
 1821

1822 **FIGURE CAPTIONS**

1823

1824 **Figure 1.** Globally averaged surface air temperature (only land points, without Antarctica) from
1825 observations (CRU), and as simulated by CMIP5 models in response to major forcings, natural and
1826 anthropogenic (upper panel). The anomaly has been computed with respect to the reference period
1827 1901-1930.

1828 Vertical grey lines indicate the timing of major volcanic eruptions, while orange line shows the most
1829 intense El-Niño event occurred in the 20th century. The grey shaded area represents range of
1830 variability of the 18 CMIP5 models, i.e. the envelope of positive and negative temperature extremes
1831 based on multi-model mean, while the red shading shows the confidence interval diagnosed from the
1832 ensemble standard deviation assuming a *t*-distribution centred on the ensemble mean (white curve).

1833 Lower panels show inter-comparison of surface temperature over land estimated by 18 different
1834 CMIP5 models (circles) with reference temperature estimated by CRU dataset (triangles) for the
1835 whole Globe, Southern Hemisphere (20°S-90°S, without Antarctica), Northern Hemisphere (20°N-
1836 90°N), and Tropic (20°S-20°N). Scatter plot shows multi-year average temperature in x-axis computed
1837 during the period 1986-2005, its linear trend in y-axis over the full period 1901-2005, and the Model
1838 Variability Index (MVI).

1839

1840 **Figure 2.** As Figure 1 but for land precipitation.

1841

1842 **Figure 3.** As Figure 1 but for SST. The regional SST are computed over the ocean sub-regions rather
1843 than over the land sub-domains. The reference SST dataset is HadISST. Note that BNU-ESM trend has
1844 been computed over the period 1950-2005 due to the unavailability of data on PCMDI server; in
1845 addition, in the upper panel BNU-ESM has been excluded by the analysis.

1846

1847 **Figure 4.** Simulated and observed climatological seasonal cycle of MLD (meters) for each ocean sub-
1848 domain.

1849 **Figure 5.** Temporal variability of CMIP5 global land-atmosphere CO₂ flux compared to Global
1850 Carbon Project (GCP) estimates (black line). Green shading shows the confidence interval diagnosed
1851 from the CMIP5 ensemble standard deviation assuming a t-distribution centred on the ensemble mean
1852 (white curve), while the grey shading represents the range of variability of CMIP5 models. Positive
1853 values correspond to land uptake.

1854

1855 **Figure 6.** Error-bar plot showing the 1986-2005 CMIP5 integrated NBP over the land sub-domains.
1856 Positive values correspond to land uptake, and vertical bars are computed considering the
1857 interannual variation. At global scale CMIP5 models are compared also with GCP estimates, while in
1858 all the other sub-regions the reference observations are inversion estimates (triangles).

1859

1860 **Figure 7.** Comparison of mean annual cycle of NBP (PgC/y) as simulated by CMIP5 models and JMA
1861 inversion in the 20-year period 1986-2005.

1862

1863 **Figure 8.** Integrated GPP over the land sub-domains. The linear trend has been computed over the
1864 period 1986-2005, and the reference dataset is MTE-GPP.

1865

1866 **Figure 9.** Comparison of mean annual cycle of GPP (PgC/y) as simulated by CMIP5 models with
1867 MTE-GPP data over the 20-year period 1986-2005.

1868

1869 **Figure 10.** Mean annual LAI as simulated by CMIP5 models and the reference LAI3g data (black
1870 triangle) over the land sub-domains.

1871

1872 **Figure 11.** Mean annual cycle of LAI over the period 1986-2005.

1873

1874 **Figure 12.** Simulated CMIP5 soil and vegetation carbon content over the period 1986-2005 compared
1875 against the Harmonized World Soil Database (HWSD) and the NDP-017 vegetation data.

1876 **Figure 13.** Temporal variability of CMIP5 global ocean-atmosphere CO₂ flux compared to Global
1877 Carbon Project (GCP) estimates (black line). Blue shading shows the confidence interval diagnosed
1878 from the CMIP5 ensemble standard deviation assuming a *t*-distribution centred on the ensemble mean
1879 (white curve), while the grey shading represents the range of variability of CMIP5 models. Positive
1880 values correspond to ocean uptake.

1881

1882 **Figure 14.** Error-bar plot showing the 1986-2005 CMIP5 means and standard deviations of ocean-
1883 atmosphere carbon fluxes (fgCO₂) in the chosen ocean sub-domains. Positive values correspond to
1884 ocean uptake, while vertical bars are computed considering the interannual variation. At global scale
1885 CMIP5 models are compared also with GCP estimates, while in all the other sub-regions the
1886 reference observations are JMA inversion estimates and Takahashi data (triangles).

1887

1888 **Figure 15.** Comparison of mean annual cycle of fgCO₂ (PgC/y) as simulated by CMIP5 models with
1889 JMA inversion and Takahashi data in the 20-year period 1986-2005.

1890

1891 **Figure 16.** Ocean primary production integrated over the ocean sub-domains as simulated by CMIP5
1892 models and observed (SeaWIFS) in the period 1998-2005.

1893

1894 **Figure 17.** Comparison of ocean primary production (PgC/y) mean annual cycle as simulated by
1895 CMIP5 models and SeaWIFS observations in the period 1998-2005.

1896

1897 **Figure 18.** Seasonal skill score matrix as computed according to Equation 3 for the whole Globe,
1898 Southern Hemisphere (20°S-90°S), Northern Hemisphere (20°N-90°N), and Tropic (20°S-20°N). A
1899 score of 0 indicates poor performance of models reproducing the phase and amplitude of the reference
1900 mean annual cycle, while a perfect score is equal to 1.

1901

1902 **Figure 19.** PDF-based skill scores for temperature, precipitation, LAI, and NBP for the

1903 whole Globe, Southern Hemisphere (20°S - 90°S), Northern Hemisphere (20°N - 90°N), and Tropic
1904 (20°S - 20°N). A perfect score is 1.

1905 Note that since the reference data for the soil and vegetation carbon pools are a single annual data,
1906 we were unable to build the PDF, therefore the skill scores for these variables are based on the
1907 normalized mean bias between the model and the reference data (see equation 6).

1908

1909 **Figure 20.** As Figure 18 but for the ocean variables.

1910

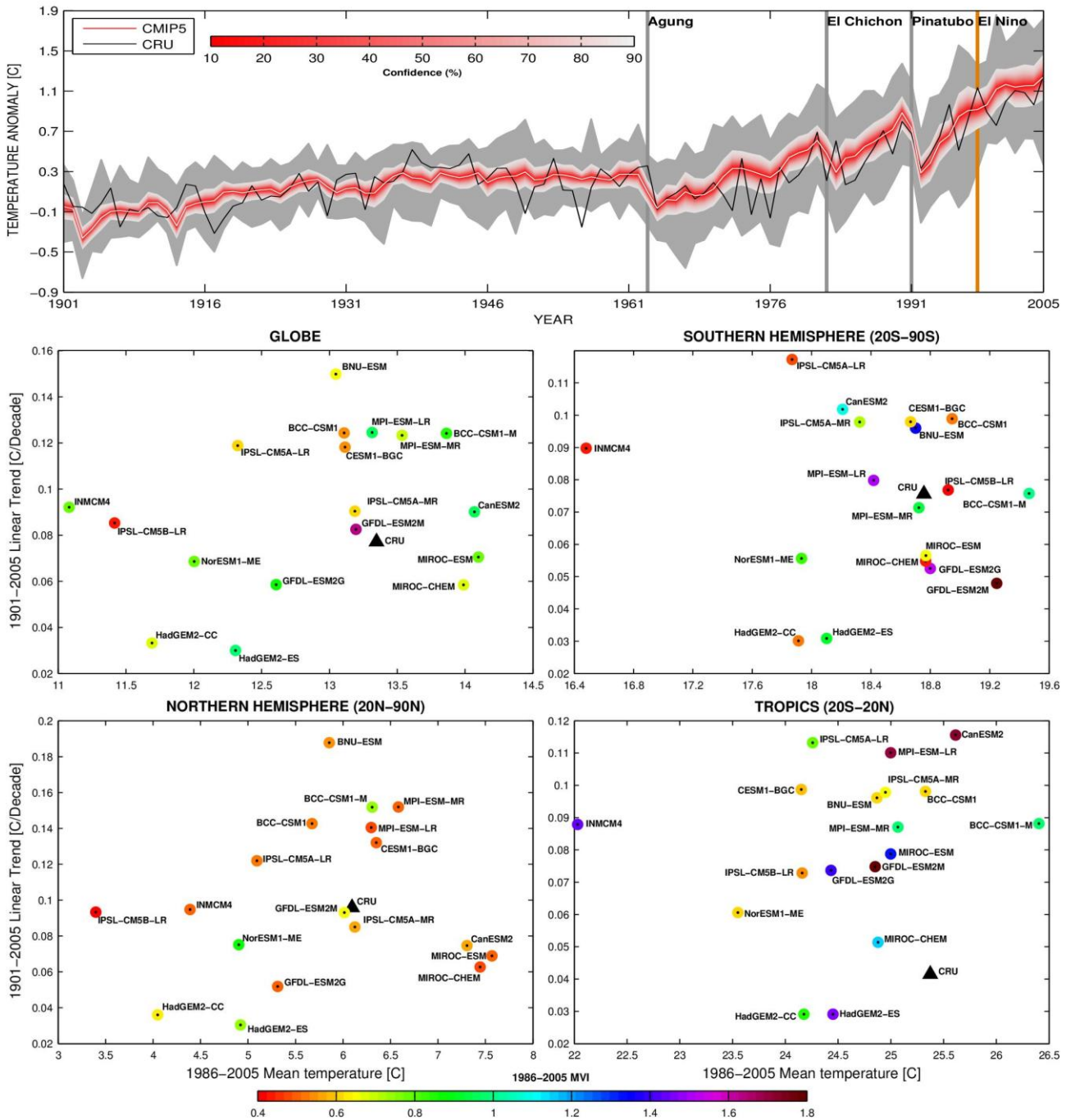
1911

1912 **Figure 21.** As Figure 19 but for the ocean variables. Note that since the MLD dataset is a climatology

1913 we were unable to compute the PDF, consequently the skill scores have been computed according to

1914 equation 6.

1915



1916
1917

1918

1919

1920

1921

1922

1923

1924

1925

1926

1927

1928

1929

1930

1931

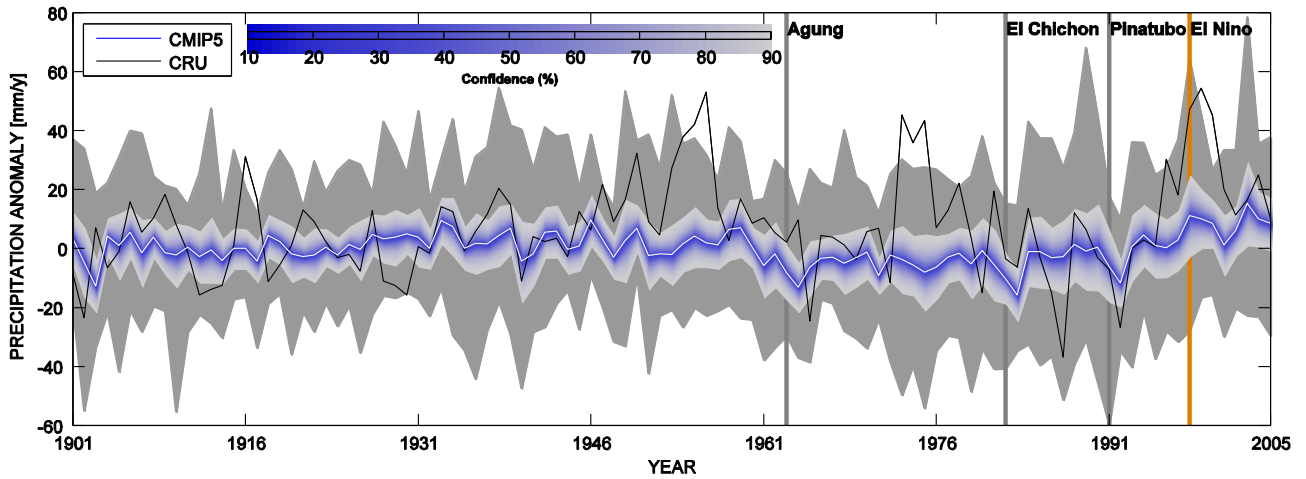
1932

1933

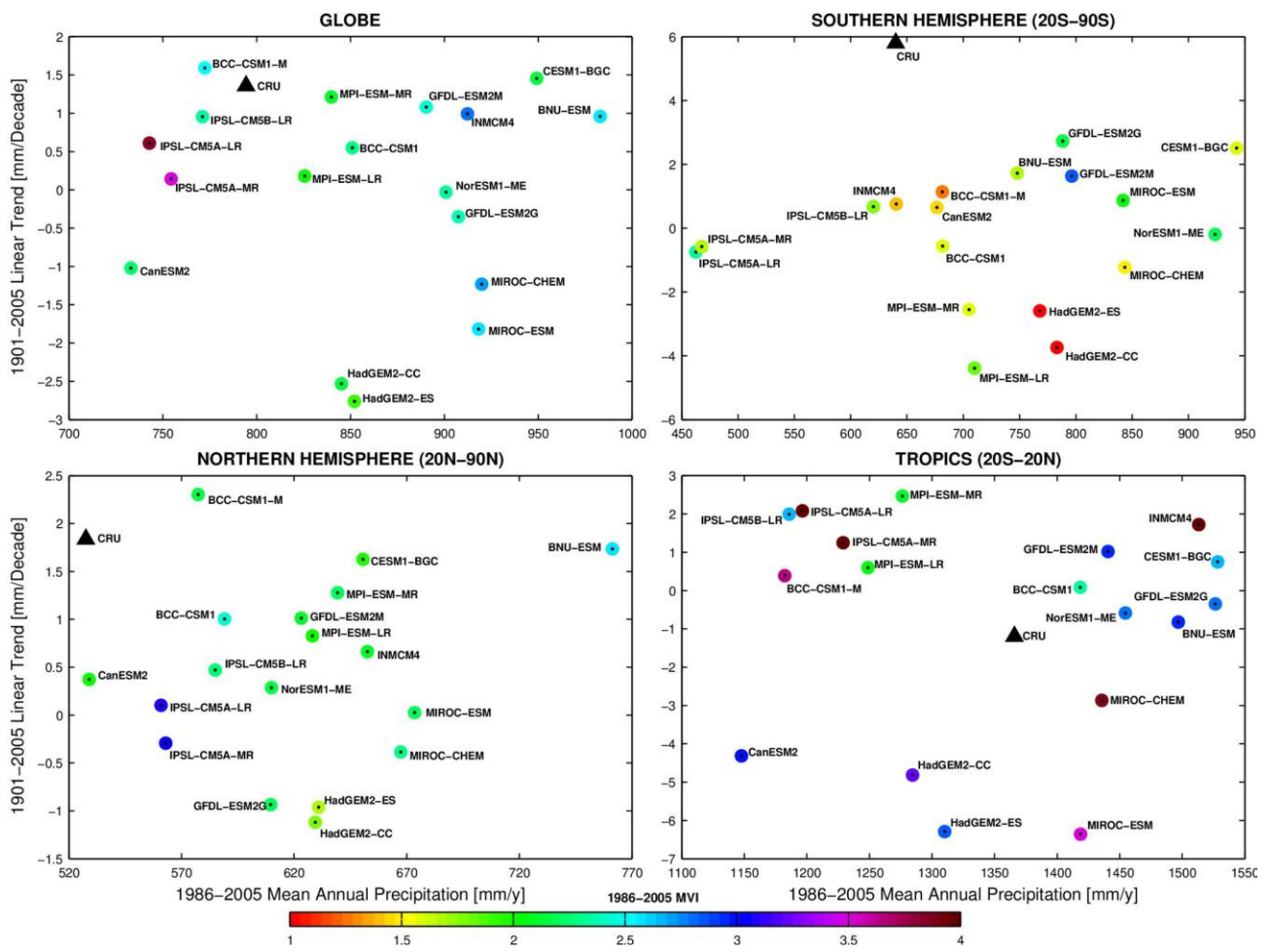
Figure 1. Globally averaged surface air temperature (only land points, without Antarctica) from observations (CRU), and as simulated by CMIP5 models in response to major forcings, natural and anthropogenic (upper panel). The anomaly has been computed with respect to the reference period 1901-1930.

Vertical grey lines indicate the timing of major volcanic eruptions, while orange line shows the most intense El-Niño event occurred in the 20th century. The grey shaded area represents range of variability of the 18 CMIP5 models, i.e. the envelope of positive and negative temperature extremes based on multi-model mean, while the red shading shows the confidence interval diagnosed from the ensemble standard deviation assuming a t-distribution centred on the ensemble mean (white curve).

Lower panels show inter-comparison of surface temperature over land estimated by 18 different CMIP5 models (circles) with reference temperature estimated by CRU dataset (triangles) for the whole Globe, Southern Hemisphere (20°S-90°S, without Antarctica), Northern Hemisphere (20°N-90°N), and Tropic (20°S-20°N). Scatter plot shows multi-year average temperature in x-axis computed during the period 1986-2005, its linear trend in y-axis over the full period 1901-2005, and the Model Variability Index (MVI).



1934
1935



1936
1937
1938
1939
1940
1941
1942
1943

Figure 2. As Figure 1 but for land precipitation.

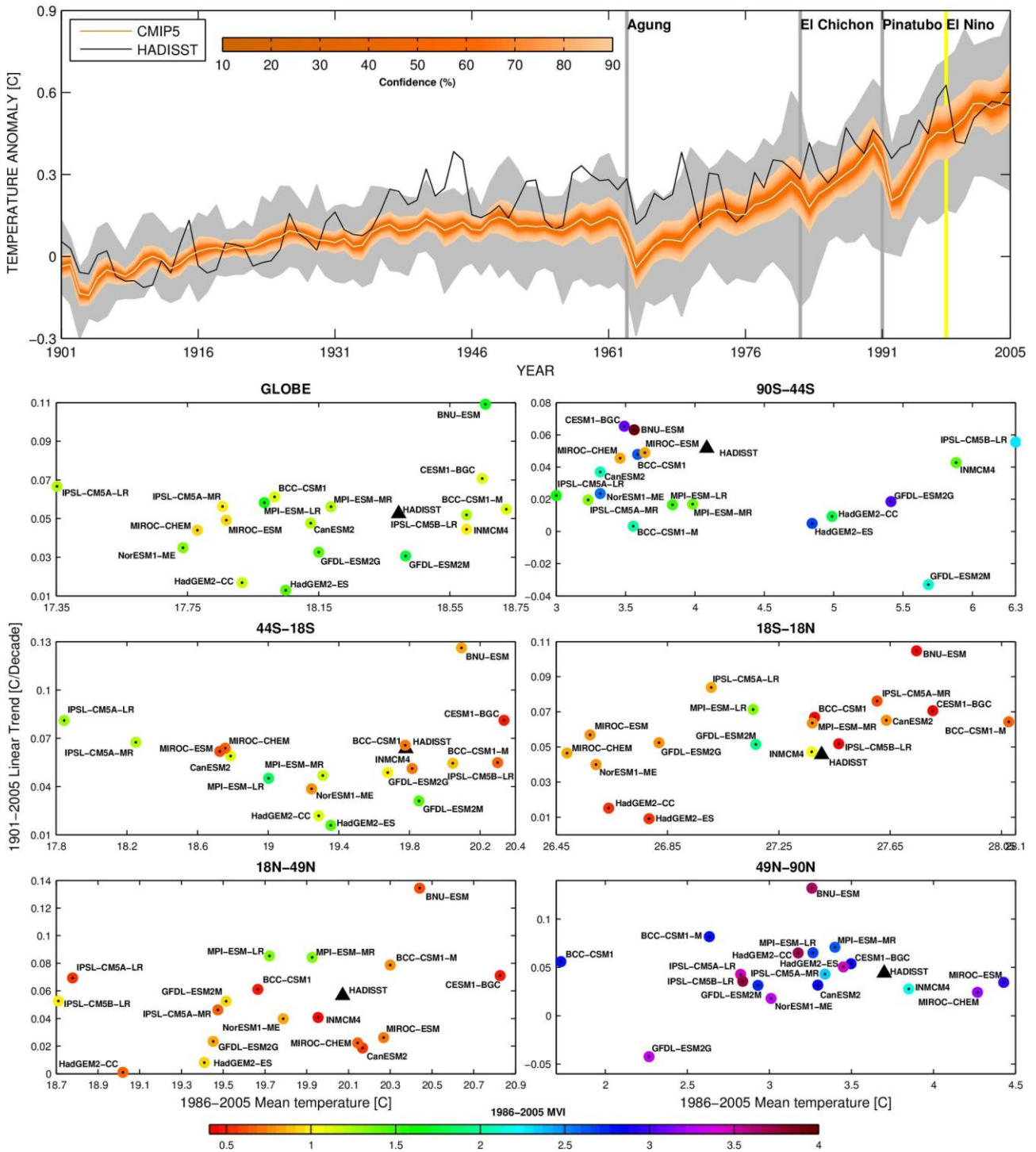


Figure 3. As **Figure 1** but for SST. The regional SST are computed over the ocean sub-regions rather than over the land sub-domains. The reference SST dataset is HadISST. Note that BNU-ESM trend has been computed over the period 1950-2005 due to the unavailability of data on PCMDI server; in addition, in the upper panel BNU-ESM has been excluded by the analysis.

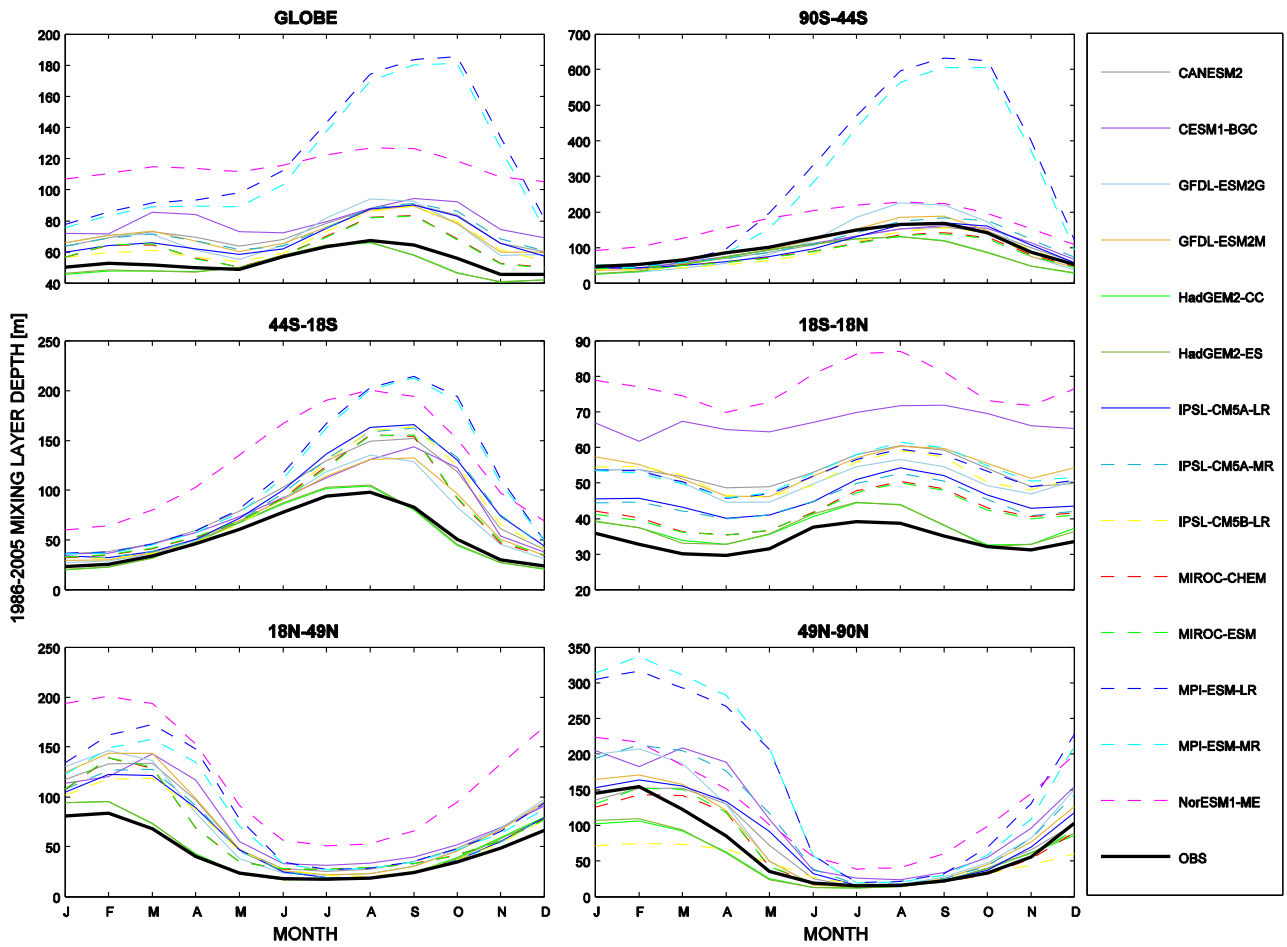
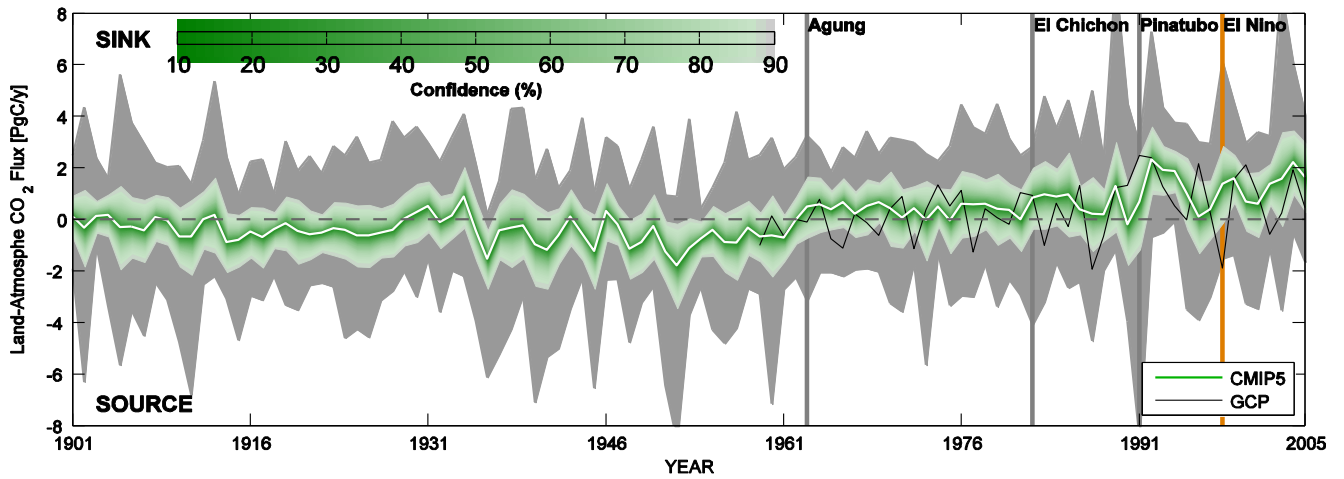


Figure 4. Simulated and observed climatological seasonal cycle of MLD (meters) for each ocean sub-domain.

1953
 1954
 1955
 1956
 1957
 1958
 1959
 1960
 1961
 1962
 1963
 1964
 1965
 1966
 1967
 1968
 1969
 1970



1971
 1972
 1973
 1974
 1975
 1976
 1977
 1978
 1979

Figure 5. Temporal variability of CMIP5 global land-atmosphere CO₂ flux compared to Global Carbon Project (GCP) estimates (black line). Green shading shows the confidence interval diagnosed from the CMIP5 ensemble standard deviation assuming a t-distribution centred on the ensemble mean (white curve), while the grey shading represents the range of variability of CMIP5 models. Positive values correspond to land uptake.

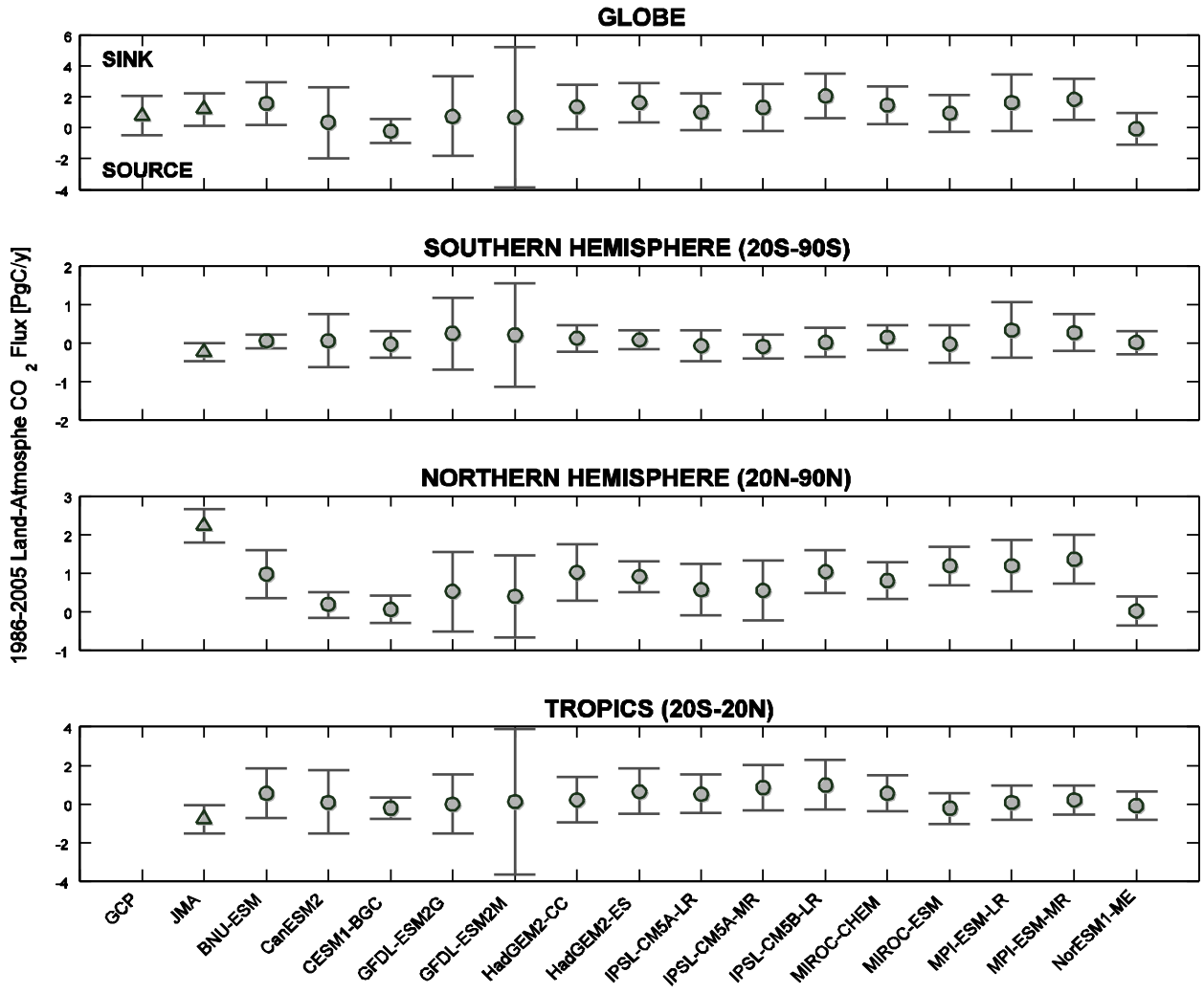
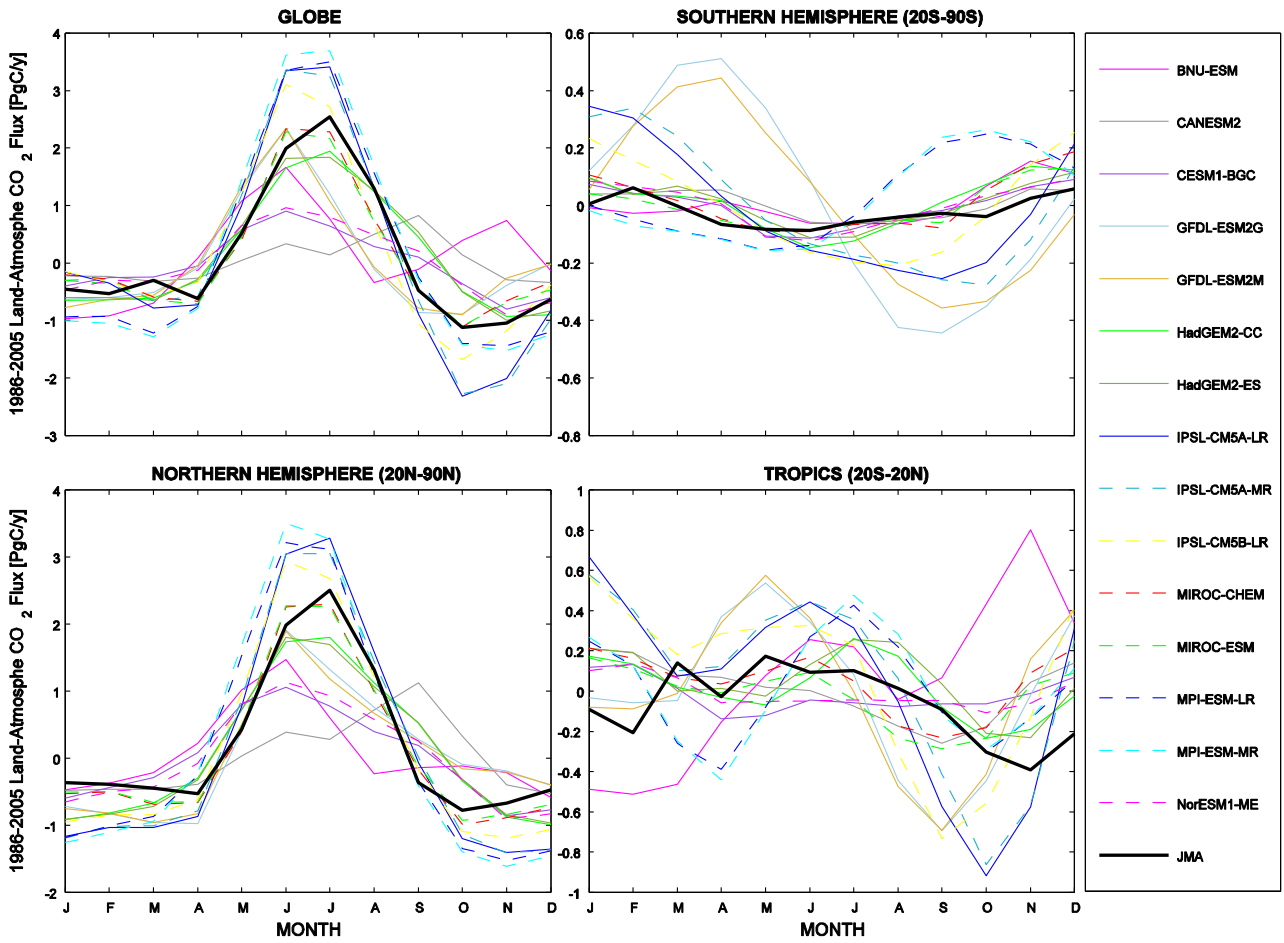


Figure 6. Error-bar plot showing the 1986-2005 CMIP5 integrated NBP over the land sub-domains. Positive values correspond to land uptake, and vertical bars are computed considering the interannual variation. At global scale CMIP5 models are compared also with GCP estimates, while in all the other sub-regions the reference observations are inversion estimates (triangles).

1980
1981
1982
1983
1984
1985
1986



1987
1988
1989
1990
1991

Figure 7. Comparison of mean annual cycle of NBP (PgC/y) as simulated by CMIP5 models and JMA inversion in the 20-year period 1986-2005.

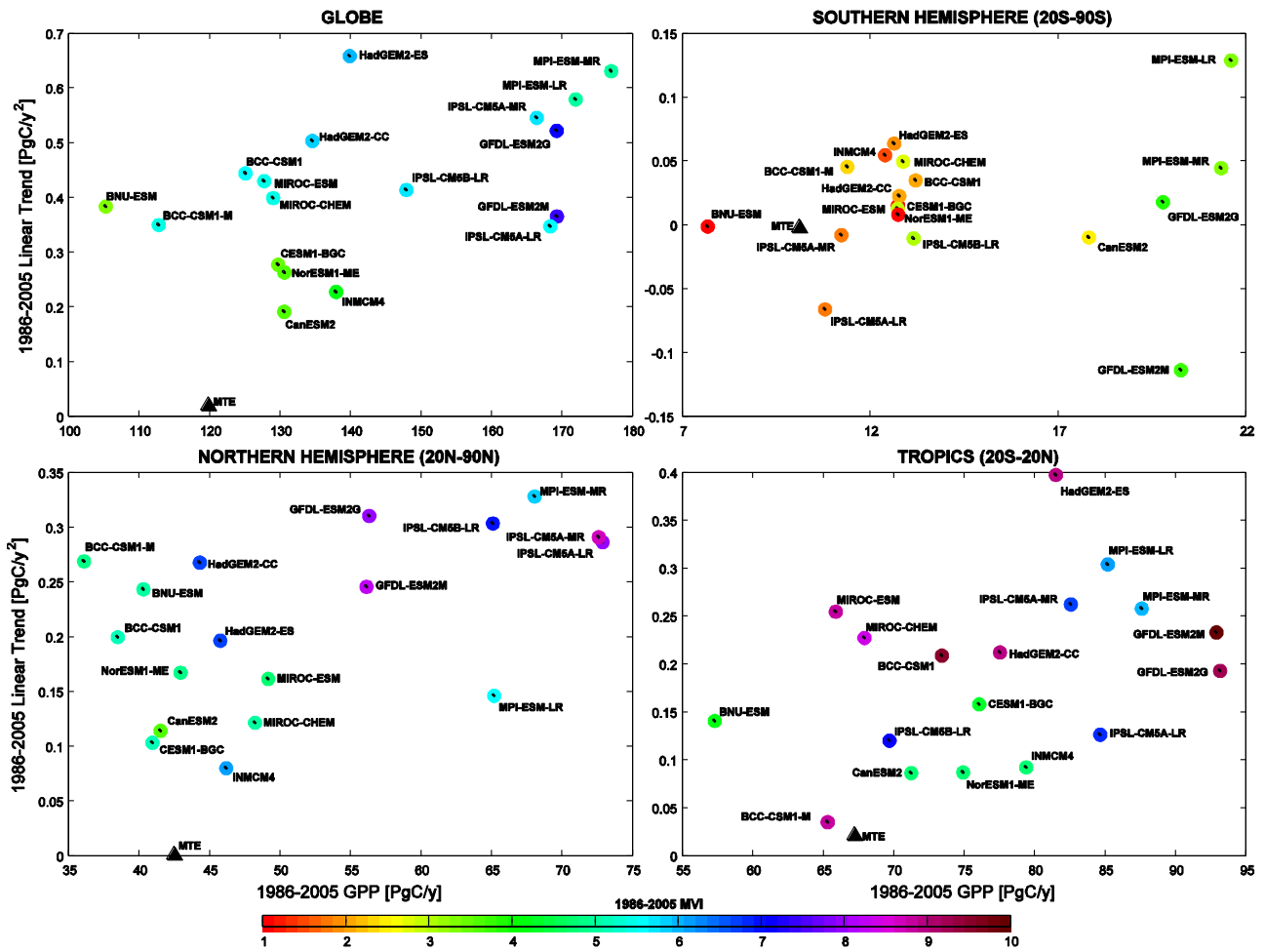
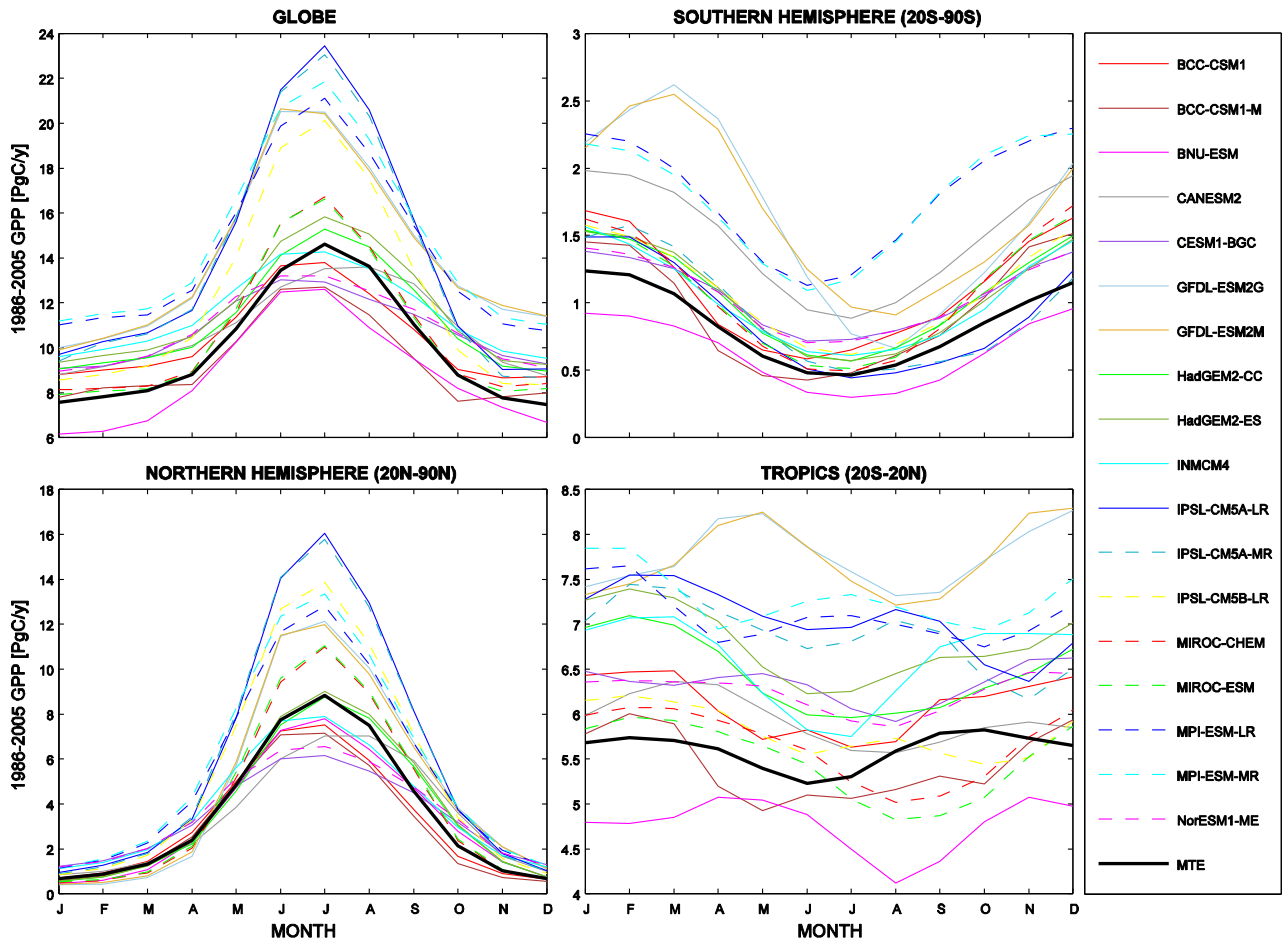


Figure 8. Integrated GPP over the land sub-domains. The linear trend has been computed over the period 1986-2005, and the reference dataset is MTE-GPP.

1992
1993
1994
1995
1996



1997
1998
1999
2000
2001
2002
2003

Figure 9. Comparison of mean annual cycle of GPP (PgC/y) as simulated by CMIP5 models with MTE-GPP data over the 20-year period 1986-2005.

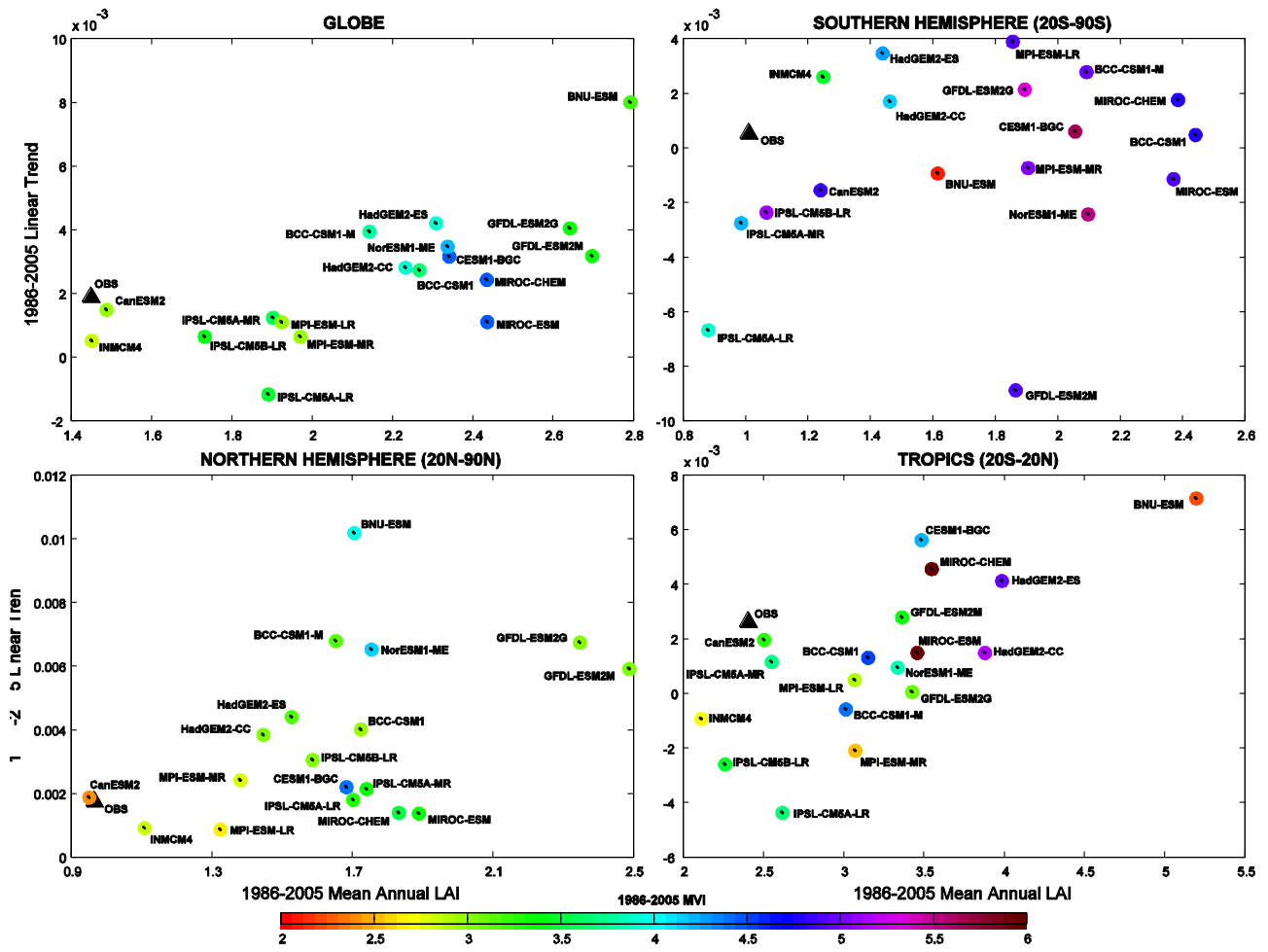


Figure 10. Mean annual LAI as simulated by CMIP5 models and reference LAI3g data (black triangle) over the land sub-domains.

2004
2005
2006
2007
2008

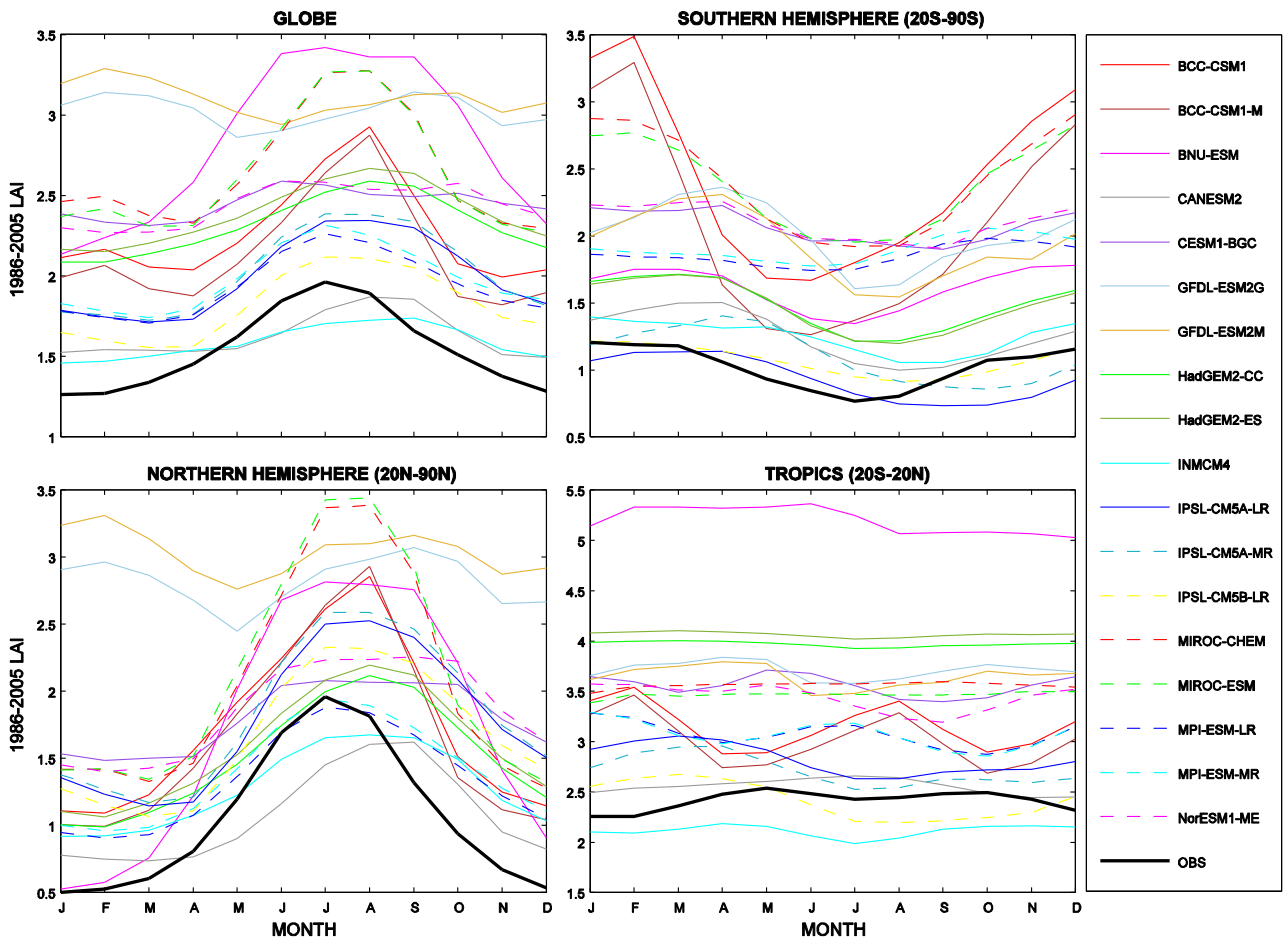


Figure 11. Mean annual cycle of LAI over the period 1986-2005.

2009
2010
2011
2012
2013
2014
2015
2016
2017
2018
2019
2020
2021
2022
2023
2024
2025
2026
2027
2028
2029
2030
2031
2032
2033
2034

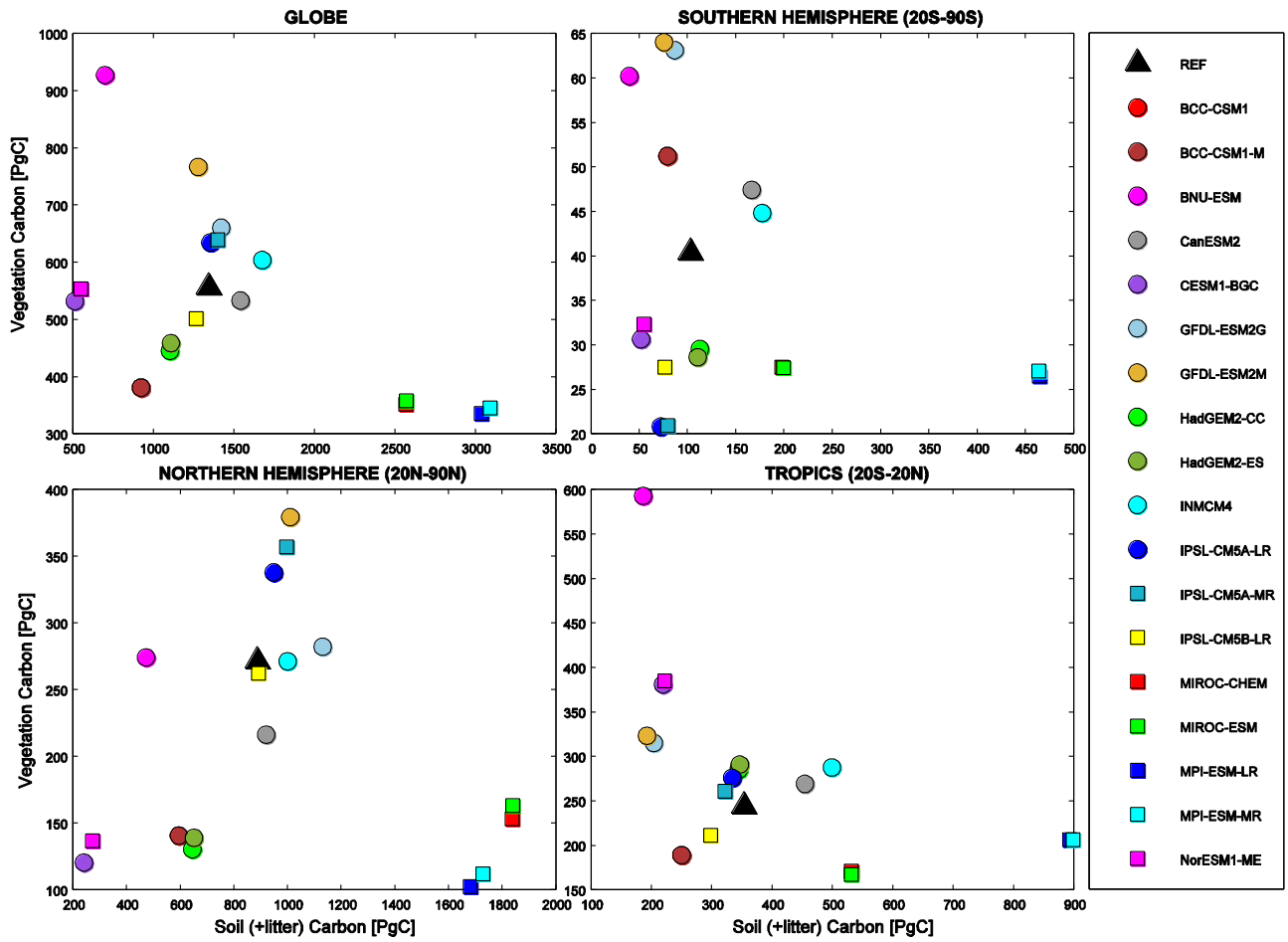
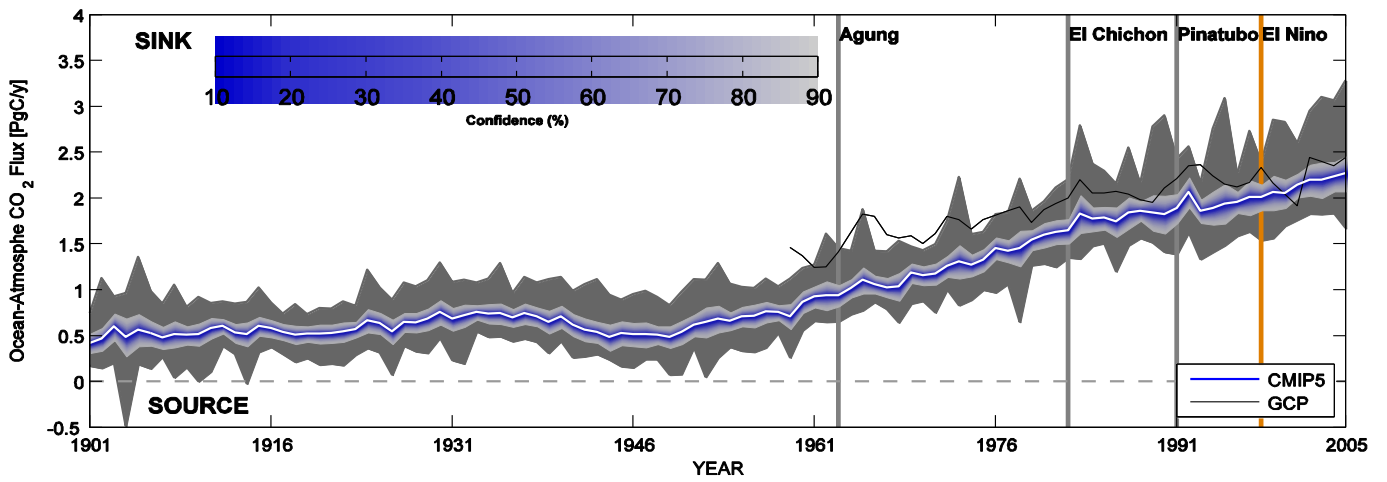


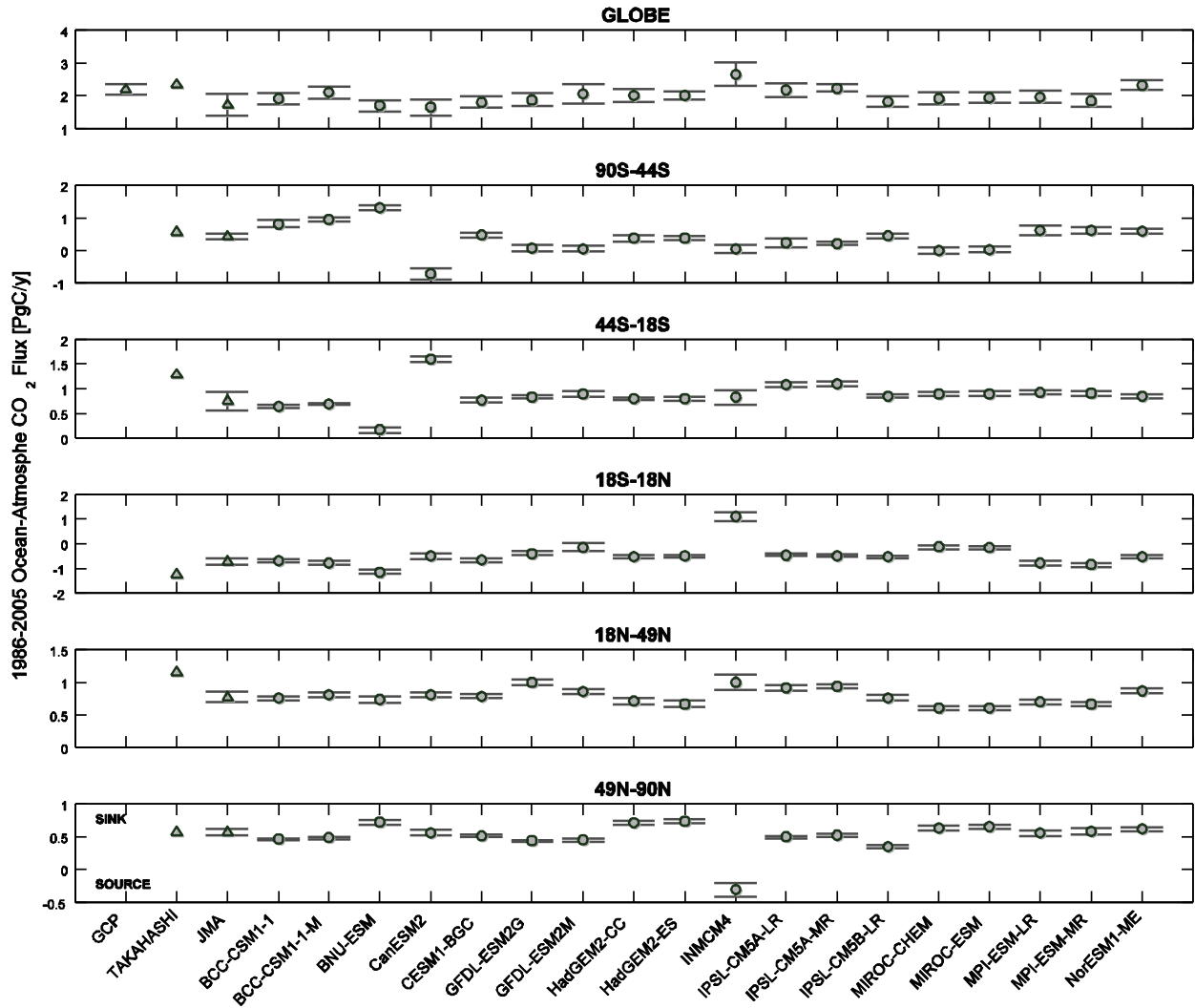
Figure 12. Simulated CMIP5 soil and vegetation carbon content over the period 1986-2005 compared against the Harmonized World Soil Database (HWSD) and the NDP-017 vegetation data.

2035
 2036
 2037
 2038
 2039
 2040
 2041
 2042
 2043
 2044
 2045
 2046
 2047
 2048
 2049
 2050



2051
 2052
 2053
 2054
 2055
 2056
 2057
 2058

Figure 13. Temporal variability of CMIP5 global ocean-atmosphere CO₂ flux compared to Global Carbon Project (GCP) estimates (black line). Blue shading shows the confidence interval diagnosed from the CMIP5 ensemble standard deviation assuming a t-distribution centred on the ensemble mean (white curve), while the grey shading represents the range of variability of CMIP5 models. Positive values correspond to ocean uptake.



2059
 2060
 2061
 2062
 2063
 2064
 2065

Figure 14. Error-bar plot showing the 1986-2005 CMIP5 means and standard deviations of ocean-atmosphere carbon fluxes (fgCO₂) in the chosen ocean sub-domains. Positive values correspond to ocean uptake, while vertical bars are computed considering the interannual variation. At global scale CMIP5 models are compared also with GCP estimates, while in all the other sub-regions the reference observations are JMA inversion estimates and Takahashi data (triangles).

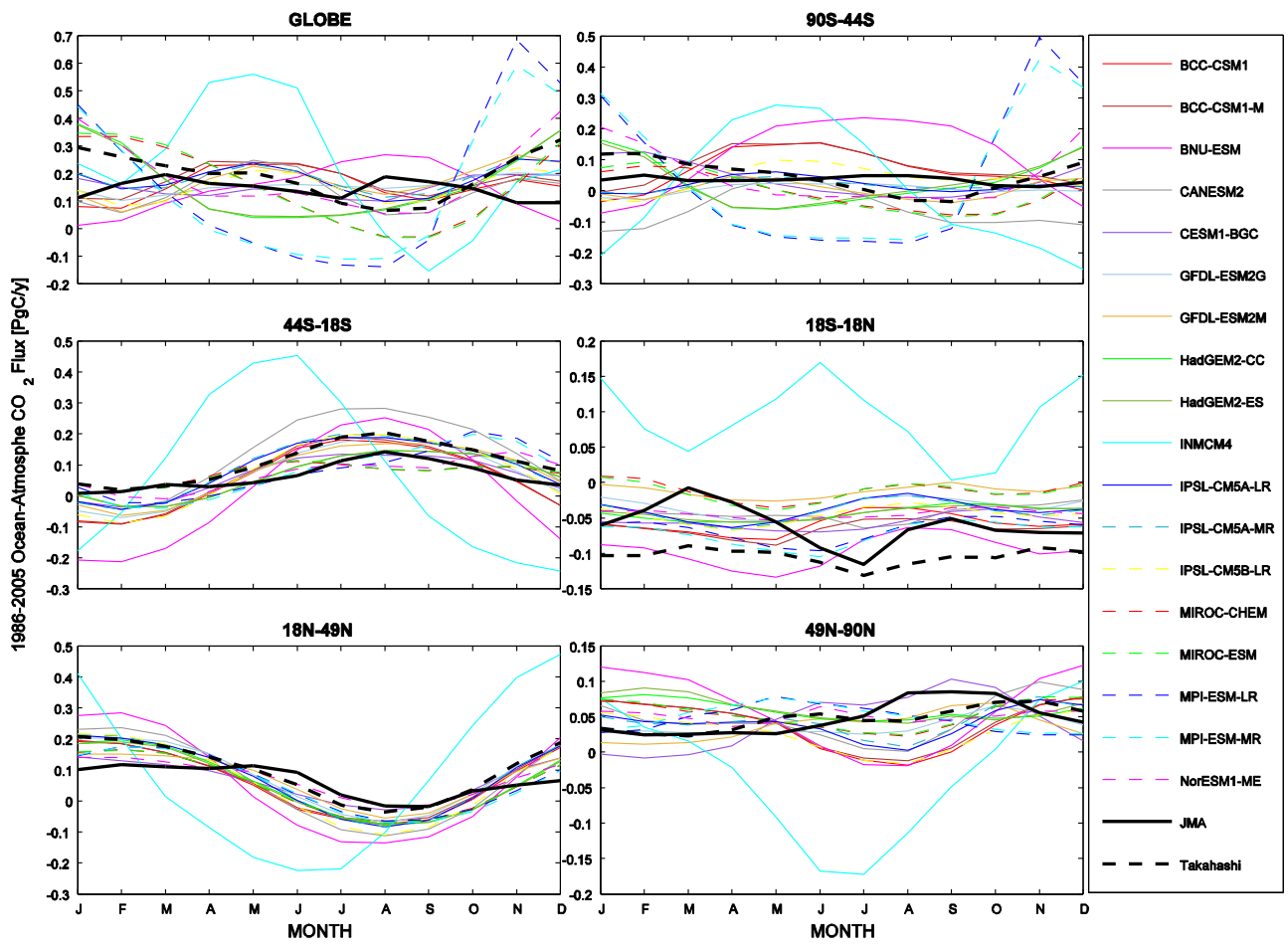


Figure 15. Comparison of mean annual cycle of fgCO₂ (PgC/y) as simulated by CMIP5 models with JMA inversion and Takahashi data in the 20-year period 1986-2005.

2066
2067
2068
2069
2070

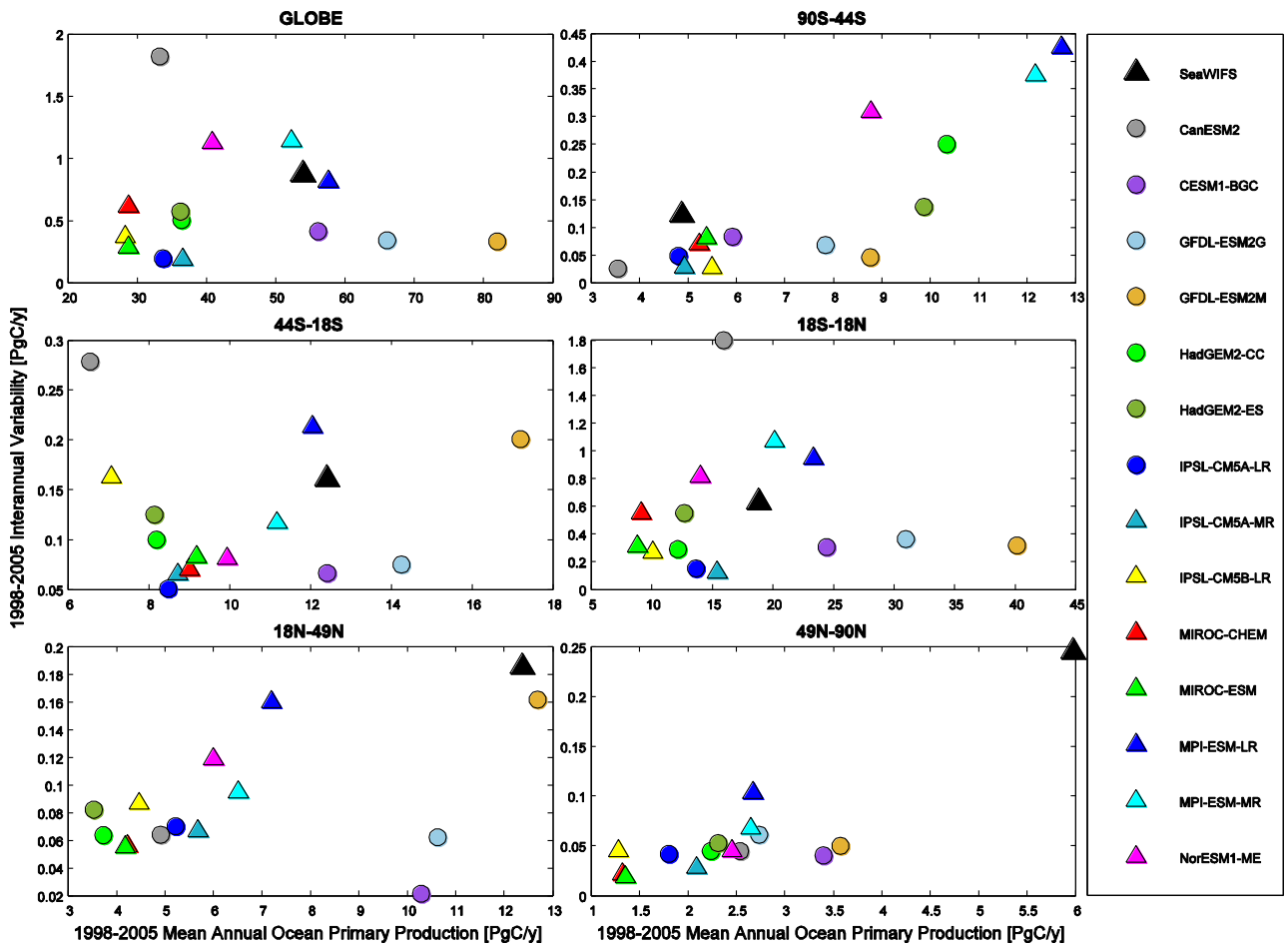


Figure 16. Ocean primary production integrated over the ocean sub-domains as simulated by CMIP5 models and observed (SeaWIFS) in the period 1998-2005.

2071
2072
2073
2074
2075
2076
2077

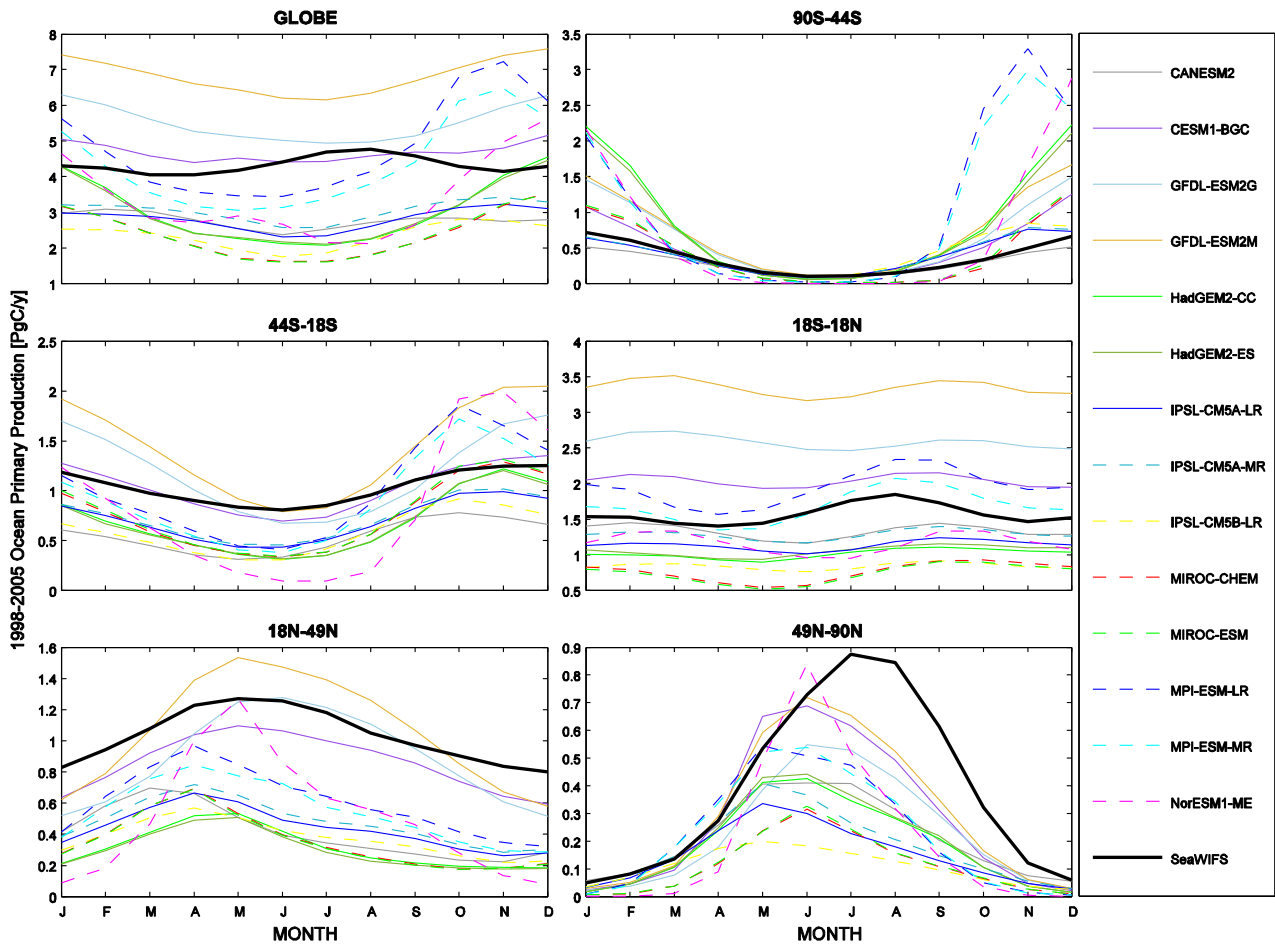
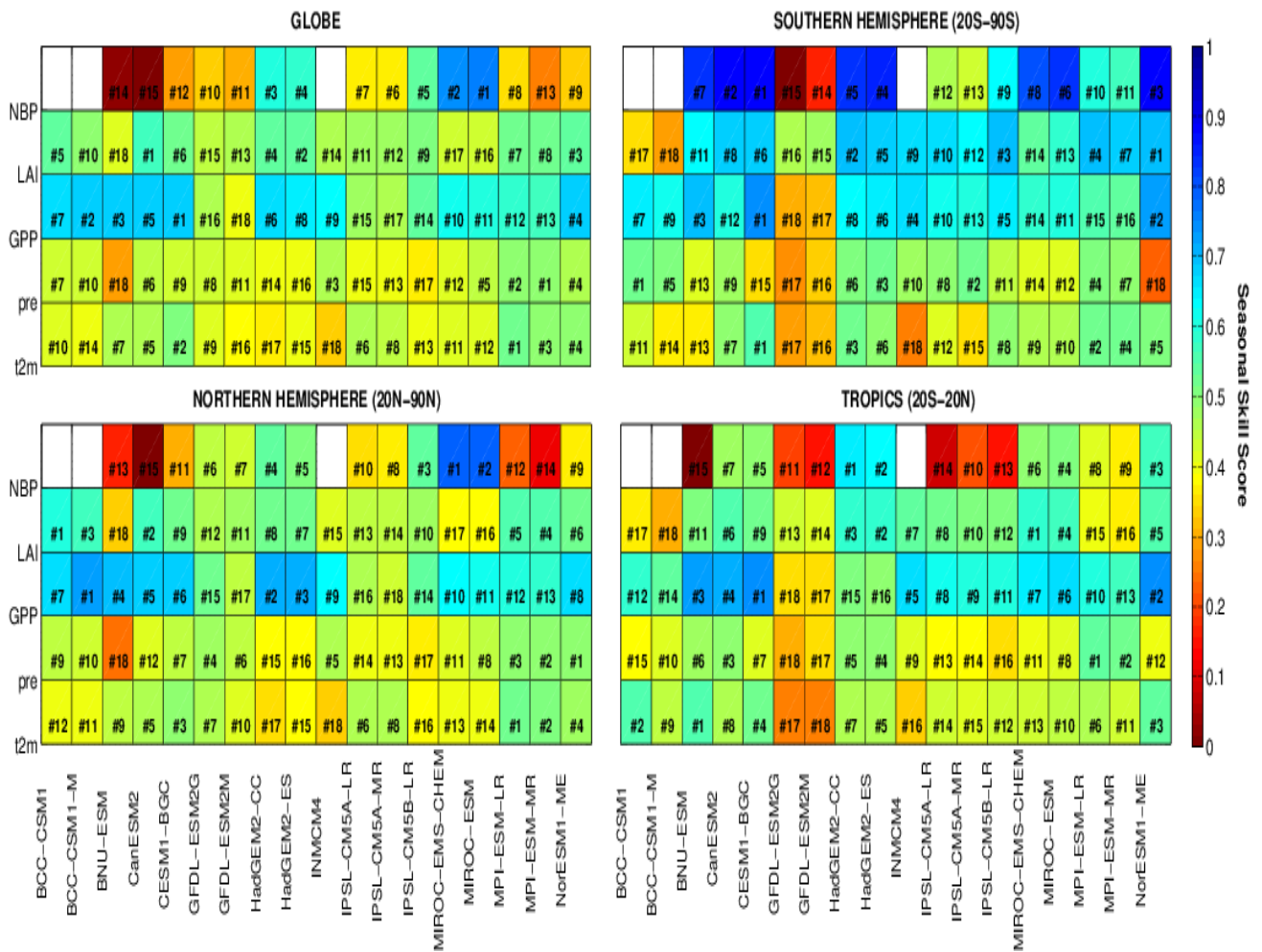
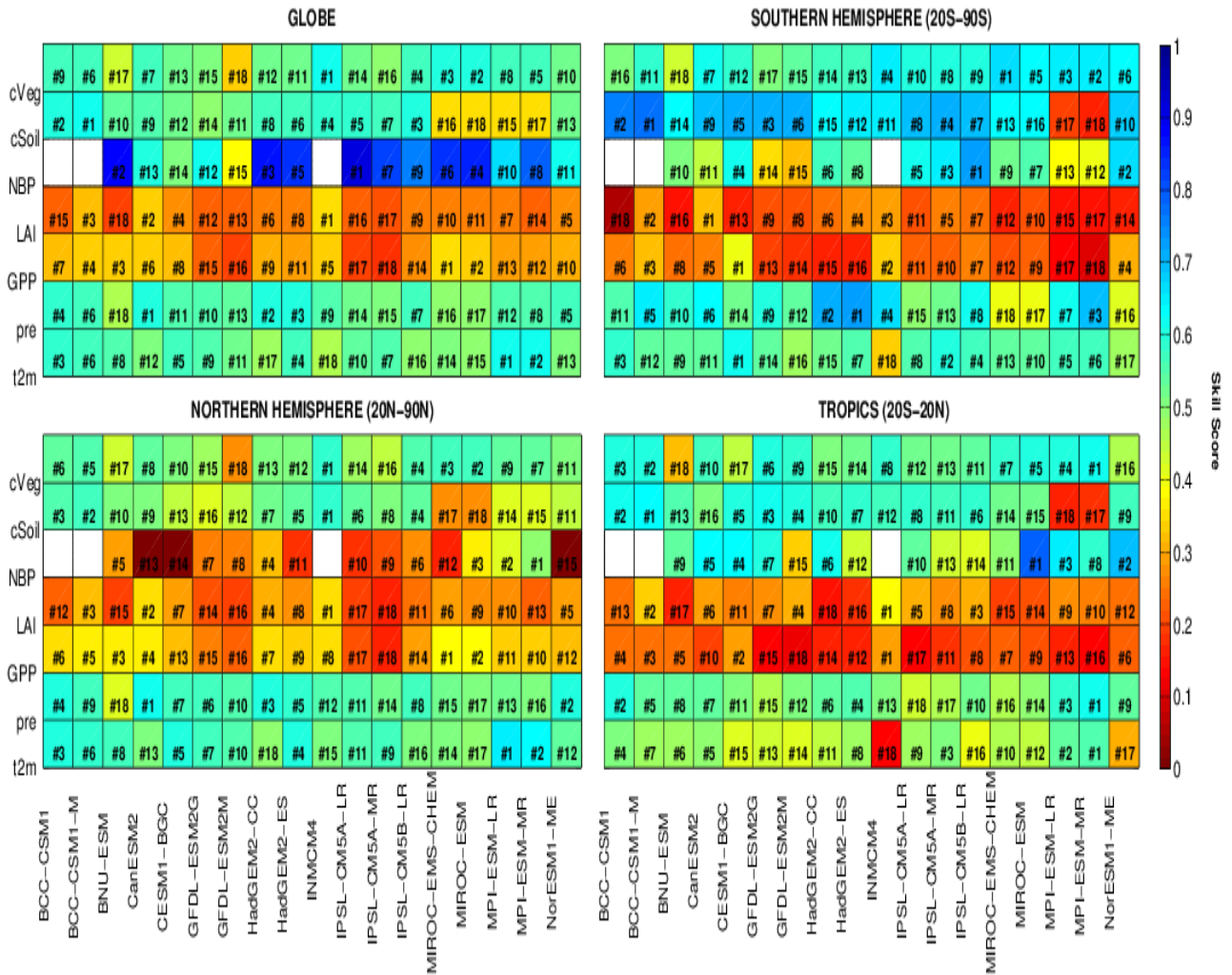


Figure 17. Comparison of ocean primary production (PgC/y) mean annual cycle as simulated by CMIP5 models and SeaWiFS observations in the period 1998-2005.

2078
 2079
 2080
 2081
 2082
 2083
 2084



2085
2086
2087 **Figure 18.** Seasonal skill score matrix as computed according to Equation 3 for the
2088 whole Globe, Southern Hemisphere (20°S-90°S), Northern Hemisphere (20°N-90°N), and Tropic
2089 (20°S-20°N). A score of 0 indicates poor performance of models reproducing the phase and
2090 amplitude of the reference mean annual cycle, while a perfect score is equal to 1.
2091



2092
2093
2094
2095
2096
2097
2098
2099
2100
2101
2102

Figure 19. PDF-based skill scores for temperature, precipitation, LAI, and NBP for the whole Globe, Southern Hemisphere (20°S-90°S), Northern Hemisphere (20°N-90°N), and Tropic (20°S-20°N). A perfect score is 1.

Note that since the reference data for the soil and vegetation carbon pools are a single annual data, we were unable to build the PDF, therefore the skill scores for these variables are based on the normalized mean bias between the model and the reference data (see equation 6).

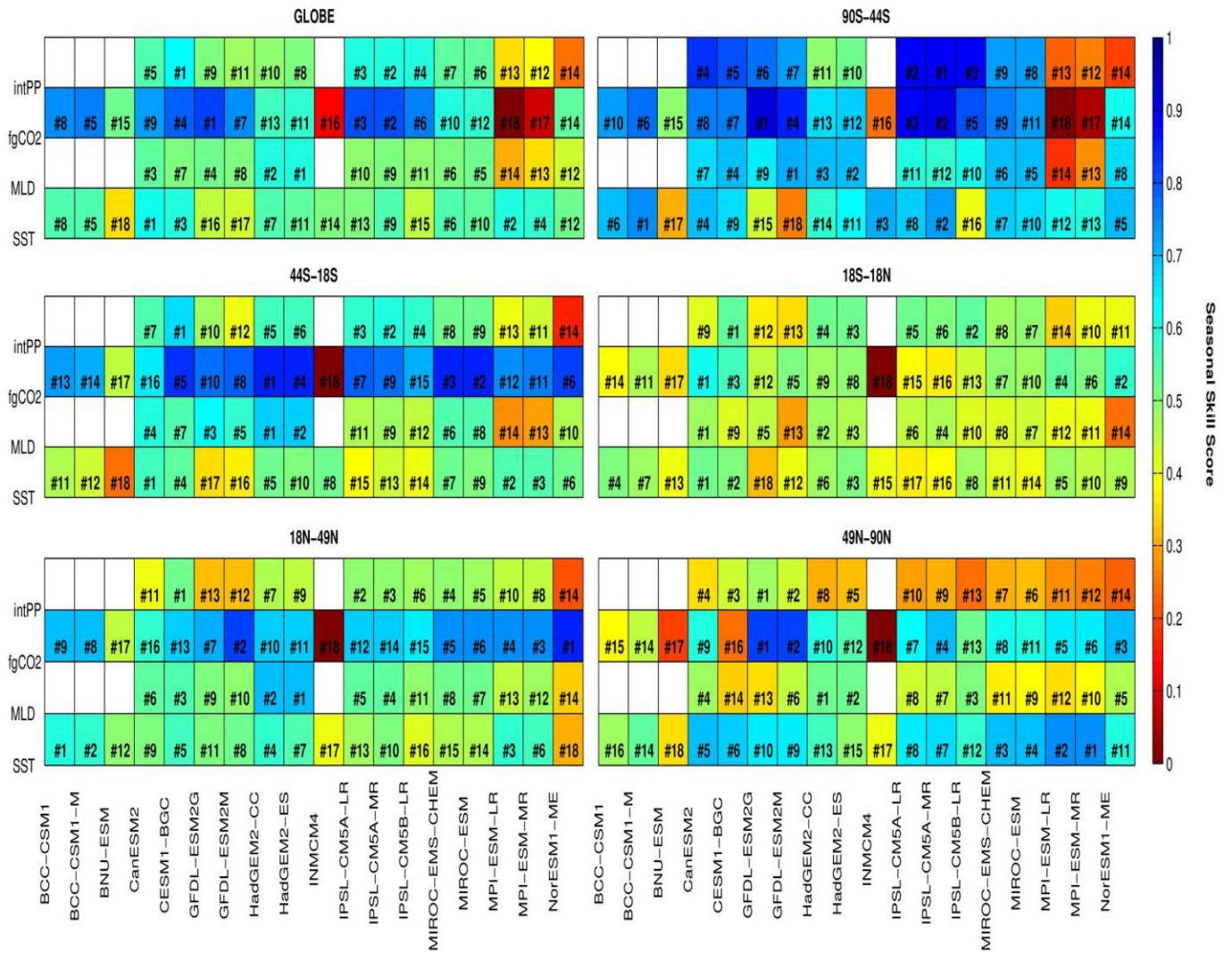


Figure 20. As Figure 18 but for the ocean variables.

2103
2104
2105

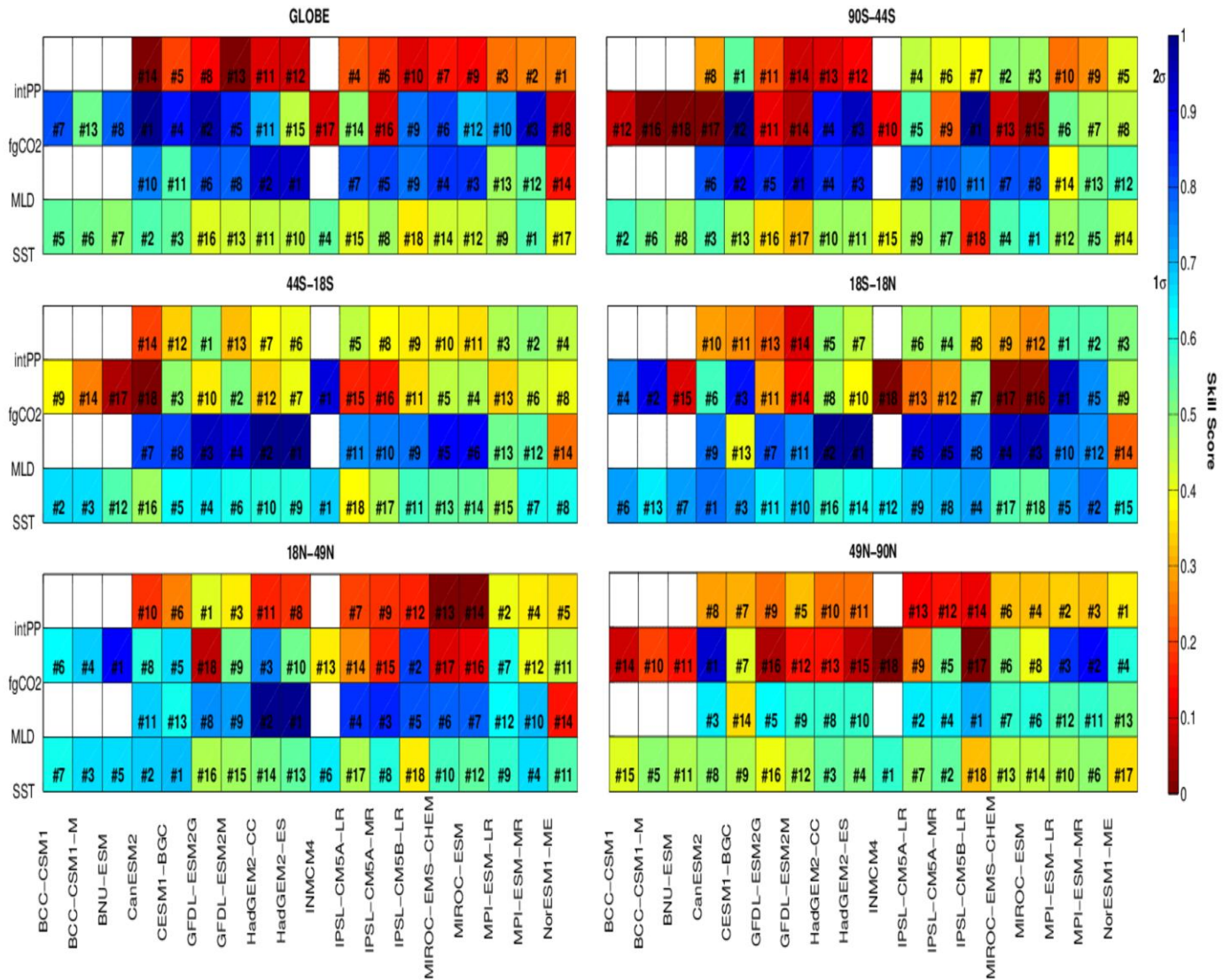


Figure 21. As Figure 19 but for the ocean variables. Note that since the MLD dataset is a climatology we were unable to compute the PDF, consequently the skill scores have been computed according to equation 6.

2106
2107
2108
2109
2110
2111